



HAL
open science

**Search for standard model production of four top quarks
with same-sign di-lepton and multi-lepton final states in
proton-proton collisions at $\sqrt{s} = 13$ TeV recorded
with the ATLAS detector**

Shuyang Hu

► **To cite this version:**

Shuyang Hu. Search for standard model production of four top quarks with same-sign di-lepton and multi-lepton final states in proton-proton collisions at $\sqrt{s} = 13$ TeV recorded with the ATLAS detector. High Energy Physics - Experiment [hep-ex]. Université Paris-Saclay; Shanghai Jiao Tong University, 2020. English. NNT : 2020UPASP098 . tel-03335413

HAL Id: tel-03335413

<https://theses.hal.science/tel-03335413>

Submitted on 6 Sep 2021

HAL is a multi-disciplinary open access archive for the deposit and dissemination of scientific research documents, whether they are published or not. The documents may come from teaching and research institutions in France or abroad, or from public or private research centers.

L'archive ouverte pluridisciplinaire **HAL**, est destinée au dépôt et à la diffusion de documents scientifiques de niveau recherche, publiés ou non, émanant des établissements d'enseignement et de recherche français ou étrangers, des laboratoires publics ou privés.

Search for standard model production of four top quarks with same-sign di-lepton and multi-lepton final states in proton-proton collisions at $\sqrt{s} = 13$ TeV recorded with the ATLAS detector

Recherche de la production de 4 quark tops dans le modèle standard avec des états finaux de même signe di-lepton et multi-lepton à 13 TeV avec le détecteur ATLAS au LHC

**Thèse de doctorat de l'université Paris-Saclay et de
Shanghai Jiao Tong University**

School of Physics and Astronomy, Shanghai Jiao Tong University
Shanghai Key Laboratory for Particle Physics and Cosmology

École doctorale n°576 Particules, Hadrons, Énergie et Noyau : Instrumentation,
Image, Cosmos et Simulation (PHENIICS)
Unité de recherche: Université Paris-Saclay, CEA, Département de Physique des
Particules, 91191, Gif-sur-Yvette, France
Spécialité de doctorat : Physique des particules
Réfèrent : Faculté des sciences d'Orsay

**Thèse présentée et soutenue à Shanghai, le 30/10/2020, par
Shuyang HU**

Composition du Jury

Gautier HAMEL DE MONCHENAU Cadre scientifique des EPIC, CEA-Saclay	Président
Daniel BLOCH Directeur de recherche, IPHC (Strasbourg)	Rapporteur & Examineur
Yaquan FANG Professeur, IHEP CAS (Beijing, Chine)	Rapporteur & Examineur
Haijun YANG Professeur, Shanghai Jiao Tong University	Examineur

Direction de la thèse

Frédéric DELIOT Cadre scientifique des EPIC, Université Paris-Saclay	Directeur de thèse
Liang LI Professeur, Shanghai Jiao Tong University	Directeur de thèse

上海交通大学

SHANGHAI JIAO TONG UNIVERSITY

博士学位论文

THESIS OF DOCTORAL DEGREE



论文题目：Search for standard model production of four top quarks with same-sign di-lepton and multi-lepton final states in proton-proton collisions at $\sqrt{s} = 13$ TeV recorded with the ATLAS detector

学生姓名： 胡舒旻

学生学号： 0130729009

专 业： 粒子物理学

指导教师： 李亮

学院(系)： 物理与天文系

PHD THESIS

Search for standard model production of four top quarks with same-sign di-lepton and multi-lepton final states in proton-proton collisions at $\sqrt{s} = 13$ TeV recorded with the ATLAS detector

Shanghai Jiao Tong University

Université Paris-Saclay

Shuyang Hu

Jury composition:

President: Gautier Hamel de Monchenault, CEA-Saclay, Senior physicist

Referee: Daniel Bloch, Institut Pluridisciplinaire Hubert Curien Strasbourg, Research Director

Referee: Yaquan Fang, The Institute of High Energy Physics of the Chinese Academy of Sciences, Researcher

Jury member: Haijun Yang, Shanghai Jiao Tong University, Professor

Jury member: Jun Gao, Shanghai Jiao Tong University, Researcher

Thesis Director: Frederic Deliot, CEA-Saclay, Senior physicist

Thesis Director: Liang Li, Shanghai Jiao Tong University, Professor

A DISSERTATION IN

Physics and Astronomy

In partial fulfillment of the requirements for the degree of

Doctor of physics

2020

摘要

使用 ATLAS 探测器在质心系能量为 13TeV 的质子质子对撞中寻找同电荷双轻子及多轻子末态下的标准模型四顶夸克产生过程

本论文给出了在 ATLAS 实验上对同电荷双轻子末态以及多轻子末态下标准模型四顶夸克产生过程进行寻找的最新实验结果。论文分析了 ATLAS 探测器于 2015-2018 年采集的整个 Run2 数据，质心系能量为 13TeV，积分亮度为 139 fb^{-1} 。四顶夸克多轻子衰变末态的信号特征为：含有两个（同电荷）轻子或者更多个轻子，有较多的夸克喷注（jets）和底夸克喷注（b-tagged jets）。我们首先对四顶夸克多轻子末态信号过程以及具有类似末态的背景过程进行了初步的区分和筛选。然后，我们采用了多变量分析（Multi-Variate Analysis - MVA）中的提升决策树（Boosting Decision Tree - BDT）方法进一步提升信号事例与背景事例的区分度。最后，我们通过信号区域和控制区域对信号判断函数的分布进行最大似然函数拟合得到了四顶夸克的反应截面以及相对标准模型预言值的信号产生强度。实验测得的四顶夸克的产生截面值为： $\delta_{\text{tttt}}=24+5-5(\text{stat})+5-4(\text{syst})\text{fb}=24+7-6 \text{ fb}$ ，与标准模型的预言值基本吻合（有 2 倍的标准方差）。信号强度为： $\mu=2.0+0.4-0.4(\text{stat})+0.7-0.4(\text{syst})=2.0+0.8-0.6$ 。该信号的观测（预期）统计显著性为 4.3（2.4）个标准偏差。这是标准模型四顶夸克产生过程的首个实验证据。

关键词：四顶夸克，标准模型，稀有过程，ATLAS

ABSTRACT

Search for standard model production of four top quarks with same-sign di-lepton and multi-lepton final states in proton-proton collisions at $\sqrt{s} = 13$ TeV recorded with the ATLAS detector

This thesis presents the latest results of the Standard Model four-top-quark search in the same sign di-lepton and multi-lepton channel. The analysis uses the full Run2 proton-proton collision dataset at $\sqrt{s}=13$ TeV collected with the ATLAS detector, which corresponds to an integrated luminosity of 139 fb^{-1} . Events with two same sign leptons or three or more leptons, plus multiple jets and b-tagged jets in the final states are considered in the analysis. Further event and kinematic selections are performed in separate signal and background control regions with proper background modelling. Boosting Decision Tree (BDT) based Multi-Variate Analysis (MVA) method is then used to enhance signal and background separation. Finally, a simultaneous likelihood fit is performed on the BDT discriminant across all the signal and background control regions to measure the four-top-quark production cross section and the signal strength (defined as the ratio of the measured cross section over the SM prediction). The measured four-top-quark production cross section is $\delta_{\text{tttt}}=24+5-5(\text{stat})+5-4(\text{syst})\text{fb}=24+7-6 \text{ fb}$, which is in consistent with the standard model prediction within 2 standard deviations. The corresponding signal strength is $\mu=2.0+0.4-0.4(\text{stat})+0.7-0.4(\text{syst})=2.0+0.8-0.6$. The observed (expected) significance of the four-top-quark signal is 4.3 (2.4) σ , which provides the first evidence for the SM four-top-quark production.

Key Words: Four Top Quarks, Standard Model, Rare Process, ATLAS

RÉSUMÉ

Recherche de la production standard de quatre quarks top dans l'état final avec deux leptons de même signe ou plusieurs leptons en collisions proton-proton à $\sqrt{s} = 13$ TeV avec le détecteur ATLAS

Cette thèse présente les résultats sur la recherche de la production de quatre quarks top dans le canal deux leptons de même signe ou multilepton. L'analyse utilise l'ensemble des collisions proton-proton du Run 2 du LHC à $\sqrt{s}=13$ TeV collecté avec le détecteur ATLAS, ce qui correspond à une luminosité de 139 fb^{-1} . Les événements avec deux leptons de même signe ou au moins trois leptons avec de nombreux jets en particulier provenant de quarks b sont considérés. Les événements sont sélectionnés en région de signal et régions de contrôle avec une modélisation du bruit de fond appropriée. Un arbre de décision boosté (BDT), qui est une méthode multivariée, est alors utilisé pour augmenter la séparation entre le signal et le bruit de fond. Enfin un ajustement par maximum de vraisemblance est effectué sur la sortie du BDT simultanément sur les régions de signal et de contrôle pour mesurer la section efficace de production de quatre quarks top et la force du signal (définie comme le rapport entre la section efficace mesurée et la prédiction du modèle standard). La section efficace mesurée est : $\sigma_{\text{tttt}} = 24 + 5 - 5(\text{stat}) + 5 - 4(\text{syst}) \text{ fb} = 24 + 7 - 6 \text{ fb}$, ce qui est compatible avec la prédiction du modèle standard à 1.7 déviations standard. La force du signal correspondante est : $\mu = 2.0 + 0.4 - 0.4(\text{stat}) + 0.7 - 0.4(\text{syst}) = 2.0 + 0.8 - 0.6$. La signification statistique observée (attendue) du signal quatre quarks top est 4.3 (2.4) σ , ce qui représente la première mise en évidence de ce processus.

Mots clés: quark top, modèle standard, processus rare, ATLAS

Contents

1. Overview	12
2. Introduction	14
2.1 The Standard Model	14
2.1.1 Elementary particles	14
2.1.2 Quantum Electrodynamics (QED)	15
2.1.3 Quantum Chromodynamics (QCD)	16
2.1.4 ElectroWeak Unification	17
2.1.5 Spontaneous Symmetry Breaking (SSB)	19
2.2 Top quark physics	21
2.3 Higgs boson physics	22
2.3.1 Higgs production mechanisms	22
2.3.2 Higgs Decays	24
2.3.3 Discovery of the Higgs boson	24
2.3.4 Properties of the Higgs boson	25
2.4 Top Yukawa coupling and $t\bar{t}H$ production	27
2.5 Four-top-quark production	28
3. LHC and ATLAS	33
3.1 LHC	33
3.2 The ATLAS detector	34
3.2.1 Inner detector	36
3.2.2 Calorimeter	36
3.2.2.1 The EM calorimeter	37
3.2.2.2 The hadronic calorimeter	37
3.2.3 The Muon spectrometer	38
3.2.4 The Trigger system	38
4. Object reconstruction	41
4.1 Primary Vertex	41
4.2 Electrons	41
4.2.1 Electron reconstruction	42
4.2.2 Electron identification	42
4.2.3 Electron isolation	43
4.3 Muons	43
4.3.1 Muon reconstruction	43
4.3.2 Muon identification	43
4.3.3 Muon isolation	44
4.4 Jets	46
4.5 b-tagged jets	47
4.6 Missing transverse momentum	48

5. Data sample and Monte Carlo simulation	50
5.1 Data	50
5.2 Simulated samples	50
6. Event Selection	55
6.1 Trigger list	55
6.2 Object overlap removal and definition	56
6.3 Event pre-selection and categorization	57
7. Background Modelling	59
7.1 Estimation of the charge mis-identification background	59
7.2 Estimation of the non-prompt and fake background	67
7.2.1 The template fit method	67
7.2.2 The data-driven matrix method	70
7.3 Pre-fit and post-fit Data/MC comparison	73
8. Multivariate Analysis	79
9. Systematic Uncertainties	87
9.1 Experimental uncertainties	87
9.2 Background modelling uncertainties	88
9.2.1 $t\bar{t}$ +jets related backgrounds	88
9.2.2 non- $t\bar{t}$ +jets backgrounds	89
9.3 Signal modelling uncertainties	89
10. Statistical treatment and results	92
11. Conclusion and outlook	113
Appendix A. Systematic uncertainty of the charge mis-identification rates	114
Appendix B. Extended Abstract in French / Résumé en Français	121
Acknowledgement	127
List of Publication	128

List of figures

2.1	Potential V of a scalar field ϕ with $\mu^2 < 0$ and $\lambda > 0$	20
2.2	Summary of the ATLAS measurements of the top quark mass	21
2.3	Feynman diagram of the top quark decay	21
2.4	Summary of ATLAS measurements of the top-pair production cross-section as a function of the centre-of-mass energy compared to the NNLO QCD calculation complemented with NNLL resummation	22
2.5	Feynman diagrams for the four dominant SM Higgs boson production mechanisms at the LHC	23
2.6	(a) Cross-sections for different SM Higgs production mechanisms at the LHC, as a function of the Higgs mass (b) Total cross-section for SM Higgs production at the LHC, as a function of the Higgs mass (with $M_H = 125$ GeV measured in experiment)	23
2.7	Branching ratios of the SM Higgs boson as a function of its mass	24
2.8	The observed local p value as a function of the SM Higgs boson mass from ATLAS(left) and CMS(right) respectively	25
2.9	Summary of the measurements of the SM Higgs boson mass	25
2.10	Cross sections times branching fraction for different Higgs production mechanisms in each relevant decay mode, normalized to their SM predictions	26
2.11	Negative log-likelihood contours at 68% and 95% CL in the κ_V^f, κ_F^f plane for the individual decay modes and their combination	27
2.12	Examples of tree-level Feynman diagrams for the production of the Higgs boson in association with a pair of top quarks	28
2.13	Example of Feynman diagram for the Standard Model four-top-quark production	29
2.14	Feynman diagram for vector-like $T_{5/3}$ single (left) and pair production (right)	29
2.15	Example of Feynman diagram of four-top-quark production in Effective Field Theory with contact interaction	29
2.16	Example of Feynman diagram of four-top-quark production in 2HDM	30
2.17	Example of Feynman diagram of four-top-quark production in 2UED/RPP model	30
3.1	The accelerator complex at CERN	33
3.2	Diagram of the ATLAS detector system	34
3.3	Illustration of the ATLAS coordinate system	35
3.4	Overview picture of the ATLAS inner detector (left) and illustration of the inner detector in the barrel region (right)	36
3.5	Illustration of the ATLAS calorimeters	36
3.6	Illustration of the ATLAS Muon Spectrometer	38
3.7	Illustration of the ATLAS Trigger and Data acquisition system	39
4.1	Overview of different particle signatures in the ATLAS detector	41
4.2	Distribution of relative muon isolation variables: track based $p_T^{\text{varcone30}} / p_T$ (left) and calorimeter based $E_T^{\text{topocone20}} / p_T$ (right)	45
4.3	Muon isolation efficiencies as a function of muon p_T for different working points	46

4.4	Schematic plot of ATLAS jet reconstruction procedure	47
6.1	Branching ratios of the $t\bar{t}\bar{t}$ decay modes	55
7.1	Charge mis-identification due to a straight track	60
7.2	Charge mis-identification due to bremsstrahlung and photon conversion	60
7.3	Z mass fit on di-electron invariant mass distributions for same sign events (left) and opposite sign events (right) in a data $Z \rightarrow ee$ enriched region	61
7.4	Data/MC comparison of the di-electron invariant mass distribution for the opposite sign (left) and same sign (right) electron pairs in the Z peak region using 2016 data	61
7.5	Kinematic distributions of opposite sign events (top) and same sign events (bottom) in the Z peak region using 2016 data	62
7.6	Extracted charge mis-identification rates using the likelihood method in data (left) and Z+jets MC (right) samples as a function of electron's p_T and $ \eta $	63
7.7	Closure test of kinematic distributions in the Z peak region in 2016 data sample with charge mis-identification weights applied on the opposite sign events	64
7.8	Closure test of kinematic distributions in the Z peak region in Z+jets sample with charge mis-identification weights applied on the opposite sign events	65
7.9	Extracted charge mis-identification rates using a likelihood method in data samples as a function of electron's p_T and $ \eta $ in the $t\bar{t}W$ control region	66
7.10	Extracted charge mis-identification rates using a likelihood method in data samples as a function of electron's p_T , $ \eta $ and $M_{ee}@PV$ in the conversion control region	67
7.11	Pre-fit distributions in the signal region	69
7.12	Measured prompt and fake efficiencies as a function of lepton's p_T in 2015-2016 data	71
7.13	Measured prompt and fake efficiencies as a function of lepton's p_T in 2017 data	71
7.14	Measured prompt and fake efficiencies as a function of lepton's p_T in 2018 data	72
7.15	Distributions of different kinematic variables in the control region using data-driven Matrix Method fake estimation	73
7.16	Pre-fit (left) and post-fit (right) kinematic distributions in the region with $BDT < 0$	74
7.17	Pre-fit and post-fit BDT distribution in the $t\bar{t}Z$ control region	75
7.18	Pre-fit and post-fit event yields difference between all positively charged leptons and all negatively charge leptons as a function of the multivariate discriminant	75
7.19	Post-fit event yields difference between all positively charged leptons and all negatively charge leptons as a function of the number of jets	76
8.1	Illustration of the train-test-validation procedure for the BDT analysis	79
8.2	Example of a typical ROC curve for the trained BDT model	80
8.3	Post-fit data/MC comparison of BDT input variables in the region with $BDT < 0$	82
8.4	Post-fit data/MC comparison of BDT input variables in the region with $BDT < 0$	83
8.5	Shape comparison between signal and all background for BDT input variables	84
8.6	Pre-fit (left) and post-fit (right) BDT distributions in the signal region	85
10.1	Pre-fit distributions in the $BDT > 0$ region	94
10.2	Pre-fit distributions in the $BDT > 0$ region	95
10.3	Pre-fit distributions in the $BDT > 0$ region	96
10.4	Fitted normalization factors and signal strength for the plain Asimov fit	98
10.5	Ranking plot of the nuisance parameters for the plain Asimov fit	99
10.6	Fitted normalization factors and signal strength for the realistic Asimov fit	100

10.7	Constraints and pulls of all the nuisance parameters for the realistic Asimov fit	101
10.8	Ranking plot of the nuisance parameters for the Realistic Asimov fit	102
10.9	Post-fit distributions of the fitted variables in each of the regions	104
10.10	Post-fit distributions in the BDT>0 region	105
10.11	Post-fit distributions in the BDT>0 region	106
10.12	Post-fit distributions in the BDT>0 region	107
10.13	Fitted normalization factors and signal strength for the full fit on data	108
10.14	Constraints and pulls of all the nuisance parameters for the full fit on data	109
10.15	Ranking plots of the nuisance parameters for the full fit on data	110
A.1	Total systematic uncertainty of the electron charge mis-identification rates as a function of electron's p_T and $ \eta $	114
A.2	Statistical uncertainty of the electron charge mis-identification rates as a function of electron's p_T and $ \eta $	115
A.3	Difference between the electron charge mis-identification rates from the likelihood fit method and the truth method as a function of electron's p_T and $ \eta $	115
A.4	Z peak range variation uncertainties of the electron charge mis-identification rates as a function of electron's p_T and $ \eta $	116
A.5	Total systematic uncertainty of the electron charge mis-identification rates as a function of electron's p_T and $ \eta $ in $t\bar{t}W$ control region	116
A.6	Statistical uncertainty of the electron charge mis-identification rates as a function of electron's p_T and $ \eta $ in $t\bar{t}W$ control region	117
A.7	Difference between the electron charge mis-identification rates from the likelihood fit method and the truth method as a function of electron's p_T and $ \eta $ in $t\bar{t}W$ control region	117
A.8	Z peak range variation uncertainties of the electron charge mis-identification rates as a function of electron's p_T and $ \eta $ in $t\bar{t}W$ control region	118
A.9	Total systematic uncertainty of the electron charge mis-identification rates as a function of electron's p_T and $ \eta $ in conversion control region	118
A.10	Statistical uncertainty of the electron charge mis-identification rates as a function of electron's p_T and $ \eta $ in conversion control region	119
A.11	Difference between the electron charge mis-identification rates from the likelihood fit method and the truth method as a function of electron's p_T and $ \eta $ in conversion control region	119
A.12	Z peak range variation uncertainties of the electron charge mis-identification rates as a function of electron's p_T and $ \eta $ in conversion control region	120
B.1	Exemple de diagramme de Feynman pour la production de 4 tops dans le MS	121
B.2	Distribution de l'isolation relative basée sur les traces $p_T^{\text{varcone30}} / p_T$ (gauche) et sur le calorimètre $E_T^{\text{topocone20}} / p_T$ (droit)	122
B.3	Taux de mauvaise identification de la charge des électrons en utilisant une méthode de vraisemblance dans les données (gauche) et pour la simulation Z+jets (droite) en fonction du p_T et $ \eta $ de l'électron	124
B.4	Distribution pre-fit (gauche) et post-fit (droite) de la sortie du BDT dans la région de signal	125
B.5	Distributions post-fit pour la région BDT>0	125

List of tables

2.1	Elementary particles in the Standard Model	15
2.2	Branching ratios and total width of the SM Higgs boson at $m_H = 125$ GeV	24
3.1	Designed performance goals for different components of the ATLAS detector	35
4.1	Definitions of all the muon isolation working points	45
5.1	Detailed settings of different Monte Carlo processes	50
6.1	List of single lepton triggers used in the analysis for each data period	56
6.2	List of dilepton triggers used in the analysis for each data period	56
6.3	Summary of object identification and definitions	57
7.1	Summary of the different control regions and the signal region definitions used in the analysis	69
7.2	Fitted values of the normalization factors from the simultaneous fit in all CRs	69
7.3	Summary of the selections for the single lepton data control samples used to measure lepton real efficiency and fake rate	70
7.4	Comparison between the signal and background yields with template fit fakes and matrix method fakes (post-fit)	77
8.1	Optimized BDT hyper-parameters	80
8.2	Information of the final BDT input variables list	81
9.1	Summary of the impact of the leading systematic uncertainties on the post-fit signal strength	90
10.1	Expected background and signal yields in the allBDT signal region and the BDT>0 region after the plain Asimov fit	97
10.2	Expected $t\bar{t}t$ significance for different intermediate fitting steps	103
10.3	Expected background and signal yields in the signal region after the full fit on data	103
B.1	Valeurs ajustées pour la normalisation des composantes de faux leptons et pour le bruit de fond $t\bar{t}W$	124

Chapter 1

Overview

During the past few decades, elementary particle physics has undergone great development both theoretically and experimentally. The Standard Model (SM) is a successful theoretical model, which provides a unified description of elementary particles and their interactions. The Large Hadron Collider (LHC) established at CERN, is the world's leading collider at the energy frontier of experimental particle physics. The Higgs field is responsible for the mass generation of elementary particles, and the Higgs boson is regarded as the last piece of the Standard Model for decades before its discovery. After the discovery of the Higgs boson by ATLAS [1] and CMS [2] experiments in 2012, the Standard Model is finally completed.

Although SM is successful, some rare but important processes have not been observed experimentally yet. Furthermore, there are still several issues which cannot be explained, such as the hierarchy problem, neutrino mass, dark matter origin etc. Therefore, searches for Beyond Standard Model (BSM) scenarios are important. For these reasons, four-top-quark production [3-7] is of particular interest. It is a rare process predicted by the SM but not observed yet. It is also sensitive to various BSM models owing to its large energy scale.

This thesis presents the latest search results for the SM four-top-quark production in the same sign di-lepton and multi-lepton (SSML) channel, using a dataset corresponding to an integrated luminosity of 139 fb^{-1} collected with the ATLAS detector. Events with two same sign leptons or three or more leptons, plus multiple jets and b-tagged jets are used. Further event and kinematic selections are performed in separate signal and background control regions with proper background modelling. A multi-variate analysis method with Boosting Decision Tree (BDT) discriminant is used to optimize on signal and background separation. Finally, a combined fit using the BDT output is performed across all the signal and background control regions to measure the four-top-quark production cross section and the signal strength. The signal strength is defined as the ratio of the measured cross section over the SM prediction.

The thesis is organized as follows: Chapter 2 presents the theory overview and Chapter 3 is an introduction of the LHC project and the ATLAS detector. Object reconstruction criteria is introduced in Chapter 4. The main analysis description starts from Chapter 5, which summarizes the data and Monte Carlo simulation samples used in the analysis. Chapter 6 introduces the event selections. Background modelling is discussed in Chapter 7, which provides the validation of the background estimation. Finally, Chapter 8 summarizes the systematic uncertainties considered in this analysis. Chapter 9 describes the multivariate analysis, which is performed to enhance the signal and background separation and measurement sensitivity. Chapter 10 provides the statistical method and the final results. Finally, Chapter 11 presents the conclusion and the outlook.

Reference:

- [1] ATLAS Collaboration, Observation of a new particle in the search for the Standard Model Higgs boson with the ATLAS detector at the LHC, Physics Letters B 716 (2012) 1-29, arXiv:1207.7214 [hep-ex].
- [2] CMS Collaboration, Observation of a new boson at a mass of 125 GeV with the CMS experiment at the LHC, Physics Letters B 716 (2012) 30, arXiv:1207.7235 [hep-ex].
- [3] ATLAS Collaboration, Search for new phenomena in events with same-charge leptons and b-jets in pp collisions at $\sqrt{s}=13$ TeV with the ATLAS detector, JHEP 12 (2018) 039, arXiv:1807.11883 [hep-ex].
- [4] ATLAS Collaboration, Search for four-top-quark production in the single-lepton and opposite-sign dilepton final states in pp collisions at $\sqrt{s}=13$ TeV with the ATLAS detector, Phys. Rev. D 99 (2019) 052009, arXiv: 1811.02305 [hep-ex].
- [5] CMS Collaboration, Search for the production of four top quarks in the single-lepton and opposite-sign dilepton final states in proton-proton collisions at $\sqrt{s}=13$ TeV, JHEP 11 (2019) 082, arXiv: 1906.02805 [hep-ex].
- [6] CMS Collaboration, Search for the production of four top quarks in final states with same-sign or multiple leptons in proton-proton collisions at $\sqrt{s}=13$ TeV, Eur. Phys. J. C 80 (2020) 75, arXiv: 1908.06463 [hep-ex].
- [7] ATLAS Collaboration, Evidence for $t\bar{t}\bar{t}$ production in the multilepton final state in proton-proton collisions at $\sqrt{s}=13$ TeV with the ATLAS detector, accepted by EPJC, arXiv: 2007.14858 [hep-ex].

Chapter 2

Introduction

The particle physics theory called the Standard Model (SM) is very successful. All of the SM predictions of new particles have been discovered and their properties have been precisely measured by experiments. The level of agreement between the experiment measurements and theory predictions is remarkably good.

2.1 The Standard Model

The Standard Model provides a unitary description of elementary particles and their interactions [1].

2.1.1 Elementary particles

There are in general two types of particles, namely fermions and bosons. Fermions are particles with spin - 1/2, which make up the concrete matter in our daily life. Fermions consist of 3 generations of leptons, quarks and neutrinos, together with their anti-particle partners. Anti-particles are those particles which have an opposite electric charge to the particles, with the other properties remaining the same. The 1st generation particles are stable, while the 2nd and 3rd generation particles will decay to the 1st generation particles in a very short time scale. Bosons are particles with integer spin. They play the role of force carriers and the propagation mediators in particles' interactions. Bosons consist of photon, which is the mediator of electromagnetic interactions, weak bosons (Z, W⁺, W⁻), which are the mediators of weak interactions, gluons, which are the mediators of strong interactions, and the newly discovered Higgs boson, of which the associated Higgs field accounts for the mass generation of particles. The gravitational force is not included in the SM, as it is very small compared to the other forces. Elementary particles in the SM [2] are summarized in Table 2.1.

	Name	Spin	Charge	Mass
Quarks	u	1/2	+2/3	2.2 MeV
	d	1/2	-1/3	4.7 MeV
	c	1/2	+2/3	1.27 GeV
	s	1/2	-1/3	96 MeV
	t	1/2	+2/3	173 GeV
	b	1/2	-1/3	4.2 GeV
Leptons	e	1/2	-1	0.511 MeV
	ν_e	1/2	0	< 2 eV
	μ	1/2	-1	105 MeV
	ν_μ	1/2	0	< 0.19 MeV
	τ	1/2	-1	1.78 GeV
	ν_τ	1/2	0	< 18.2 MeV
Gauge Bosons	γ	1	0	0 GeV
	g	1	0	0 GeV
	W^\pm	1	± 1	80 GeV
	Z	1	0	91 GeV
	H	0	0	125 GeV

Table 2.1 Elementary particles in the Standard Model

2.1.2 Quantum Electrodynamics (QED)

The Standard Model is based on Quantum Field Theory (QFT). In QFT, the vacuum is composed of various fields in the ground state, and particles are excitations of these ground state fields.

Let's consider the Lagrangian of a particle field $\phi(x)$ [3], which is expressed as a function of the field and the first derivative with respect to space and time:

$$L(x) = L(\phi, \partial_\mu \phi), \quad 2.1$$

then the principle of least action can be written as:

$$\delta S = \delta \int d^4x L(\phi, \partial_\mu \phi) = 0, \quad 2.2$$

and the Euler-Lagrangian equation can be derived:

$$\partial_\mu \left(\frac{\partial L}{\partial(\partial_\mu \phi)} \right) - \frac{\partial L}{\partial \phi} = 0. \quad 2.3$$

Let's consider the Dirac Lagrangian for a free fermion of mass m:

$$L_{Dirac} = \bar{\psi}(x)(i\gamma^\mu \partial_\mu - m)\psi(x), \quad 2.4$$

where $\psi(x)$ represents the fermion field, and γ^μ are the Dirac gamma matrices. After applying

the Euler-Lagrange equation, we can get the equation of motion for a free fermion:

$$(i\gamma^\mu \partial_\mu - m)\psi(x) = 0. \quad 2.5$$

According to gauge theory, the underlying physics should remain unchanged under local gauge transformation of certain Lie groups. The free QED Lagrangian needs to remain invariant under the local gauge transformation of the U(1) group,

$$\psi(x) \rightarrow U\psi(x) = e^{i\theta(x)}\psi(x), \quad 2.6$$

while the initial form doesn't satisfy this requirement. To achieve this, the partial derivative ∂_μ is replaced by the covariant derivative D_μ , which is defined as:

$$D_\mu \equiv \partial_\mu + iqA_\mu(x). \quad 2.7$$

Here q is the electric charge, and A(x) transforms as:

$$A_\mu(x) \rightarrow A_\mu(x) - \frac{1}{q} \partial_\mu \theta(x). \quad 2.8$$

After replacing the partial derivative with the covariant derivative, the local gauge invariance of U(1) transformation is achieved, and the Lagrangian can be written as:

$$L = \bar{\psi}(x)(i\gamma^\mu D_\mu - m)\psi(x) = L_{Dirac} - q\bar{\psi}(x)\gamma^\mu A_\mu(x)\psi(x). \quad 2.9$$

Here the second term describes the interaction between the fermion and the vector field A(x). In order to comply with the formalism of Maxwell, a kinetic term is added to the Lagrangian,

$$L_{Kin} = -\frac{1}{4} F_{\mu\nu}(x)F^{\mu\nu}(x), \quad 2.10$$

where $F_{\mu\nu} = \partial_\mu A_\nu - \partial_\nu A_\mu$ is the electromagnetic strength tensor.

Finally, the QED Lagrangian can be written as:

$$L_{QED} = L_{Dirac} - q\bar{\psi}(x)\gamma^\mu A_\mu(x)\psi(x) - \frac{1}{4} F_{\mu\nu}(x)F^{\mu\nu}(x). \quad 2.11$$

This Lagrangian is invariant under U(1) transformation. However, a mass term such as $\frac{1}{2}m^2 A^\mu A_\mu$ is prohibited. So the photon is predicted to be massless.

2.1.3 Quantum Chromodynamics (QCD)

Quarks are triplets of colour under the SU(3) group. The quark field can be represented in the vector form:

$$q_f = \begin{pmatrix} q_f^R \\ q_f^G \\ q_f^B \end{pmatrix}, \quad \bar{q}_f = \left(\bar{q}_f^{\bar{R}}, \bar{q}_f^{\bar{G}}, \bar{q}_f^{\bar{B}} \right). \quad 2.12$$

Similar with QED, the Lagrangian for free quarks can be written as:

$$L = \sum_f \bar{q}_f (i\gamma^\mu \partial_\mu - m_f) q_f. \quad 2.13$$

Again, in order to satisfy local gauge invariance under the SU(3) transformation, the covariant derivative is introduced to replace the partial derivative in the Lagrangian:

$$D_\mu \equiv \partial_\mu + ig_s \frac{\lambda_a}{2} G_\mu^a(x), \quad 2.14$$

where g_s is the strong coupling constant, and $\frac{\lambda_a}{2}$ are the Gell-Mann matrices, which represent the

8 generators of the SU(3) group. $G_\mu^a(x)$ are the newly introduced gluon fields in order to define the covariant derivative.

Under SU(3), $G_\mu^a(x)$ transforms as:

$$G_\mu^a \rightarrow G_\mu^a - \frac{1}{g_s} \partial_\mu \theta_a - f_{abc} \theta_b G_\mu^c. \quad 2.15$$

Finally, adding the kinetic term of gluons, the final version of QCD Lagrangian is:

$$L_{QCD} = \sum_f \bar{q}_f (i\gamma^\mu \partial_\mu - m_f) q_f - g_s \sum_f (\bar{q}_f \gamma^\mu \frac{\lambda_a}{2} q_f) G_\mu^a - \frac{1}{4} G_{\mu\nu}^a G_a^{\mu\nu}, \quad 2.16$$

where $G_{\mu\nu}^a = \partial_\mu G_\nu^a - \partial_\nu G_\mu^a - g_s f_{abc} G_\mu^b G_\nu^c$ is the gluon tensor field, and f_{abc} provides the SU(3) structure constants. The second term in the Lagrangian represents the interaction between quarks and gluons, which is similar as in QED. However, in the third term, we have quadratic component which is the kinetic term of gluons, and we also have cubic and quartic component which represents self-interaction between gluons.

2.1.4 ElectroWeak Unification

Experiments have shown that weak interactions violate parity, which means only left-handed fermions and right-handed anti-fermions couple to the W^\pm bosons. This fact requires us to separate the two components when we express the fermion field involved in weak interactions. We will consider the left-handed fermions to be doublets, while the right-handed partners will be singlets. Then the fermion fields can be represented as:

$$L^i = \begin{pmatrix} \psi_L^i \\ \psi_R^i \end{pmatrix} \psi_R^i \psi_R^i. \quad 2.17$$

The simplest form to represent doublets is the SU(2) group, and since we want to include electromagnetic (EM) interactions as well, we also consider the U(1) group. Thus the electroweak (EW) interactions are described by the $SU(2)_L \otimes U(1)$ group. Similar to QED and QCD, the Lagrangian for free EW fermions can be written as:

$$L_{EW,free} = \sum_{q,l} \sum_{i=1}^3 (\bar{L}^i i\gamma^\mu \partial_\mu L^i + \bar{\psi}_R^i i\gamma^\mu \partial_\mu \psi_R^i + \bar{\psi}'_R^i i\gamma^\mu \partial_\mu \psi_R^i), \quad 2.18$$

where the summation is over 3 generations of quarks and leptons.

The covariant derivative is defined as:

$$D_\mu \equiv \partial_\mu + ig' \frac{Y}{2} B_\mu(x) + ig \frac{\sigma_a}{2} W_\mu^a(x), \quad 2.19$$

where B(x) is the gauge field corresponding to the U(1) group, and W(x) is the gauge field corresponding to the SU(2) group.

The left-handed doublet component transforms as:

$$\psi_1(x) \rightarrow e^{i\frac{\sigma_a}{2}\alpha_a + i\frac{Y}{2}\beta} \psi_1(x), \quad 2.20$$

while the right-handed singlet component transforms as:

$$\psi_2(x) \rightarrow e^{iY\beta} \psi_2(x). \quad 2.21$$

Finally, strength tensors are introduced to complete the EW Lagrangian:

$$L_{EW} = \sum_{j=1}^3 i\bar{\psi}_j(x) \gamma^\mu D_\mu \psi_j(x) - \frac{1}{4} B_{\mu\nu} B_{\mu\nu} - \frac{1}{4} W_{\mu\nu}^a W_a^{\mu\nu},$$

$$B_{\mu\nu} = \partial_\mu B_\nu - \partial_\nu B_\mu,$$

$$W_{\mu\nu}^a = \partial_\mu W_\nu^a - \partial_\nu W_\mu^a - g\epsilon_{abc} W_\mu^b W_\nu^c, \quad 2.22$$

where ϵ_{abc} is an anti-symmetric tensor which provides the structure constants of the SU(2) group.

After expanding the covariant derivative in the Lagrangian, we can get the interaction term between fermions and gauge bosons:

$$L_{int} = -g\bar{\psi}_1 \gamma_\mu \frac{\sigma_a}{2} W_\mu^a \psi_1 - g' B_\mu \sum_{j=1}^3 \frac{Y_j}{2} \bar{\psi}_j \gamma^\mu \psi_j. \quad 2.23$$

If we make a simple mathematical transformation of:

$$W_\mu = \frac{W_\mu^1 + iW_\mu^2}{\sqrt{2}},$$

$$W_\mu^+ = \frac{W_\mu^1 - iW_\mu^2}{\sqrt{2}}, \quad 2.24$$

then the W_μ, W_μ^+ can be identified as the W^\pm bosons, and we can separate the Lagrangian into the charge current and neutral current components. For the neutral current part, we have the following relationship:

$$\begin{pmatrix} W_\mu^3 \\ B_\mu \end{pmatrix} = \begin{pmatrix} \cos \theta_W & \sin \theta_W \\ -\sin \theta_W & \cos \theta_W \end{pmatrix} \begin{pmatrix} Z_\mu \\ A_\mu \end{pmatrix}, \quad 2.25$$

where Z_μ and A_μ are physical Z^0 boson and photon, and θ_W is the weak mixing angle. θ_W is directly related to the coupling constants:

$$\cos \theta_w = \frac{g}{\sqrt{g^2 + g'^2}}, \quad \sin \theta_w = \frac{g'}{\sqrt{g^2 + g'^2}}, \quad 2.26$$

where g is the SU(2) coupling constant and g' is the U(1) coupling constant.

2.1.5 Spontaneous Symmetry Breaking (SSB)

The gauge symmetry is important because it guarantees the theory to be renormalizable so that perturbation theory can be used to make predictions. However, from the previous section, we know that local gauge invariance forbids any mass terms in the Lagrangian, so all the gauge bosons as well as fermions are predicted to be massless. But this only holds true with photon and gluons. This problem can be dealt with by introducing the Higgs mechanism of Spontaneous Symmetry Breaking (SSB).

Let's consider a doublet of complex scalar fields

$$\phi(x) = \begin{pmatrix} \phi^+(x) \\ \phi^0(x) \end{pmatrix} = \begin{pmatrix} \frac{1}{\sqrt{2}}(\phi_1 + i\phi_2) \\ \frac{1}{\sqrt{2}}(\phi_3 + i\phi_4) \end{pmatrix}, \quad 2.27$$

and the corresponding Lagrangian written as:

$$L_{Higgs} = (D_\mu \phi)^\dagger D^\mu \phi - \mu^2 \phi^\dagger \phi - \lambda (\phi^\dagger \phi)^2, \quad 2.28$$

where $D_\mu \equiv \partial_\mu + ig' \frac{Y}{2} B_\mu(x) + ig \frac{\sigma_a}{2} W_\mu^a(x)$ is the covariant derivative defined in the EW theory. Here μ is the Higgs mass parameter and λ is the self-coupling constant.

Let's use the potential to express the second and third terms in the Lagrangian:

$$V(\phi) = \mu^2 \phi^\dagger \phi + \lambda (\phi^\dagger \phi)^2. \quad 2.29$$

In order to enable the potential to have a minimum value, $\lambda > 0$ is required. When $\mu^2 \geq 0$, the

potential will take a simple minimum at $\phi_0 = \begin{pmatrix} 0 \\ 0 \end{pmatrix}$. When $\mu^2 < 0$, the potential takes its minimum

at:

$$|\phi_0| = \sqrt{\frac{-\mu^2}{2\lambda}} = \frac{v}{\sqrt{2}}, \quad 2.30$$

where $v = \sqrt{\frac{-\mu^2}{\lambda}}$ is called the vacuum expectation value (vev). In this case, the potential has

infinite ground states which are symmetric under a U(1) phase transformation.

$$\phi_0 = \frac{v}{\sqrt{2}} e^{i\theta}. \quad 2.31$$

However, choosing a particular solution θ will spontaneously break the symmetry.

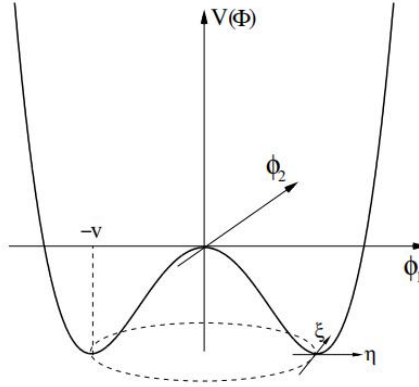


Figure 2.1 Potential V of a scalar field ϕ with $\mu^2 < 0$ and $\lambda > 0$

For simplicity, we will choose the ground state to be: $\phi_0 = \frac{1}{\sqrt{2}} \begin{pmatrix} 0 \\ v \end{pmatrix}$, because particles are understood to be excitation on the ground state field, we will expand the field in the vicinity of the ground state using perturbation theory, which will result in:

$$\phi(x) = \begin{pmatrix} \theta_1(x) + i\theta_2(x) \\ \frac{1}{\sqrt{2}}[v + H(x)] - i\theta_3(x) \end{pmatrix} \approx e^{i\frac{\sigma_a \theta_a(x)}{2v}} \begin{pmatrix} 0 \\ \frac{1}{\sqrt{2}}[v + H(x)] \end{pmatrix}. \quad 2.32$$

Due to SU(2) invariance, it's possible to choose $\theta(x)=0$. Then after taking $\phi(x)$ back to the Lagrangian, we are able to extract the mass terms of the W^\pm and Z^0 bosons:

$$m_W = \frac{1}{2}vg, m_Z = \frac{1}{2}v\sqrt{g^2 + g'^2}, \quad 2.33$$

while the photon remains massless.

The final form of the Lagrangian is written as:

$$L_{Higgs} = \frac{1}{2} \partial_\mu H \partial^\mu H + (v + H)^2 \left(\frac{g^2}{4} W_\mu^+ W^\mu + \frac{g^2}{8 \cos^2 \theta_W} Z_\mu Z^\mu \right) - \lambda v^2 H^2 - \lambda v H^3 - \frac{\lambda}{4} H^4, \quad 2.34$$

from which we can obtain the Higgs mass:

$$m_H = \sqrt{-2\mu^2} = v\sqrt{2\lambda}. \quad 2.35$$

Fermions can also have masses by introducing Higgs Yukawa couplings. Let's take the first generation of fermions as a simple example, where the Yukawa Lagrangian is written as:

$$L_{Yukawa} = -\frac{1}{\sqrt{2}}(v + H)(c_1 \bar{d}d + c_2 \bar{u}u + c_3 \bar{e}e), \quad 2.36$$

and the corresponding mass terms are:

$$m_d = c_1 \frac{v}{\sqrt{2}}, m_u = c_2 \frac{v}{\sqrt{2}}, m_e = c_3 \frac{v}{\sqrt{2}}. \quad 2.37$$

Finally, the SM Lagrangian is the summation of the different components:

$$L_{SM} = L_{QCD} + L_{EW} + L_{Higgs} + L_{Yukawa} \quad 2.38$$

2.2 Top quark physics

The top quark is the heaviest particle in the SM, and was first observed in 1995, by the CDF and D0 Collaboration at Fermilab [4][5]. Recent ATLAS measurement [6] of the top quark mass from direct top quark decay gives : $m_{top} = 172.69 \pm 0.48 \text{ GeV}$.

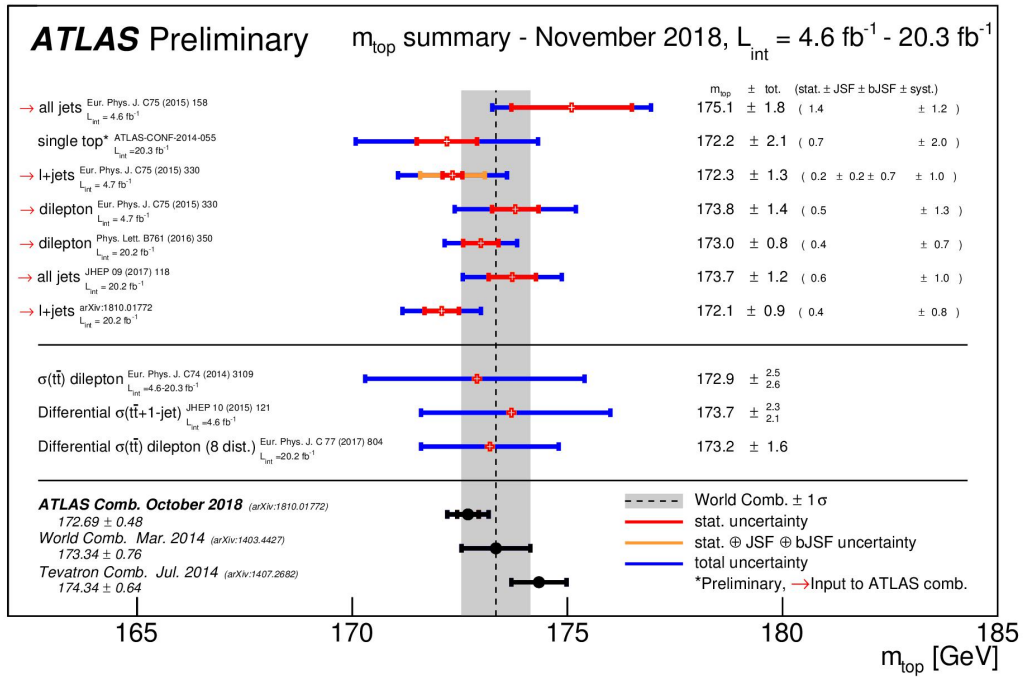


Figure 2.2 Summary of the ATLAS measurements of the top quark mass

Top quark is mainly produced in pairs by the QCD interaction and decays exclusively into a W boson and a bottom quark. Feynman diagram of the top quark decay is shown in Figure 2.3.

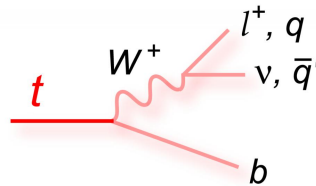


Figure 2.3 Feynman diagram of the top quark decay

Recent ATLAS inclusive $t\bar{t}$ cross section measurements [7] give the following results:

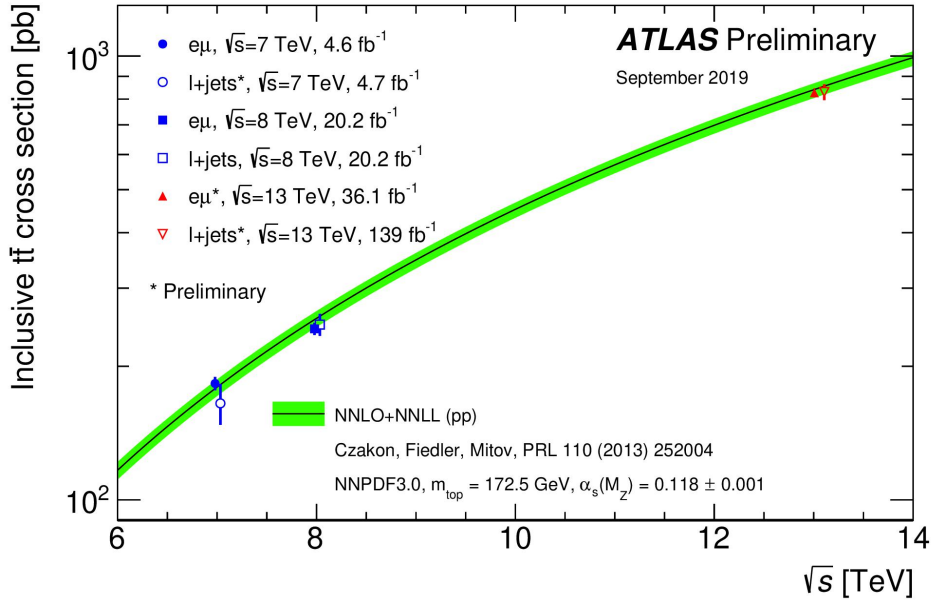


Figure 2.4 Summary of ATLAS measurements of the top-pair production cross-section as a function of the centre-of-mass energy compared to the NNLO QCD calculation complemented with NNLL resummation.

At a center of mass energy of $\sqrt{s} = 13$ TeV, the measured inclusive $t\bar{t}$ production cross section is $\sigma_{t\bar{t}} = 826.4 \pm 3.6 \pm 19.5 \text{ pb}$.

Apart from the previous measurements, there are also a lot of other interesting studies related to top quarks, such as charge asymmetry [8], spin correlation [8], and Flavor Changing Neutral Currents (FCNCs) [9] etc.

2.3 Higgs boson physics

The Higgs boson plays an essential role in the SM as its couplings explain how particles acquire masses. But it has not been observed in previous experiments until it was discovered at LHC in year 2012, by both ATLAS [12] and CMS [13] experiments.

2.3.1 Higgs production mechanisms

At LHC, the Higgs Boson can be produced through four major mechanisms. Gluon-gluon fusion (ggF), vector boson fusion (VBF), associated production with a gauge boson (VH) and associated production with a top anti-top quark pair ($t\bar{t}H$). Examples of Feynman diagrams for each production mode are shown in Figure 2.5.

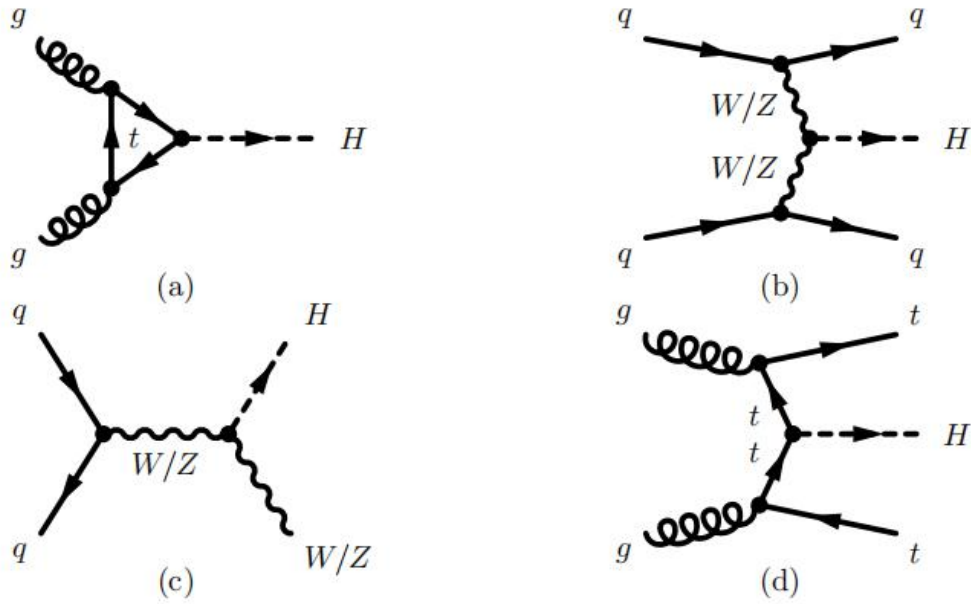


Figure 2.5 Feynman diagrams for the four dominant SM Higgs boson production mechanisms at the LHC: (a) gluon fusion (ggF); (b) vector boson fusion (VBF); (c) associated production with a gauge boson (VH); (d) associated production with a top quark pair ($t\bar{t}H$).

Among the four production modes, gluon fusion is the dominant one in the proton-proton collision environment, followed by vector boson fusion, which is an order of magnitude smaller than ggF. Associated production with a gauge boson (VH) comes next. Finally, associated production with a top quark pair is a very rare case, and also occurs in low mass Higgs cases. However, this production mode is very important as it provides a direct way to measure the top Yukawa coupling strength.

Theoretical Higgs production cross-section [10] is shown in Figure 2.6.

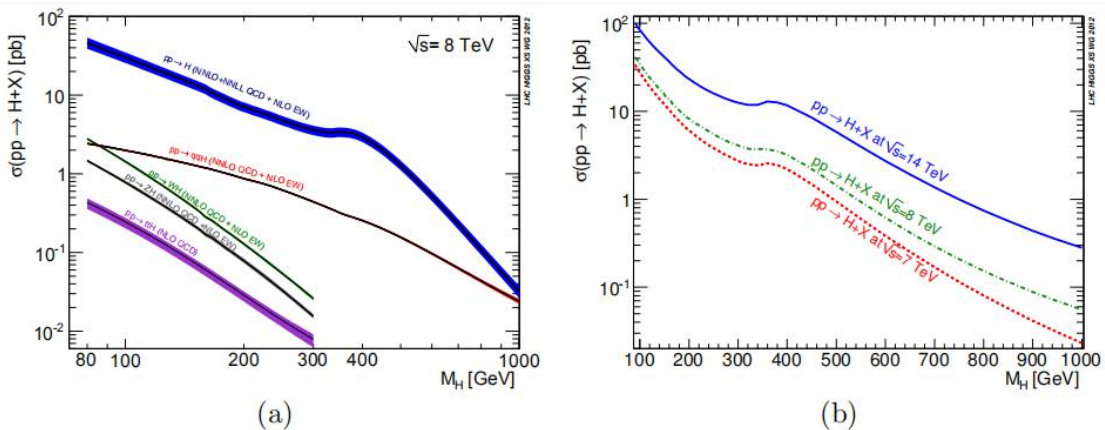


Figure 2.6 (a) Cross-sections for different SM Higgs production mechanisms at the LHC, as a function of the Higgs mass (b) Total cross-section for SM Higgs production at the LHC, as a function of the Higgs mass (with $M_H = 125$ GeV measured in experiment)

As now the Higgs boson is discovered, the Higgs mass is measured to be around 125 GeV.

2.3.2 Higgs Decays

The Higgs boson has a very short life time and will decay to other particles immediately when they are produced. There are several decay channels of the Higgs boson, and the corresponding branching ratio as a function of the Higgs mass [11] is shown in Figure 2.7.

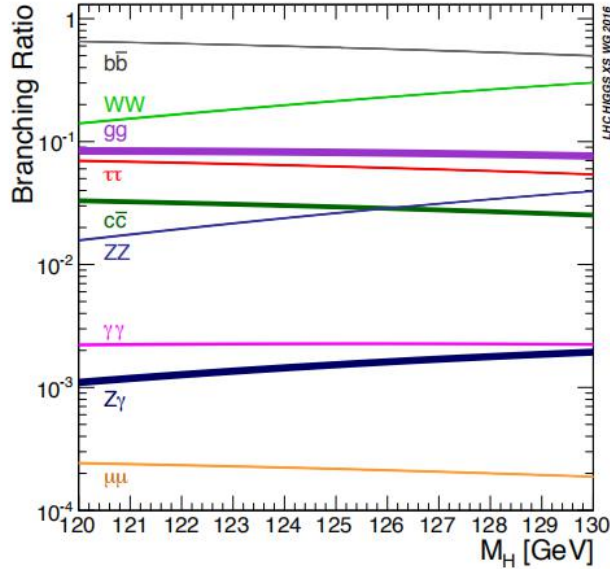


Figure 2.7 Branching ratios of the SM Higgs boson as a function of its mass

Decay mode	Branching fraction	Uncertainty [%]
	$m_H = 125 \text{ GeV}$	
$H \rightarrow b\bar{b}$	5.77×10^{-1}	+3.21 -3.27
$H \rightarrow WW^*$	2.15×10^{-1}	+4.26 -4.20
$H \rightarrow gg$	8.57×10^{-2}	+10.22 -9.98
$H \rightarrow \tau\tau$	6.32×10^{-2}	+5.71 -5.67
$H \rightarrow c\bar{c}$	2.91×10^{-2}	+12.17 -12.21
$H \rightarrow ZZ^*$	2.64×10^{-2}	+4.28 -4.21
$H \rightarrow \gamma\gamma$	2.28×10^{-3}	+4.98 -4.89
$H \rightarrow Z\gamma$	1.54×10^{-3}	+9.01 -8.83
$H \rightarrow \mu\mu$	2.19×10^{-4}	+6.01 -5.86
$\Gamma_H^{\text{total}} [\text{GeV}]$	4.07×10^{-3}	+3.97 -3.93

Table 2.2 Branching ratios and total width of the SM Higgs boson at $m_H = 125 \text{ GeV}$

2.3.3 Discovery of the Higgs boson

On the 4th of July 2012, ATLAS and CMS announced the discovery of a newly found SM Higgs-like particle with the mass around 125 GeV [12][13]. The excess over background was compatible with the SM prediction. The discovery was based on the combined results of different search channels, while $H \rightarrow \gamma\gamma$, $H \rightarrow ZZ \rightarrow 4l$ and $H \rightarrow WW \rightarrow l\nu l\nu$ channels offered the dominant contribution in terms of the sensitivity.

The combined observed significance around $M_H = 125$ GeV was 5.9σ for ATLAS and 5.0 for CMS (shown in Figure 2.8), both reaching the five sigma threshold for the discovery announcement.

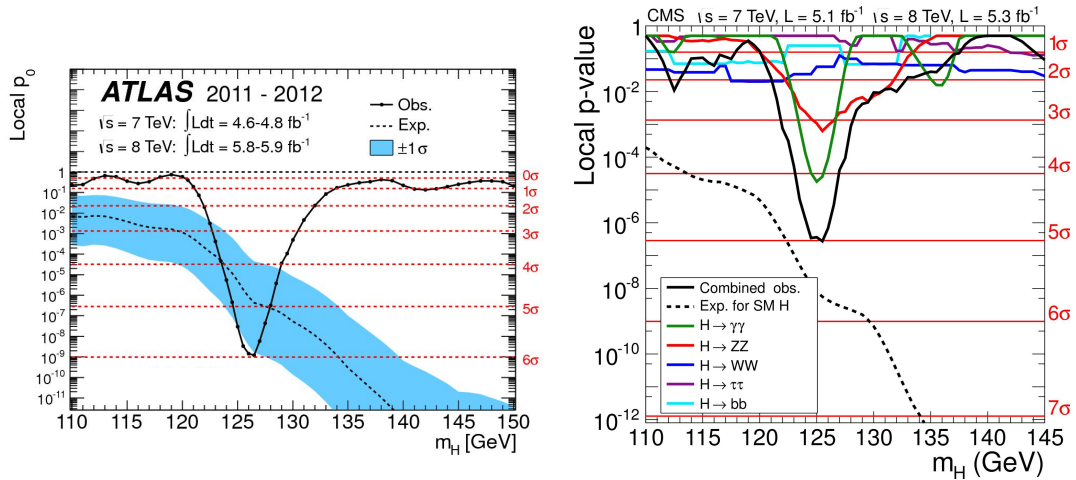


Figure 2.8 The observed local p value as a function of the SM Higgs boson mass from ATLAS(left) and CMS(right) respectively

2.3.4 Properties of the Higgs boson

After the discovery, different measurements of the new particle were made in order to test the agreement with the SM prediction.

The latest result of the Higgs mass measurement by the ATLAS experiment is shown in Figure 2.9 [14].

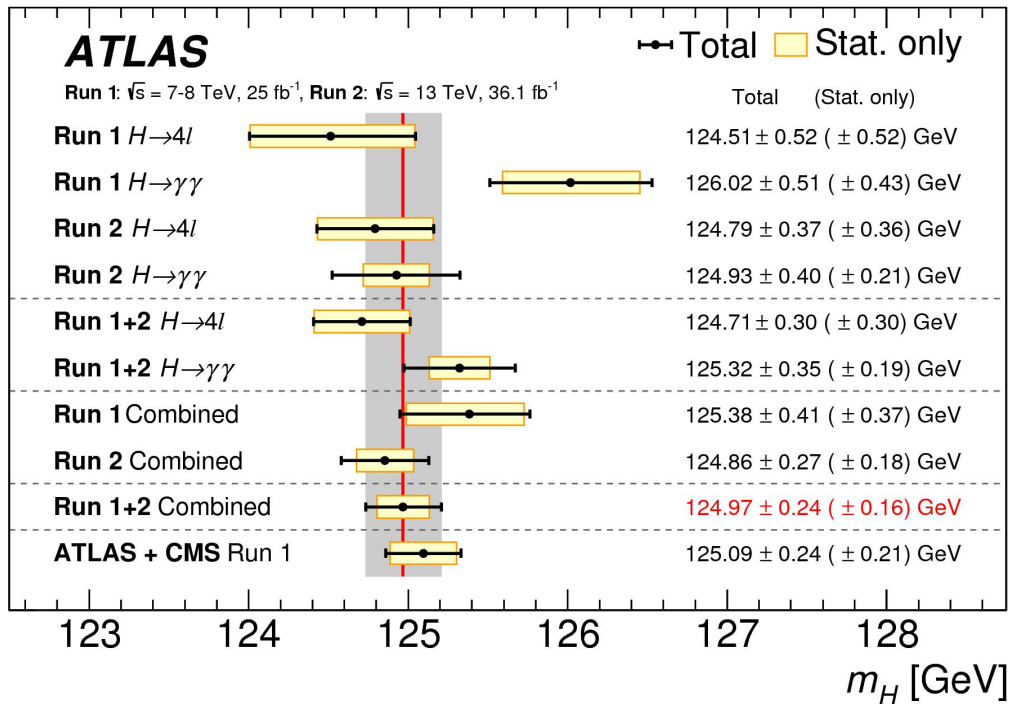


Figure 2.9 Summary of the measurements of the SM Higgs boson mass

The Higgs mass is measured to be $M_H = 124.97 \pm 0.24 \text{ GeV}$, combining ATLAS Run1 and Run2 dataset. The measured signal strengths (the ratio between the observed cross section and the predicted cross section) in different Higgs production modes are shown in Figure 2.10 [15].

The results show that the measured Higgs production cross section times branching ratio is in good agreement with the SM prediction.

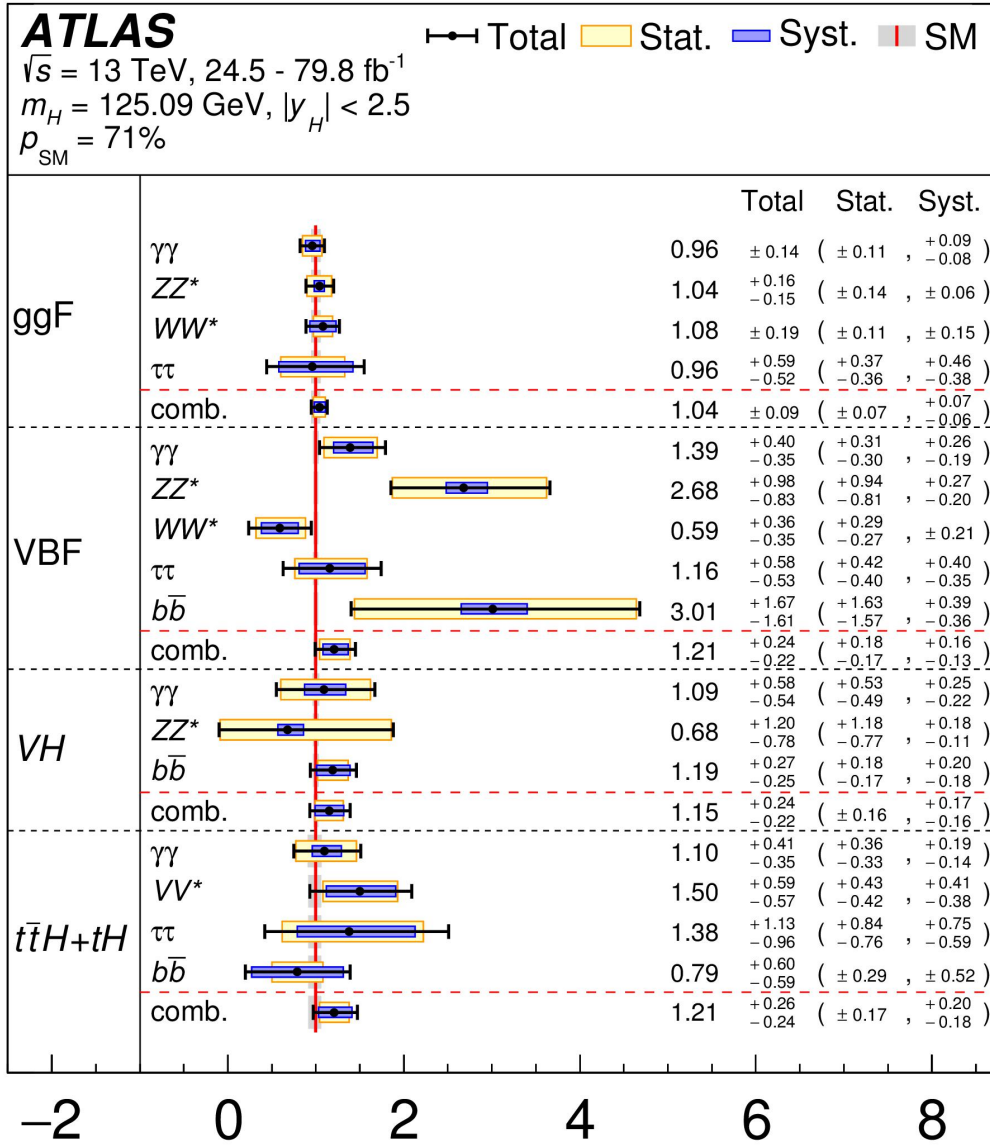


Figure 2.10 Cross sections times branching fraction for different Higgs production mechanisms in each relevant decay mode, normalized to their SM predictions.

Besides, the Higgs Yukawa coupling to other particles is also a quantity of interest. The measured universal coupling strength scale factors κ_V (for all the vector bosons) and κ_F (for all the fermions) are shown in Figure 2.11 [15]. For a given production process or decay mode j , the corresponding coupling strength scale factor is defined as $\kappa_j^2 = \sigma_j / \sigma_j^{\text{SM}}$, or $\kappa = \Gamma_j / \Gamma_j^{\text{SM}}$, where σ is the production cross section and Γ is the partial decay width.

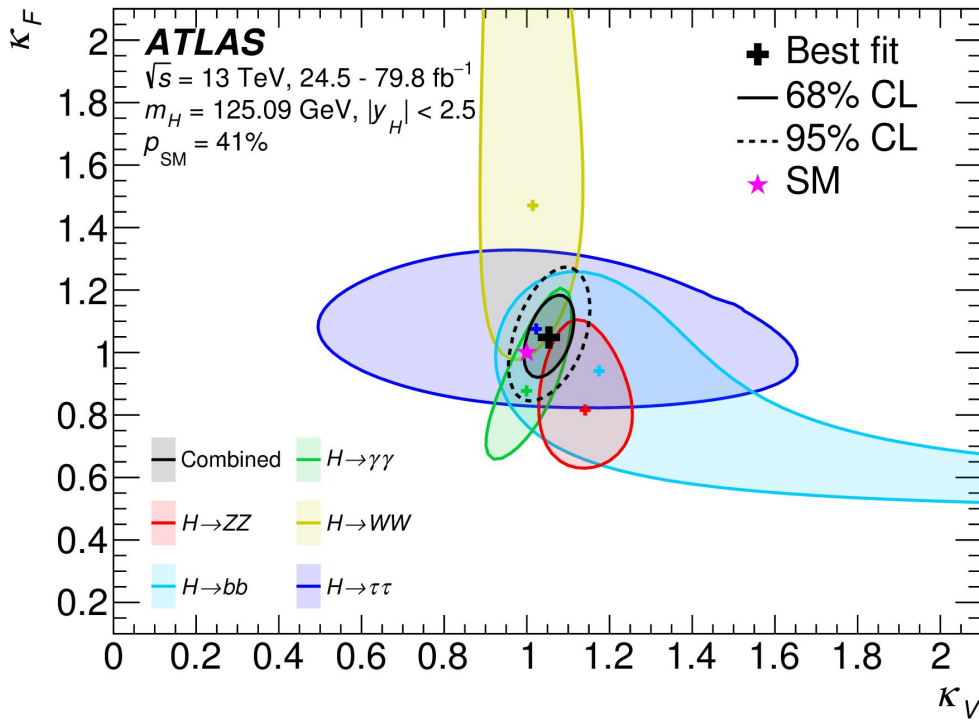


Figure 2.11 Negative log-likelihood contours at 68% and 95% CL in the κ_V^f, κ_F^f plane for the individual decay modes and their combination

The best fitted values are:

$$\kappa_V = 1.05 \pm 0.04, \kappa_F = 1.05 \pm 0.09.$$

2.4 Top Yukawa coupling and $t\bar{t}H$ production

The Higgs Yukawa coupling strength is proportional to the fermion's mass, and since the top quark is the heaviest particle in the SM, its Yukawa coupling is predicted to be close to unity. Precise measurement of this coupling is important not only as a test of the SM, but also a probe to new physics. However, currently the measurement of this coupling [16] relies on the indirect top quark contribution to gluon-gluon fusion production and diphoton decay loops, assuming no BSM contribution. Since the top quark is heavy and very sensitive to BSM physics, the assumption of no BSM contribution may not be reliable, and the coupling of the top quark to other particles may also contribute in the indirect measurement. Therefore, a direct measurement of the top Yukawa coupling is needed in order to provide a more precise result and also reduce the model dependence in the extraction of the top Yukawa coupling.

The associated production of the Higgs boson and a top quark pair ($t\bar{t}H$) is the process which provides a direct probe of the top quark Yukawa coupling. This is a tree-level process at lowest order in perturbation theory.

Example of tree-level Feynman diagrams for $t\bar{t}H$ process are shown in Figure 2.12.

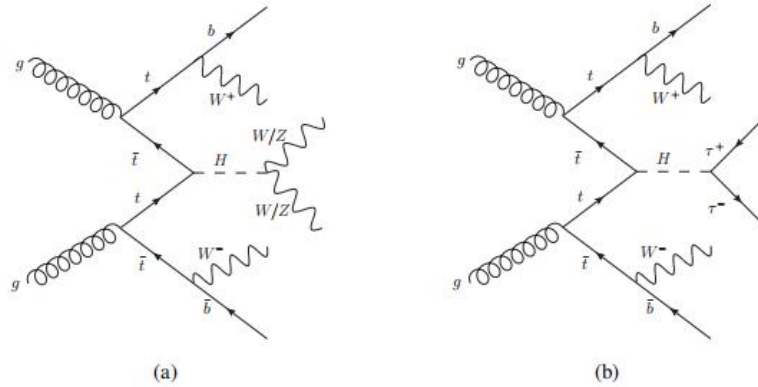


Figure 2.12 Examples of tree-level Feynman diagrams for the production of the Higgs boson in association with a pair of top quarks.

At the LHC, the production cross section of $t\bar{t}H$ is two orders of magnitude lower than the inclusive Higgs production, but this process can still be searched for due to the distinctive features of top quark final state.

The $t\bar{t}H$ process was discovered experimentally by ATLAS [17], using a dataset which corresponds to an integrated luminosity of 79.8fb^{-1} . The results were based on the combination of different Higgs boson decay channels, including $H\rightarrow b\bar{b}$, $H\rightarrow WW$, $H\rightarrow\tau\tau$, $H\rightarrow\gamma\gamma$ and $H\rightarrow ZZ$. The observed significance is 5.8 standard deviations, compared with an expected significance of 4.9 standard deviations. CMS also reported discovery of the $t\bar{t}H$ production [18] with an observed (expected) significance of 5.2 (4.2) standard deviations.

The ATLAS measurement of the $t\bar{t}H$ production cross section at 13 TeV gives: $\sigma_{t\bar{t}H} = 670 \pm 90(\text{stat.})_{-100}^{+110}(\text{syst.})\text{fb}$, which is in agreement with the SM prediction.

2.5 Four-top-quark production

As previously shown, top quark physics is a rich physics field. It plays an important role in the SM precision measurements, and is also a good probe to physics beyond the Standard Model. Among all the studies related to the top quark, four-top-quark production is the one with the highest system energy, and is thus of particular interest.

Four-top-quark production is predicted by the SM with an extremely small cross section. The latest SM prediction [19] for the four-top-quark production cross section gives: $\sigma_{t\bar{t}t\bar{t}} = 11.97_{-21\%}^{+18\%}\text{fb}$ at $\sqrt{s} = 13\text{TeV}$, in which the leading order component is $\sigma_{t\bar{t}t\bar{t}} = 7.59_{-36\%}^{+64\%}\text{fb}$. Recent analysis [20] reported an observed (expected) upper limit on the SM 4 top production cross section of 69 (29) fb. An example of Feynman diagram for the SM 4 tops production [21] is shown in Figure 2.13.

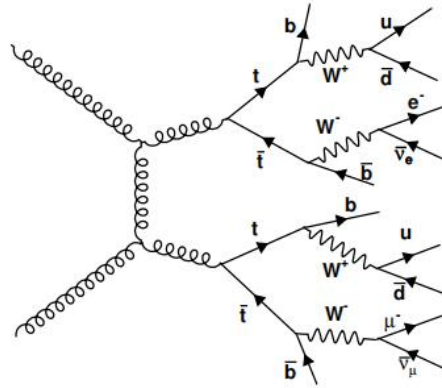


Figure 2.13 Example of Feynman diagram for the Standard Model four-top-quark production

Apart from that, the four-top-production cross section is enhanced in and thus sensitive to many BSM scenarios, such as Effective Field Theory [22], where the $t\bar{t}t\bar{t}$ production cross section is 926.3 fb for the contact interaction coupling constant $C_{4t} / \Lambda^2 = -4\pi TeV^{-2}$ by running MadGraph, Vector-like Quarks (VLQs) [23], Two Higgs Doublet Model (2HDM) [24], Universal Extra Dimension / Real Projective Plane Model (2UED/RPP) [25] e.t.c. Examples of Feynman diagrams for each model are shown in Figure 2.14-2.17. Furthermore, the four-top-production is also a powerful tool to constrain the top Yukawa coupling [26].

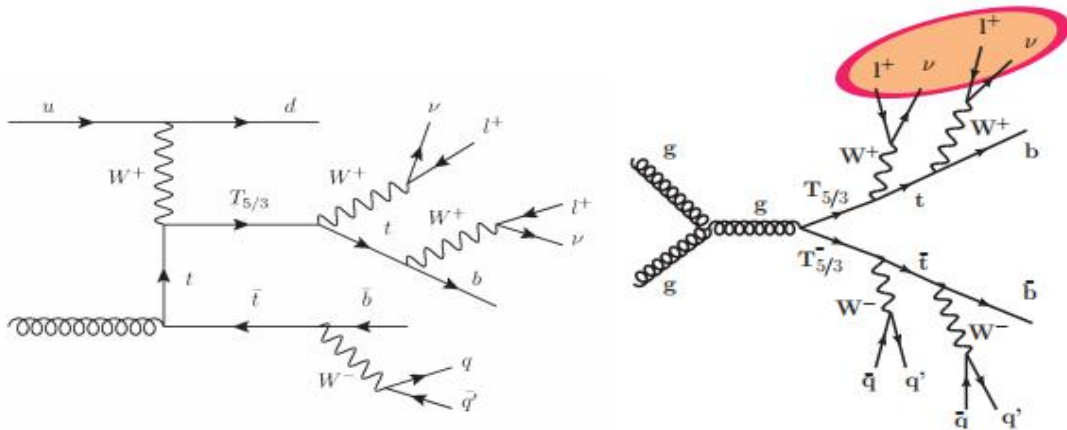


Figure 2.14 Feynman diagram for vector-like $T_{5/3}$ single (left) and pair production (right).

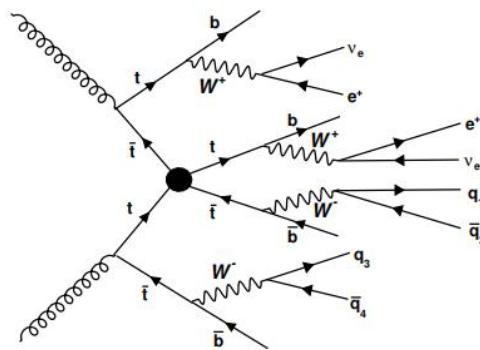


Figure 2.15 Example of Feynman diagram of four-top-quark production in Effective Field Theory with contact interaction.

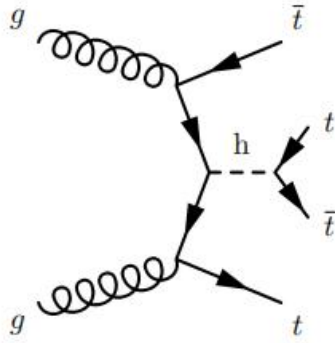


Figure 2.16 Example of Feynman diagram of four-top-quark production in 2HDM 2UED/RPP (Universal Extra Dimension / Real Projective Plane) model

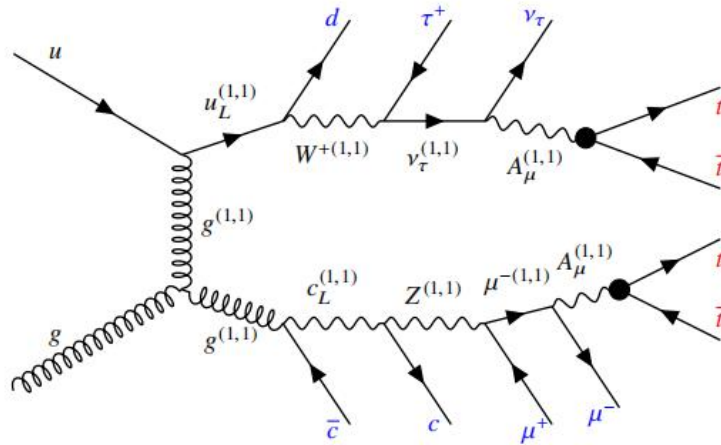


Figure 2.17 Example of Feynman diagram of four-top-quark production in 2UED/RPP model

Reference:

- [1] F. Halzen and Alan D. Martin. QUARKS AND LEPTONS: AN INTRODUCTORY COURSE IN MODERN PARTICLE PHYSICS. 1984. ISBN 0471887412, 9780471887416.
- [2] C. Patrignani and Particle Data Group. Review of particle physics. Chinese Physics C, 40(10):100001, 2016.
- [3] Joana Machado Miguens, Observation and measurement of the Higgs boson in the WW^* decay channel with ATLAS at the LHC, CERN-THESE-2015-300.
- [4] CDF Collaboration, Observation of Top Quark Production in pp Collisions with the Collider Detector at Fermilab, Physical Review Letters 74, (1995) 2626-2631, arXiv:hep-ex/9503002.
- [5] D0 Collaboration, Observation of the Top Quark, Physical Review Letters 74, (1995) 2632-2637, arXiv:hep-ex/9503003.
- [6] ATLAS Collaboration, Top Quark Mass Summary Plots, [ATL-PHYS-PUB-2019-036 \(2019\)](#).
- [7] ATLAS Collaboration, Top working group cross-section Summary Plots, [ATL-PHYS-PUB-2019-035 \(2019\)](#).
- [8] ATLAS Collaboration, Top working group Summary Plots - Autumn 2018, [ATL-PHYS-PUB-2018-034 \(2018\)](#).
- [9] ATLAS Collaboration, Search for top-quark decays $t \rightarrow Hq$ with 36 fb^{-1} of pp collision data at $\sqrt{s} = 13$ TeV with the ATLAS detector, JHEP 05 (2019) 123, arXiv:1812.11568 [hep-ex].
- [10] The LHC Higgs Cross Section Working Group, “LHC Higgs Cross Section Working Group.” <https://twiki.cern.ch/twiki/bin/biew/LHCPhysics/LHCHXSWG>.
- [11] ATLAS Collaboration, Preliminary results on the muon reconstruction efficiency, momentum resolution, and momentum scale in ATLAS 2012 pp collision data, [ATLAS-CONF-2013-088 \(2013\)](#).
- [12] ATLAS Collaboration, Observation of a new particle in the search for the Standard Model Higgs boson with the ATLAS detector at the LHC, Physics Letters B 716 (2012) 1-29, arXiv:1207.7214 [hep-ex].
- [13] CMS Collaboration, Observation of a new boson at a mass of 125 GeV with the CMS experiment at the LHC, Physics Letters B 716 (2012) 30, arXiv:1207.7235 [hep-ex].
- [14] ATLAS Collaboration, Measurement of the Higgs boson mass in the $H \rightarrow ZZ^* \rightarrow 4l$ and $H \rightarrow \gamma\gamma$ channels with $\sqrt{s} = 13$ TeV pp collisions using the ATLAS detector, Phys. Lett. B 784 (2018) 345.
- [15] ATLAS Collaboration, Combined measurements of Higgs boson production and decay using up to 80 fb^{-1} of proton-proton collision data at $\sqrt{s} = 13$ TeV collected with the ATLAS experiment, Phys. Rev. D 101 (2020) 012002, arXiv: 1909.02845 [hep-ex].
- [16] ATLAS and CMS Collaborations, Measurements of the Higgs boson production and decay rates and constraints on its couplings from a combined ATLAS and CMS analysis of the LHC pp collision data at $\sqrt{s} = 7$ and 8 TeV, JHEP 08 (2016) 045, arXiv: 1606.02266 [hep-ex].
- [17] ATLAS Collaboration, Observation of Higgs boson production in association with a top quark pair at the LHC with the ATLAS detector, Phys. Lett. B 784 (2018) 173, arXiv: 1806.00425 [hep-ex].
- [18] CMS Collaboration, Observation of $t\bar{t}H$ production, Phys. Rev. Lett. 120, 231801 (2018), arXiv: 1804.02610 [hep-ex].
- [19] R. Frederix, D. Pagani and M. Zaro, Large NLO corrections in $t\bar{t}W^\pm$ and $t\bar{t}t$ hadroproduction from supposedly subleading EW contributions, JHEP 02 (2018) 031, arXiv:

1711.02116 [hep-ph].

[20] ATLAS Collaboration, Search for new phenomena in events with same-charge leptons and b-jets in pp collisions at $\sqrt{s}=13$ TeV with the ATLAS detector, JHEP 12 (2018) 039, arXiv: 1807.11883 [hep-ex].

[21] ATLAS Collaboration, Search for new physics using events with b-jets and a pair of same charge leptons in pp collisions from 2015-16 at $\sqrt{s}=13$ TeV with the ATLAS detector, [ATL-COM-PHYS-2016-1474](#).

[22] C. Degrande et al., JHEP 1103 (2011) 125, arXiv: 1010.6304 [hep-ph].

[23] J.A.Aguilar-Saavedra, R. Benbrik, S. Heinemeyer, M. Perez-Victoria, Phys. Rev.D 88 (2013) 094010, arXiv: 1306.0572 [hep-ph].

[24] G. Branco et al., Phys.Rept. 516 (2012) 1, arXiv: 1106.0034 [hep-ph].

[25] G. Cacciapaglia, A. Deandrea, and J. Llodra-Perez, JHEP 1003 (2010) 083, arXiv: 0907.4993 [hep-ph].

[26] Qing-Hong Cao, Shao-Long Chen, Yandong Liu, Phys. Rev. D 95, 053004 (2017), arXiv: 1602.01934 [hep-ph].

Chapter 3

The Large Hadron Collider and the ATLAS Experiment

3.1 LHC

CERN's Accelerator Complex

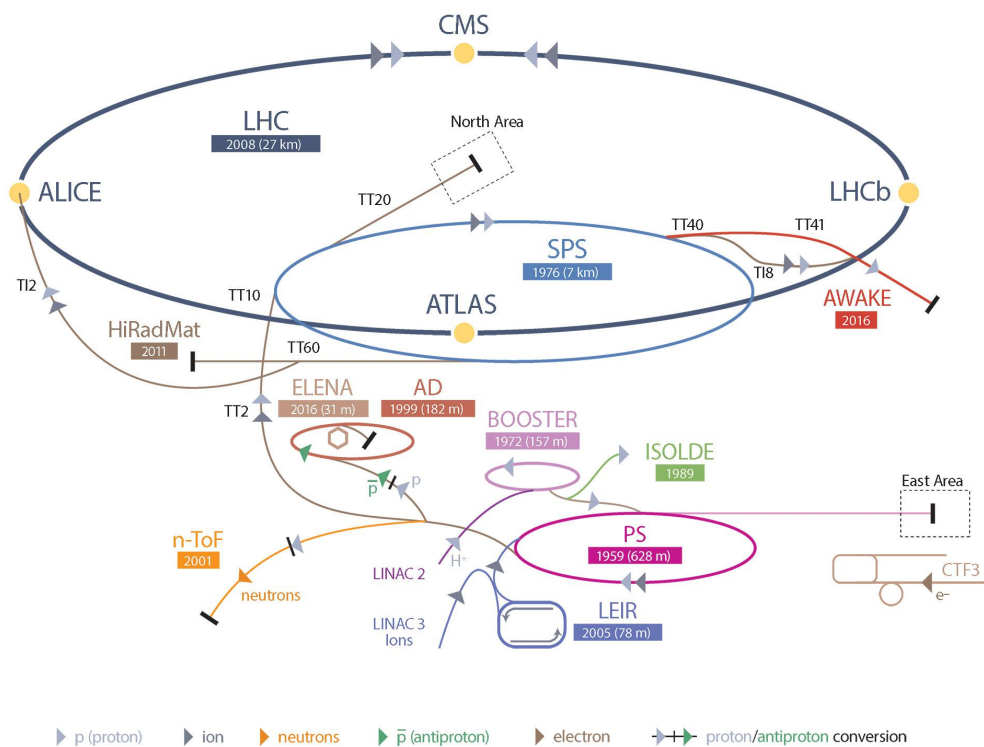


Figure 3.1 The accelerator complex at CERN

CERN(European Organization for Nuclear Research) is located on the border between Switzerland and France. It is a large organization involving tens of thousands of scientists and students from all over the world, which makes it the world's center for experimental high energy physics nowadays.

The LHC[1] is the representative of the high energy frontier in experimental particle physics. It is actually the last piece of a large accelerator system at CERN. The whole procedure starts with the production of the protons, which is achieved with a small hydrogen bottle. The original protons are injected into the LINAC 2 for the first step of acceleration, where the beam energy can be raised up to 50 MeV. Then the protons will travel successively through a circular Proton Synchrotron Booster (PSB) and a Proton Synchrotron (PS), where the beam energy will be increased to 1.4 GeV and 25 GeV respectively. Finally, the Super Proton Synchrotron (SPS)

increases the beam energy to 450 GeV, and transfers the protons in bunches to both LHC rings, where the protons are accelerated to reach the nominal energy of 6.5 TeV per beam.

The LHC is installed in a tunnel which is around 26.7 km in circumference and lies around 100 meters underground. It is designed to operate at center of mass energy (CME) of 14 TeV, which corresponds to 7 TeV for each proton beam. Because of this extremely high energy environment, it is only feasible by superconducting techniques. Therefore, the LHC is composed of thousands of superconducting Niobium-Titanium magnets, together with superconducting resonant-frequency (RF) cavities. The magnets system is used to steer and focus the particle beams, while the resonant-frequency cavities are designed to boost the beam to higher energies.

There are several interaction points (IPs) in different regions of the tunnel, where two beam pipes are merged into a single pipe. 4 detectors are built around these specific interaction points. Namely, they are ATLAS (A Toroidal LHC ApparatuS) at IP1, ALICE (A Large Ion Collider Experiment) at IP2, CMS (Compact Muon Solenoid) at IP5 and LHCb (Large Hadron Collider beauty) at IP8. Among the four detectors, ATLAS and CMS are general purpose detectors which are designed for various types of physics analyses. ALICE is a specialized detector for the dedicated study of heavy ion physics. LHCb is also a specialized detector for dedicated study of b-quark physics.

3.2 The ATLAS detector

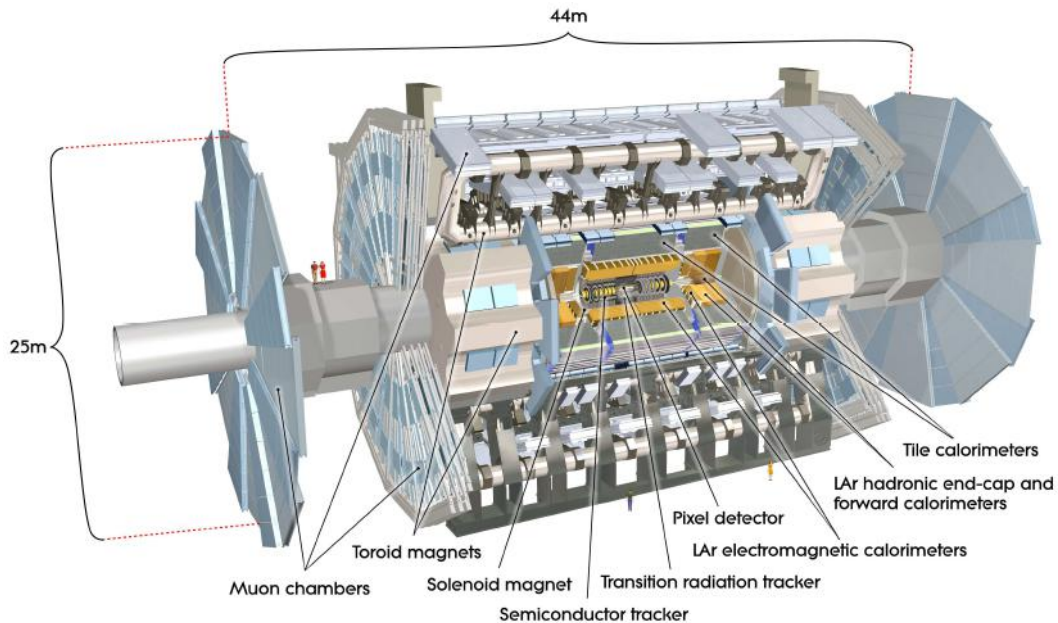


Figure 3.2 Diagram of the ATLAS detector system [4]

ATLAS is a multi-purpose detector [2][3] with 25m in height, 44m in length and approximate 7000 tons in weight. The sub-detector systems of ATLAS include: the inner detector (ID) composed of various tracking devices, the calorimeters for energy measurement and the muon spectrometer for muon detection. A magnet system is installed for momentum measurement and charge identification. In addition, there is a trigger and data acquisition (TDAQ) system which is meant to collect LHC data with high performance and reasonable rate.

ATLAS uses a right-handed coordinate system, of which the center is located at the nominal

interaction point. The beam line is the z-axis and the x-y plane (the transverse plane) is perpendicular to the beam line. Transverse plane is very important in physics analysis, because the initial momentum of the collision system is 0 along the transverse plane in the lab rest frame, thus the momentum conservation law can be applied within that plane.

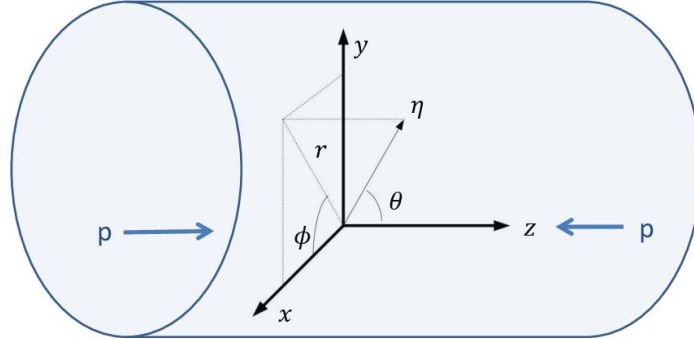


Figure 3.3 Illustration of the ATLAS coordinate system

ATLAS has a roughly cylindrical symmetric structure, so the cylindrical and polar coordinates are used for mathematical calculation. The radial coordinate R stands for the transverse distances from the beam line. The azimuthal angle ϕ stands for the angle from the x-axis in the x-y plane and the polar coordinate θ is the angle away from z-axis. The pseudo-rapidity $\eta = -\ln(\tan(\frac{\theta}{2}))$ is often used in analysis instead of the original polar angle. This is because that the differences in pseudo-rapidity are invariant under boosts along z-axis, so that one can perform a Lorentz boost on the data by just translating the directional distribution along the η axis. In the η - ϕ coordinate space, a distance defined as $\Delta R = \sqrt{\Delta\eta^2 + \Delta\phi^2}$ is commonly used to measure the spatial distance between two particles.

The required resolution and the η coverage for the different detector components are shown in Table 3.1 [2]:

Detector component	Required resolution	η coverage	
		Measurement	Trigger
Tracking	$\sigma_{p_T} / p_T = 0.5\% p_T \oplus 1\%$	± 2.5	
EM calorimeter (barrel and end-cap)	$\sigma_E / E = 10\% / \sqrt{E} \oplus 0.7\%$	± 3.2	± 2.5
Hadronic CAL (barrel and end-cap)	$\sigma_E / E = 50\% / \sqrt{E} \oplus 3\%$	± 3.2	
Hadronic CAL (forward)	$\sigma_E / E = 100\% / \sqrt{E} \oplus 10\%$	$3.1 < \eta < 4.9$	
Muon spectrometer	$\sigma_{p_T} / p_T = 10\%$ at $p_T = 1$ TeV	± 2.7	± 2.4

Table 3.1 Designed performance goals for different components of the ATLAS detector

3.2.1 Inner detector

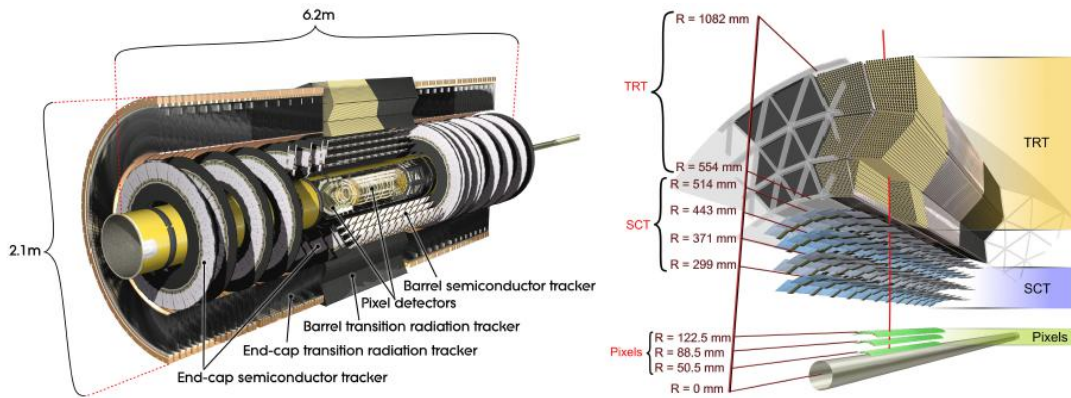


Figure 3.4 Overview picture of the ATLAS inner detector (left) and illustration of the inner detector in the barrel region (right) [4]

The Inner Detector (ID) is the innermost layer of ATLAS, which is closest to the interaction point. It is composed of the Insertable B Layer (IBL), the Pixel detector, the SemiConductor Tracker (SCT) and the Transition Radiation Tracker (TRT). The IBL is newly added for Run 2 operation. It is added between a new beam pipe and the previously innermost Pixel layer. The IBL preserves robustness of the tracking quality and the resolution on the impact parameter measurements. The Pixel detector is a silicon pixel precision tracking device placed as the second of the inner detector. It provides a position measurement accuracy of $10 \mu\text{m}^2$ (in R- ϕ plane) and of $115 \mu\text{m}$ (for z in the barrel region and R in the end-cap region). The SCT is the third layer of ATLAS. It is a precision silicon microstrip detector which contains a large number of readout channels. It provides a position measurement accuracy of $17 \mu\text{m}^2$ (in R- ϕ plane) and of $580 \mu\text{m}$ (for z in the barrel region and R in the end-cap region). The TRT is the outermost layer of the ID. It is a straw tube gaseous detector which only provides R- ϕ measurement. The accuracy of the TRT measurement is around $130 \mu\text{m}^2$, which is worse compared to the Pixel and the SCT. However, it has the advantage of a larger number of measurements and longer level arm. The sensitive volume of the TRT covers a large radial range, allowing for significant contributions to momentum measurement.

3.2.2 Calorimeter

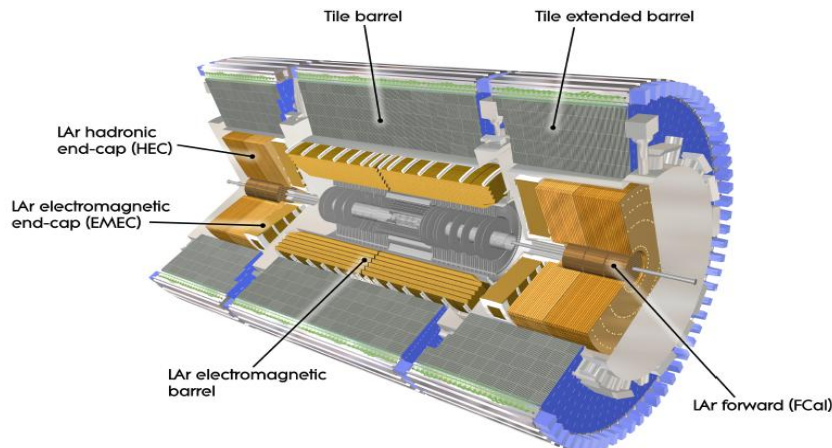


Figure 3.5 Illustration of the ATLAS calorimeters [4]

The ATLAS calorimeters [2] are sampling detectors, which means that they contain layers of sensitive medium alternating with layers of dense absorber material. Particles lose energy through interactions with the absorber medium, and then the sensitive medium generates signal which is proportional to the energy loss.

The innermost layer of the calorimeter system is composed of one EM calorimeter in the barrel (EMB), one EM calorimeter (EMEC) and one hadronic calorimeter (HEC) at each endcap, together with a forward calorimeter (FCal) which covers regions closest to the beam line. The outer layer of the system is formed by the hadronic TileCal calorimeter. The TileCal is composed of one central barrel and two extended barrels on each side. Generally, the calorimeters can provide energy and topology measurements over the range $|\eta| < 4.9$.

3.2.2.1 The EM calorimeter

The EM calorimeter uses liquid argon as active material and lead plates as absorber. The lead-LAr layers have accordion shaped geometry, which can provide complete ϕ symmetry without any azimuthal gaps.

In the barrel region, the EMB calorimeter covers regions of $|\eta| < 1.475$. In the end-caps, the EMEC calorimeter is divided into an outer wheel which covers regions of $1.375 < |\eta| < 2.5$ and an inner wheel which covers regions of $2.5 < |\eta| < 3.2$. In regions of $|\eta| < 2.5$, the EM calorimeter is segmented longitudinally into three layers, devoted to precision physics. The first layer is finely segmented in η , which provides accurate position measurement. The second layer has a segmentation of 0.025×0.025 in $\Delta\eta \times \Delta\phi$ space. This layer collects the largest fraction of the energy from EM shower. The third layer only collects the tail of EM shower, so it is less segmented in η . The inner layer end-cap wheel ($2.5 < |\eta| < 3.2$) is segmented into two sections only. The typical energy resolution of the EM calorimeter is $\sigma_E / E = 10\% / \sqrt{E} \oplus 0.7\%$.

3.2.2.2 The hadronic calorimeter

The hadronic calorimeter is composed of the TileCal in the barrel and the HEC in the end-caps. Generally, the hadronic calorimeter has around 10-19 interaction lengths, which can provide full containment of the hadronic showers produced in the LHC collisions. The TileCal uses plastic scintillator as active material, alternating with steel plates as absorber, and has a coverage of $|\eta| < 1.7$, while the extended barrels cover $0.8 < |\eta| < 1.7$. The HEC uses copper plates as absorber medium, interleaved with the LAr gaps, used as the active material, in a flat-plate design topology. The HEC has a coverage of $1.5 < |\eta| < 3.2$. Finally, the forward calorimeter (FCal) has a depth of approximately 10 interaction lengths and further extends the coverage of the calorimeter system up to $|\eta| < 4.9$. The typical energy resolution of the hadronic calorimeter is $\sigma_E / E = 50\% / \sqrt{E} \oplus 3\%$. The intrinsic resolution of the hadronic calorimeters is much worse than the EM calorimeters, because much of the energy is lost to the inelastic scattering of nucleons.

3.2.3 The Muon spectrometer

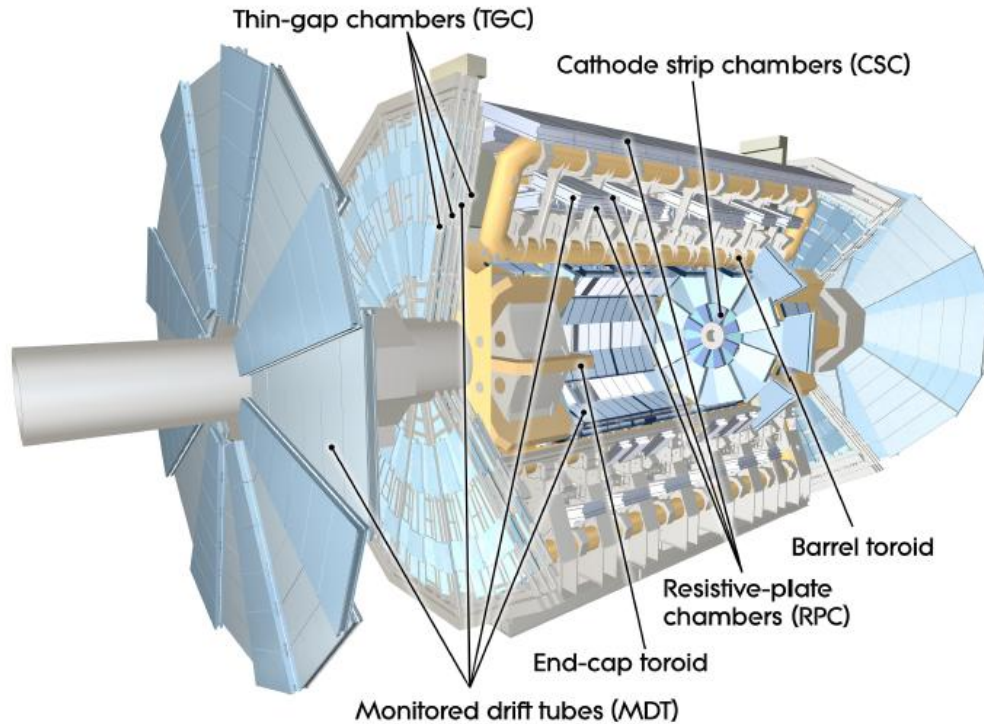


Figure 3.6 Illustration of the ATLAS Muon Spectrometer [4]

The Muon spectrometer (MS) [2] is the outermost part of the ATLAS detector. It is designed to detect muons and measure their momentum within $|\eta| < 2.7$, as well as triggering them within $|\eta| < 2.4$ region. The MS is composed of four subsystems, namely, Monitored Drift Tubes (MDT), Cathode Strip Chambers (CSC), Resistive Plate Chambers (RPC), and Thin Gap Chambers (TGC). In the barrel region, chambers are arranged in three cylindrical layers around the beam, while in the endcap region, layers are arranged to be perpendicular to the beam. The MDT and the CSC are designed for precision measurements of the muon momentum. The MDT covers regions of $|\eta| < 2.7$, and the CSC covers regions of $2.0 < |\eta| < 2.7$. The small coverage of the CSC is compensated by the capability of coping with higher background rate. The RPC and the TGC are designed to provide fast and robust readout, to be used by the trigger system, in the regions of $|\eta| < 1.05$ and $1.05 < |\eta| < 2.4$, respectively.

3.2.4 The Trigger system

The ATLAS trigger system is composed of three levels, namely, the level-1 Trigger (L1), the level-2 Trigger (L2) and the Event Filter (EF).

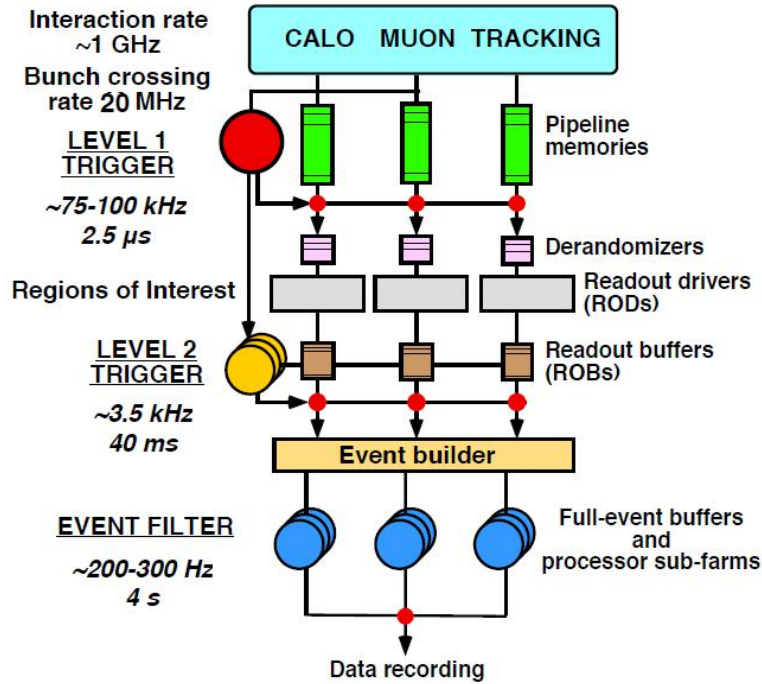


Figure 3.8 Illustration of the ATLAS Trigger and Data acquisition system [5]

The level-1 trigger is based on hardware, which is designed to reduce the event rate from the initial around 20 MHz bunch collision rate to about 75-100 kHz within $2.5 \mu s$. The L1 trigger consists of L1Calo and L1Muon, which have direct access to the detector and rely on the information of the calorimeter and the muon spectrometer respectively. The L1 trigger also defines several Regions-of-Interest (ROIs). These are typically small areas containing high energies. The typical ROI are defined using η - ϕ positions of the identified objects, information of the types of identified features and the passed thresholds.

The level-2 trigger is based on software, while it can also search for information from the inner detector to help its decision making. The L2 trigger is designed to further reduce the event rate from around 75 kHz (L1 output) to around 3.5kHz within 40 ms. The L2 trigger only selects information which is needed for its decision making, and normally the interesting information is around the ROIs defined by the L1 trigger. So, with this ROI approach, only 2-6% of the total data volume will be accessed by the L2 system.

Once the event passes the L2 trigger, the information which were temporarily stored in the Readout Buffers will be collected, the full event is built, and after that, the built event will be accessed by the Event Filter (EF). The EF is designed to finally reduce the event rate to around 200-300 Hz, within 4s. Due to this large available processing time, the standard ATLAS reconstruction and analysis algorithms, which are adapted to the online environment, can be performed for the event selection at the EF stage. If the event fails the EF selection, it will be discarded. The final accepted event will be categorized into different streams, namely, Muons, EGamma, JetTauEtMiss and MinBias, according to the identified features in the event. These events will be permanently stored at CERN Computing Center for offline analysis.

Reference:

- [1] L. Evans and P. Bryant, LHC Machine, Journal of Instrumentation 3 no. 08, (2008) S08001.
- [2] ATLAS Collaboration, The ATLAS Experiment at the CERN Large Hadron Collider, Journal of Instrumentation 3 no. 08, (2008) S08003.
- [3] ATLAS Collaboration, Expected Performance of the ATLAS Experiment - Detector, Trigger and Physics, arXiv:0901.0512 [hep-ex].
- [4] ATLAS Collaboration, “[ATLAS Photos](#)”.
- [5] ATLAS Collaboration, ATLAS detector and physics performance: Technical Design Report, 1, ATLAS-TDR-14; [CERN-LHCC-99-014](#) (1999).

Chapter 4

Object Reconstruction in ATLAS

Figure 4.1 shows the various kinds of particle's signatures when they interact with the ATLAS detector. The object reconstruction is performed based on these signatures.

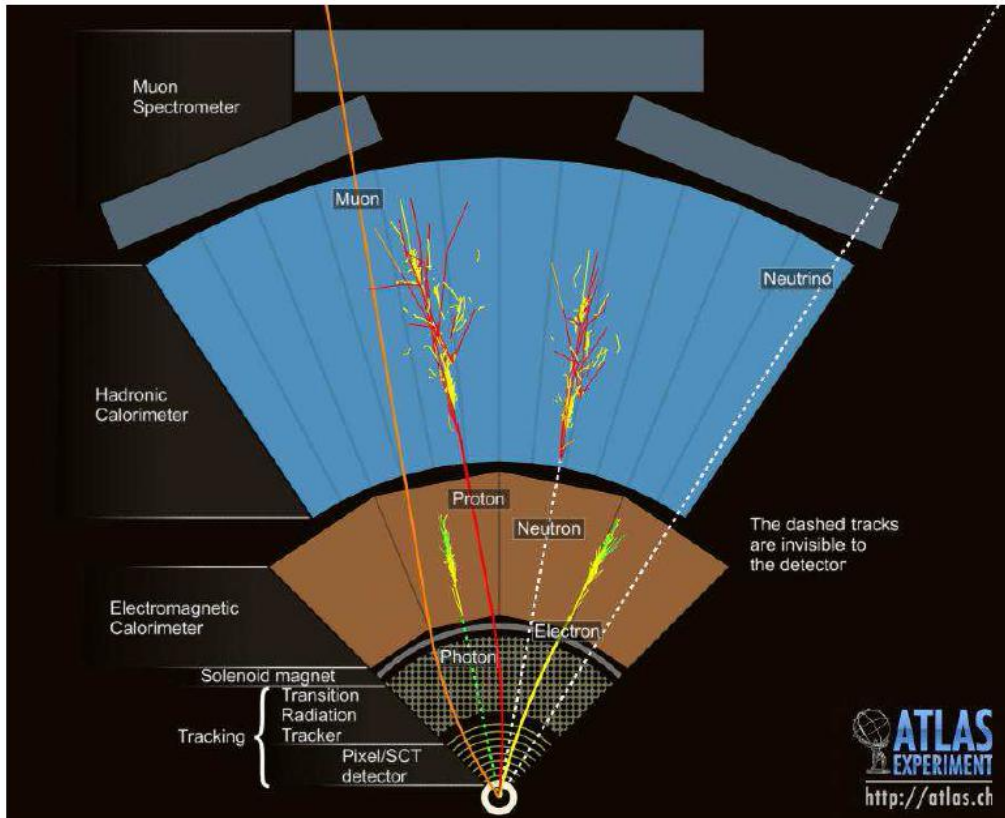


Figure 4.1 Overview of different particle signatures in the ATLAS detector

4.1 Primary Vertex

In the ATLAS experiment, the primary vertex [1] is reconstructed using the information of the reconstructed ID tracks. First of all, the reconstructed tracks are pre-selected with some selection criteria, and a vertex seed is chosen through finding the global maximum of selected tracks' z coordinates distribution. After that, the precise position of the vertex is determined using the adaptive vertex fitting algorithm [2].

When all the primary vertices are found, the one with the largest $\sum p_T^2$ of all the associated tracks is chosen as the hard scattering primary vertex. The rest of the vertices are considered to come from the soft pile-up interactions.

4.2 Electrons

In the ATLAS detector, electrons in the central detector region are triggered by and reconstructed from energy deposits in the electromagnetic (EM) calorimeter that are matched to a track in the inner detector. Electrons are distinguished from other particles using several sets of

identification criteria with different levels of background rejection and signal efficiency. The identification criteria depend on the shapes of the electromagnetic showers in the calorimeter as well as on the track-to-cluster matching quantities. They are based either on independent cuts on these quantities or on a single cut on the output of a likelihood function taking these quantities as input.

4.2.1 Electron reconstruction

Standard ATLAS electron reconstruction [3] consists of three steps: cluster reconstruction in the EM calorimeter, track reconstruction in the ID, and the matching procedure between the two.

The η - ϕ space of the EM calorimeter system is divided into a grid of $N_\eta \times N_\phi = 200 \times 256$ towers of size $\Delta\eta^{\text{tower}} \times \Delta\phi^{\text{tower}} = 0.025 \times 0.025$, corresponding to the granularity of the EM calorimeter middle layer. The energy of the cells is summed to get the tower energy. In order to reconstruct the EM clusters, seed clusters of longitudinal towers with a total cluster transverse energy above 2.5 GeV are searched for by a sliding-window algorithm. The window size is 3×5 towers in the η - ϕ space.

Track reconstruction proceeds in two steps: pattern recognition and track fit. First of all, the seed track requires 3 hits in different silicon detector layers, and more hits are included to form the full track. The standard pattern recognition [4] uses the pion hypothesis for the energy loss at material surfaces. This has been complemented with a modified pattern recognition algorithm based on a Kalman filter-smoother formalism [5] which allows at most 30% energy loss at each material surface to account for possible bremsstrahlung. If using the pion hypothesis does not succeed to extend the track seed to a full track, the new pattern recognition using an electron hypothesis for energy loss is retried. Track candidates are then fitted either with the pion hypothesis or the electron hypothesis (according to the hypothesis used in the pattern recognition) using the ATLAS Global Track Fitter [6]. The fitted tracks need to pass additional requirements on $\Delta\eta$ and $\Delta\phi$, and the number of tracker hits in order to be considered as loosely matched to an EM cluster.

An electron is reconstructed if at least one track is matched to a seed cluster. There can be more than one track associated to a cluster, but only the best matched one is chosen as the primary track which is used to determine the kinematics and charge of the electron and to calculate the electron identification decision. Tracks with at least one hit in the Pixel detector are preferred in order to favor the primary electron track and to avoid random matches between nearby tracks in case of cascades due to bremsstrahlung. If more than one associated track has pixel hits, a dedicated selection criterion is then applied to choose the primary track. All seed clusters together with their matching tracks are treated as electron candidates. Several calibration and correction procedures are performed before the cluster energy are eventually determined.

4.2.2 Electron Identification

Not all objects built by the electron reconstruction algorithm are real prompt electrons. There could be several sources of contamination such as hadronic jets, photon conversions, etc. A likelihood based method [3] is used for the electron identification, in order to reject as much fake or non-prompt backgrounds as possible while keeping a high real electron efficiency. Five working points [7] are supported for LH based electrons, which are VeryLooseLH, LooseLH, LooseAndBLayerLH, MediumLH and TightLH. The electrons in the LAr crack region ($1.37 < |\eta|$

< 1.52) are rejected in order to reduce background from non-prompt and fake leptons.

Apart from that, for channels sensitive to electron charge mis-identification, the electron charge identification selector [8] (ECIDS) is further applied to reduce background from electrons with a wrong charge. ECIDS is a Boosted Decision Tree discriminant built using the following electron input variables: p_T , η , $q \times d_0$, E/p , $\Delta\phi_2^{re-scaled}$ (angle between the cluster position in the second calorimeter layer and the extrapolated track) and the average charge of the tracks weighted by the number of SCT hits. Here d_0 is the transverse impact parameter, which is defined as the shortest distance between a track and the beam line in the transverse plane.

4.2.3 Electron isolation

Electron isolation requirement is applied in order to further reject hadronic jets mis-identified as electrons. Detailed definitions of electron isolation working points can be found in reference [9]. An isolation working point is defined as a fixed cut on both calorimeter and track isolation variables. Details of the electron isolation definitions can be found in reference [3].

4.3 Muons

In the ATLAS experiment, muons reconstruction mainly uses information in the MS and ID, and sometimes requires the information in the calorimeter.

4.3.1 Muon reconstruction

The ID track reconstruction of muons is similar to that of electrons. The MS track reconstruction starts from processing the raw data to obtain drift circles in the MDT and clusters in the CSC, and then track segments are formed from these signal units. Finally, the full track candidates are reconstructed from the track segments.

According to the different information obtained from the detector system, muons can be categorized into four different types. Namely, they are:

- Combined (CB) muons: CB muons are muons of the standard quality. The muon tracks are separately reconstructed in the MS and ID, and the muon candidates are reconstructed through a successful matching between the MS track and the ID track.

- Segment-tagged (ST) muons: Due to low muon transverse momentum or the limited detector acceptance, some muons will only leave trajectory in part of the layers of MDT or CSC, thus only track segments can be reconstructed in the MS. In this case, muon candidates are reconstructed by extrapolating the ID tracks to the MS track segments.

- Calorimeter-tagged (CT) muons: An ID track is reconstructed as a muon if the track is associated with some energy deposit in the calorimeter corresponding to the deposit of a minimum ionizing particle. This type of muon is only used in the region $|\eta| < 0.1$, where the MS is not well instrumented.

- Stand-alone (SA) muons: The muon track is only reconstructed in the MS, while the properties of the muon like the direction and the impact parameter are determined by extrapolating the MS track back to the beam line, considering the muon energy loss in the calorimeter. Stand-alone muons are used in the region $2.5 < |\eta| < 2.7$, where the ID is not covered.

4.3.2 Muon identification

After the muon candidates are reconstructed, the identification is performed in order to

suppress backgrounds from sources like pion and kaon decays. Background muons are expected to have a worse track fit quality and different p_T signature.

Basic requirements for combined muons include: at least 1 pixel hit, at least 5 SCT hits, less than 3 holes and at least 10% of TRT hits included in the final fit in the region $0.1 < |\eta| < 0.9$. In addition, several muon identification quality working points are defined for different analysis goals:

- Medium: This is the standard quality for physics analysis. Only combined and stand-alone muons are selected.
- Loose: This is the quality used to maximize the identification efficiency. All muon types are included in this quality.
- Tight: This is the quality used to maximize the purity of the muons. Only combined muons are considered.
- HighPt: This is the quality used to maximize the muon momentum resolution for muons with $p_T > 100$ GeV.

The corresponding efficiencies for these working points are around 95%, 97%, 90% and 80%, respectively, with a fake muon rate around 1%. Details of the selection criteria for different working points can be found on reference [10].

4.3.3 Muon isolation

Muons originating from the decay of heavy particles, such as W, Z, or Higgs bosons, are often produced isolated from other particles. Unlike muons from semileptonic decays, which are usually embedded in jets, these muons are well separated from other particles in the event. The measurement of the detector activity around a candidate object, referred to as isolation, is therefore a powerful tool for background rejection in many physics' analyses [10]. Since muon isolation is the topic of my ATLAS qualification task, and I've made significant contributions on the muon isolation tool (software) development and muon isolation scale factor (see definition on next page) calculation, more details about it are shown below.

Both track-based and calorimeter-based isolation variables are defined to assess muon isolation.

The track-based isolation variable, p_T^{varcon30} , is defined as the scalar sum of the transverse momenta of the tracks with $p_T > 1$ GeV in a cone of size $\Delta R = \min(10\text{GeV}/p_T^\mu, 0.3)$ around the muon of transverse momentum p_T^μ , excluding the muon track itself. The cone size is chosen to be p_T -dependent to improve the performance for muons produced in the decay of particles with a large transverse momentum.

The calorimeter-based isolation variable, $E_T^{\text{topocone20}}$, is defined as the sum of the transverse energy of topological clusters [11] in a cone of size $\Delta R = 0.2$ around the muon, after subtracting the contribution from the energy deposit of the muon itself and correcting for pile-up effects. Contributions from pile-up and underlying event are estimated using the ambient energy-density technique [12] and are corrected on an event-by-event basis.

The isolation selection criteria are determined using relative isolation variables, which are defined as the ratio of the track- or calorimeter-based isolation variables to the transverse momentum of the muon. The distribution of the relative isolation variables is shown in Figure 4.2, with the data to simulation ratio shown in the bottom panel.

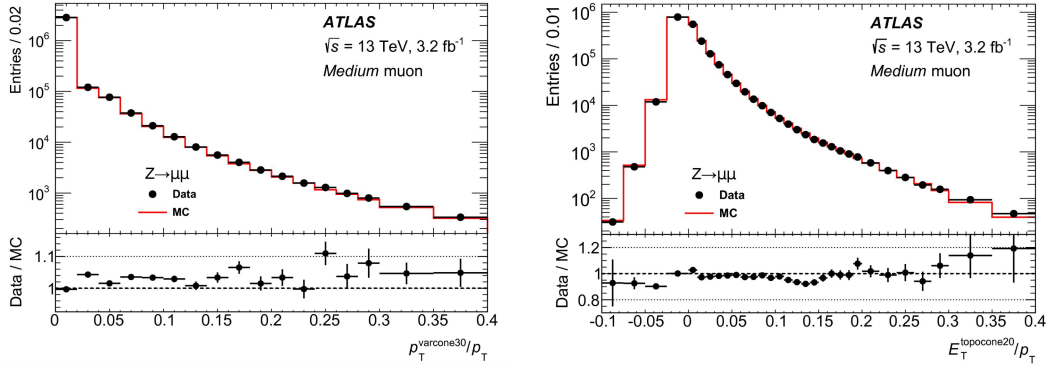


Figure 4.2 Distribution of relative muon isolation variables: track based $p_T^{\text{varcone30}} / p_T$ (left) and calorimeter based $E_T^{\text{topocone20}} / p_T$ (right)

Muons included in the plot are from $Z \rightarrow \mu\mu$ events. They also satisfy the Medium identification criteria and are well separated from the other muon from the Z boson ($\Delta R_{\mu\mu} > 0.3$).

There are in total seven isolation working points defined, each optimised for different physics analyses. Detailed definitions of these working points are listed in Table 4.1.

Isolation WP	Discriminating variable(s)	Definition
<i>LooseTrackOnly</i>	$p_T^{\text{varcone30}}/p_T^\mu$	99% efficiency constant in η and p_T
<i>Loose</i>	$p_T^{\text{varcone30}}/p_T^\mu, E_T^{\text{topocone20}}/p_T^\mu$	99% efficiency constant in η and p_T
<i>Tight</i>	$p_T^{\text{varcone30}}/p_T^\mu, E_T^{\text{topocone20}}/p_T^\mu$	96% efficiency constant in η and p_T
<i>Gradient</i>	$p_T^{\text{varcone30}}/p_T^\mu, E_T^{\text{topocone20}}/p_T^\mu$	≥ 90 (99)% efficiency at 25 (60) GeV
<i>GradientLoose</i>	$p_T^{\text{varcone30}}/p_T^\mu, E_T^{\text{topocone20}}/p_T^\mu$	≥ 95 (99)% efficiency at 25 (60) GeV
<i>FixedCutTightTrackOnly</i>	$p_T^{\text{varcone30}}/p_T^\mu$	$p_T^{\text{varcone30}} / p_T^\mu < 0.06$
<i>FixedCutLoose</i>	$p_T^{\text{varcone30}}/p_T^\mu, E_T^{\text{topocone20}}/p_T^\mu$	$p_T^{\text{varcone30}}/p_T^\mu < 0.06, E_T^{\text{topocone20}}/p_T^\mu < 0.30$

Table 4.1 Definitions of all the muon isolation working points

The efficiencies for the seven isolation working points are measured in both data and $Z \rightarrow \mu\mu$ simulation samples using the tag-and-probe method. The measured isolation efficiencies for Medium muons as a function of the muon p_T for the LooseTrackOnly, Loose, GradientLoose and FixedCutLoose working points are shown in Figure 4.3, with the data-to-Monte Carlo ratios (scale factors) shown in the bottom panel. The systematic uncertainties of the SFs are included in the error bar. Various sources of the systematics are considered, which include: variation of the di-muon invariant mass selection window, the isolation of the tag muon, the minimum quality of the probe muon, the opening angle between the two muons, and the ΔR between the probe muon and the closest jet.

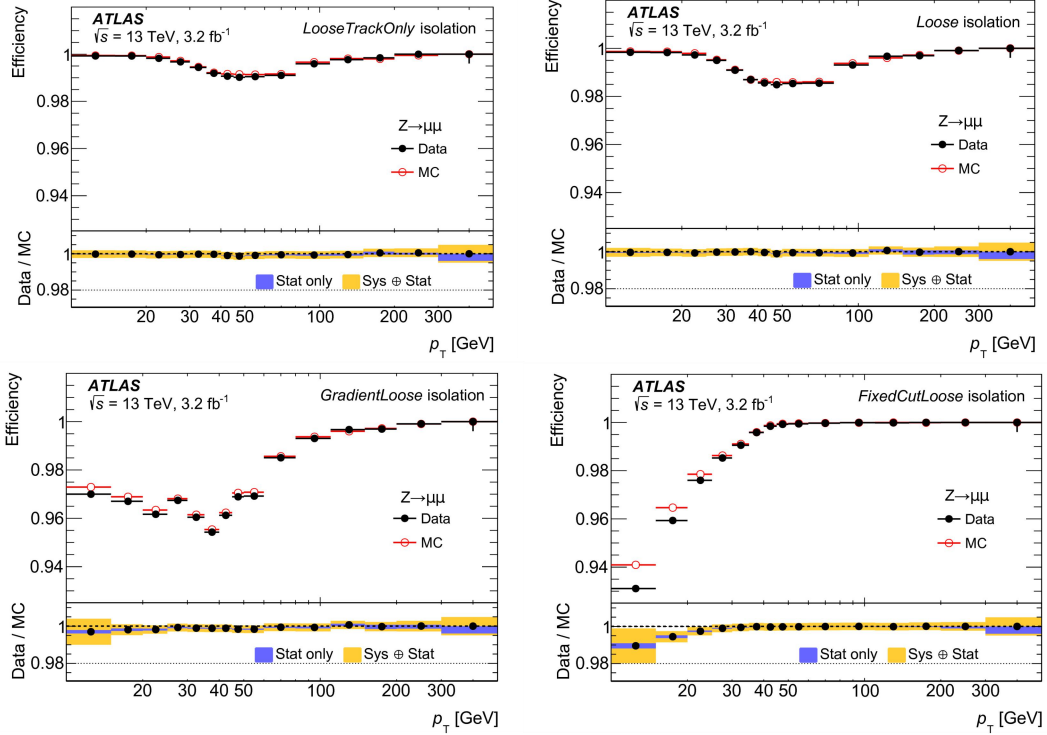


Figure 4.3 Muon isolation efficiencies as a function of muon p_T for different working points

4.4 Jets

Jets are the experimental signatures of quarks and gluons, and they are the most commonly produced objects in a proton-proton collision environment at the LHC. Quarks and gluons are colored objects which participate in the strong interaction. Due to property of colour confinement, single quark cannot exist alone on the time scale of the detector measurement. When quarks and gluons are emitted, hadronization will take place, in which they convert into bound states of colorless hadrons. The majority of the hadrons are charged and neutral pions.

Figure 4.4 provides a schematic overview of jet reconstruction procedure in ATLAS [13]. The standard ATLAS jet reconstruction uses the anti-kt jet algorithm [14] with a distance parameter of $R = 0.4$. This algorithm has been shown to be infrared and collinear safe [15], which means that the physical quantities of the jets are not sensitive to low energy, small angle radiative divergences. Jets can be reconstructed from different inputs, such as truth-level particles, detector tracks, or clusters of energy depositions in calorimeters. Topological clusters (topo-clusters) [16] are the most widely used inputs for jet reconstruction in ATLAS.

Jet reconstruction

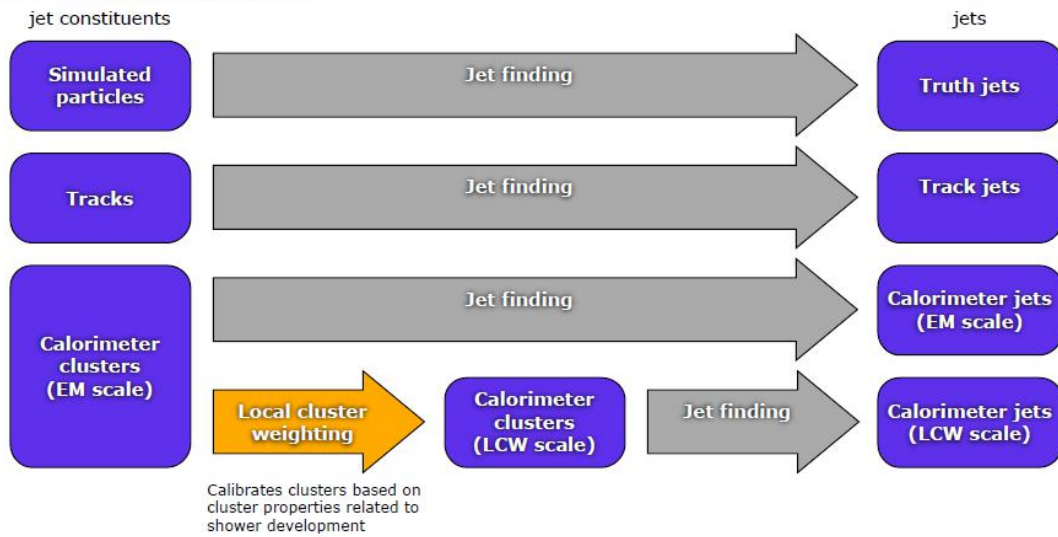


Figure 4.4 Schematic plot of ATLAS jet reconstruction procedure

The topological clustering procedure starts with a seed cell, which has a signal-to-noise ratio above certain threshold (typically 4). The noise usually includes the pile-up noise and the measured detector electronic noise. The ratio threshold is estimated as the absolute value of the energy deposited in the calorimeter cell divided by the RMS of the energy distribution measured respectively from ZeroBias data (random filled bunch crossing triggered proportionally to luminosity) and Monte Carlo simulation. Neighboring cells with high signal-to-noise ratio are iteratively added to the cluster until no neighboring cell meets the requirement.

After the jets are reconstructed, the jet cleaning procedure is performed in order to reduce the fake background. The main sources of the background jets include Beam Induced Background (BIB), cosmic-ray shower and electronic calorimeter noise.

In addition, to reduce the jets coming from pile-up, a specific Jet Vertex Tagger (JVT) is used [17]. It mainly relies on a ratio, where the numerator is the sum of the p_T of all the tracks associated to the jet from the primary vertex, and the denominator is either the sum of the p_T of all the tracks associated to the jet or the reconstructed jet p_T . JVT achieves $\sim 90\%$ efficiency for signal jets and retains $\sim 1\%$ of fake jets.

By default, the energy of reconstructed topo-cluster jets is measured at the EM scale, which is the correct energy scale for EM showers, but not correct for hadronic showers because some of the energy released during the development of a hadronic shower is either invisible or lost in nuclear recoils and dissociation. This problem can be corrected for by applying a hadronic calibration to hadronic objects. This calibration is performed using the local cluster weighting method (LCW) [11], which corrects for non-compensation, energy losses in dead material and out-of-cluster energy depositions, improving the hadronic response of the ATLAS calorimeters.

Finally, a series of jet calibration corrections [18] are performed to further correct the jet energy calculation and improve the jet energy resolution.

4.5 b-tagged jets

Jets originating from b quarks will produce b-hadrons when they hadronize. These jets are unique due to the relatively long lifetime of the produced b-hadrons, which will generate secondary decay vertices in the detector. This unique property is mainly used to tag the b-jets.

There are various b-tagging methods developed in ATLAS, and the most commonly used b-tagging algorithm is the multivariate algorithm (MV2c10) [19]. It uses a boosting decision tree model, which is trained on simulation samples using b-jets as signal and light-jets as background, to compute a tagging weight for each jet. Different b-tagging working points corresponding to a tagging efficiency of 60%, 70%, 77% and 85% are defined, depending on the cut thresholds of the MV2c10 output score [20]. In this analysis, the working point with 77% b-tagging efficiency is used. The corresponding mis-tag rates for c-jets and light jets are 22.2% and 0.7% respectively.

4.6 Missing transverse momentum

Experimentally produced neutrinos don't interact with any detector material, and thus will be reconstructed as missing transverse momentum. Missing transverse momentum (P_T^{miss}) is defined as the negative vector sum of transverse momenta of all the electrons, muons, jets and soft terms from the tracks which are not associated to any reconstructed objects. The missing transverse energy E_T^{miss} is used to represent the magnitude of P_T^{miss} .

Reference:

- [1] ATLAS Collaboration, Performance of primary vertex reconstruction in proton-proton collisions at $\sqrt{s}=7\sim\text{TeV}$ in the ATLAS experiment, [ATLAS-CONF-2010-069](#) (2010).
- [2] W. Waltenberger, R. Fruhwirth, and P. Vanlaer, Adaptive vertex fitting, Journal of Physics G: Nuclear and Particle Physics 34 no. 12, (2007) N343.
- [3] ATLAS Collaboration, Electron efficiency measurements with the ATLAS detector using the 2012 LHC proton-proton collision data, 2014, [ATLAS-CONF-2014-032](#).
- [4] T. Cornelissen et al., Concepts, design and implementation of the ATLAS new tracking (NEWT), [ATL-SOFT-PUB-2007-007](#), 2007.
- [5] R. Fruhwirth, Application of Kalman filtering to track and vertex fitting, Nucl. Instrum. Meth. A262 (1987).
- [6] Improved electron reconstruction in ATLAS using the Gaussian Sum Filter-based model for bremsstrahlung. Technical Report [ATLAS-CONF-2012-047](#), CERN, Geneva, May 2012.
- [7] ATLAS Internal, [Egamma Identification](#), 2018.
- [8] ATLAS Internal, [Electron Charge ID Selection](#), 2018.
- [9] ATLAS Internal, [Lepton Isolation Working points](#), 2018.
- [10] ATLAS Collaboration, Muon reconstruction performance of the ATLAS detector in proton-proton collision data at $\sqrt{s}=13\text{ TeV}$, Eur. Phys. J. C76 (2016) 292, arXiv:1603.05598 [hep-ex].
- [11] ATLAS Collaboration, Jet energy measurement with the ATLAS detector in proton-proton collisions at $\sqrt{s}=7\text{TeV}$, The European Physical Journal C 73 no. 3, (2013) 2304, arXiv:1112.6426 [hep-ex].
- [12] M. Cacciari and G.P. Salam, Pileup subtraction using jet areas, Physics Letters B 659 no. 1-2, (2008) 119-126, arXiv:0707.1378 [hep-ph].
- [13] ATLAS Collaboration, Jet energy measurement and its systematic uncertainty in proton-proton collisions at $\sqrt{s}=7\sim\text{TeV}$ with the ATLAS detector, CERN-PH-EP-2013-222 (2014) 88, arXiv:1406.0076 [hep-ex].
- [14] M. Cacciari, G.P. Salam, and G. Soyez, The anti- k_t jet clustering algorithm, Journal of High Energy Physics 2008 no. 04, (2008) 063-063, arXiv:0802.1189 [hep-ph].
- [15] G.C. Blazey, J.R. Dittmann, S.D. Ellis, et al., Run II Jet Physics: Proceedings of the Run II QCD and Weak Boson Physics Workshop, arXiv:hep-ex/0005012v2 [hep-ex].
- [16] W. Lampl, S. Laplace, D. Lelas, et al., Calorimeter Clustering Algorithms: Description and Performances, ATL-LARG-PUB-2008-002; [ATL-COM-LARG-2008-003](#) (2008).
- [17] ATLAS Collaboration. Performance of pile-up mitigation techniques for jets in pp collisions at $\sqrt{s}=8\text{ TeV}$ using the ATLAS detector. 2015. doi: 10.1140/epjc/s10052-016-4395-z.
- [18] ATLAS Collaboration, Jet energy measurement and its systematic uncertainty in proton-proton collisions at $\sqrt{s}=7\sim\text{TeV}$ with the ATLAS detector, CERN-PH-EP-2013-222 (2014) 88, arXiv:1406.0076 [hep-ex].
- [19] Expected performance of the ATLAS b-tagging algorithms in Run-2. Technical Report [ATL-PHYS-PUB-2015-022](#), CERN, Geneva, Jul 2015.
- [20] ATLAS Collaboration, Expected performance of the ATLAS b-tagging algorithms in Run-2, [ATL-PHYS-PUB-2015-022](#).

Chapter 5

Data Sample and Monte Carlo Simulation

5.1 Data

The data used in this analysis corresponds to the full Run 2 dataset from 2015 to 2018 collected with the ATLAS detector at $\sqrt{s}=13$ TeV. The corresponding integrated luminosity is $139.0 \pm 2.4 \text{ fb}^{-1}$, measured following a methodology similar to that detailed in Ref [1]. The pile-up effect from soft interactions can be expressed by μ , the average number of additional interactions per bunch crossing. μ ranges from 14 in 2015 to 38 in 2017-2018.

5.2 Simulated samples

Monte Carlo (MC) simulation is used for the signal and physics background modeling. Detailed information of simulated samples is listed in Table 5.1. Here PDF means ‘parton distribution function’, PS means ‘parton shower’ and UE means ‘underlying events’.

Process	MC generator	PDF	PS	UE	Xsec (pb)
$t\bar{t}t\bar{t}$	MADGRAPH5	NNPDF	PYTHIA	A14 + NNPDF	0.012
$t\bar{t}$	POWHEG	NNPDF	PYTHIA	A14 + NNPDF	831.76
single top s channel	POWHEGBOX	NNPDF	PYTHIA	A14 + NNPDF	10.32
single top t channel	POWHEGBOX	NNPDF	PYTHIA	A14 + NNPDF	217
tW	POWHEGBOX	NNPDF	PYTHIA	A14 + NNPDF	71.7
$t\bar{t}Z$	MADGRAPH5	NNPDF	PYTHIA	A14 + NNPDF	0.839
$t\bar{t}W$	SHERPA	NNPDF	SHERPA	SHERPA	0.601
$t\bar{t}H$	POWHEGBOX	NNPDF	PYTHIA	A14 + NNPDF	0.508
tWZ	MADGRAPH5	NNPDF	PYTHIA	A14 + NNPDF	/
W+jets	SHERPA	NNPDF	SHERPA	SHERPA	11076
Z+jets	SHERPA	NNPDF	SHERPA	SHERPA	1950
VV	SHERPA	NNPDF	SHERPA	SHERPA	/
VVV	SHERPA	NNPDF	SHERPA	SHERPA	/

Table 5.1 Detailed settings of different Monte Carlo processes

Generally, MC generator is used to compute the production of specific physics processes. In

proton-proton environment, the cross section could be divided into a hard scattering part and a soft scattering part. Due to the unique feature of the strong coupling constant α_s , in the hard scattering part, α_s is small so that perturbative QCD can be used to calculate the cross section, while in the soft scattering part, α_s becomes large so that perturbation theory cannot be applied. The energy scale threshold which separates hard scattering and soft scattering is called the factorization scale μ_F . The inner structure of a proton is provided by the parton distribution function (PDF), which provides the probability of a proton to contain a specific parton with a given fraction of the proton momentum. The initial hard partons will undergo cascade shower process where new gluons or quark-antiquark pairs are emitted. During the parton showering, the interaction scale falls and the strong coupling scale rises, eventually triggering the hadronization process, where partons are bound into colourless hadrons. In the perturbative part, the cross section can be expressed as an expansion of the renormalized coupling constant. The leading order prediction is usually obtained by the Matrix Element (ME) calculation, and corresponds to tree-level Feynman diagrams. Higher order calculation corresponds to more complicated Feynman diagram contributions and usually leads to infinities. Renormalization techniques are introduced to solve the infinity problem. The renormalization scale μ_R is defined as the energy scale for which these divergences can be absorbed in the coupling constant.

The parton-level information provided by the MC generator is interfaced with specific program (usually Pythia) for parton shower. Specific tunes are then used to model the contamination from the underlying events (UE). Finally, the ATLAS detector is simulated using full simulation (Geant4) [2] or fast simulation (ATLFAST-II) [3].

In the analysis presented in this thesis, the $t\bar{t}t\bar{t}$ signal is modelled using the `MADGRAPH5_AMC@NLO v2.6.2` [4] generator which provides matrix elements at next-to-leading order (NLO), with the `NNPDF3.1NLO` [5] PDF set. The renormalization and factorization scales are set in the form of $0.25 \times \sum_i \sqrt{m_i^2 + p_{T,i}^2}$, where i runs over all the particles generated from the matrix element calculation [6]. `PYTHIA8.230` [7] is used for parton shower and hadronization and the A14 tune [8] is used for underlying event modeling. To avoid negative weights in the Boosted Decision Tree training, an additional $t\bar{t}t\bar{t}$ signal sample is produced at LO precision with the same settings. For the estimation of the MC generator uncertainty, an additional $t\bar{t}t\bar{t}$ sample is produced at NLO using `HERWIG7.04` for parton shower and hadronization. The H7UE set of tuned parameters is used for underlying event modelling, and the `MMHT2014LO` PDF set is used for this sample.

The production of $t\bar{t}$ background is modelled with the `POWHEGBOX` [9-12] v2 generator at NLO with the `NNPDF3.0NLO` PDF set and the h_{damp} is set to $1.5 m_{\text{top}}$ [13]. The h_{damp} parameter controls the transverse momentum p_T of the first additional emission beyond the leading-order Feynman diagram in the parton shower, and therefore regulates the high p_T emission against which the $t\bar{t}$ system recoils. `PYTHIA8.230` is used for parton shower and hadronization and A14 is used for underlying event modeling.

The productions of single top related processes are simulated with the `POWHEGBOX` [10-12,14,15,16] v2 generator at NLO with `NNPDF3.0NLO(nf4)` PDF set, interfaced with `PYTHIA8.230` using the A14 tune.

The production of $t\bar{t}Z/\gamma^*$ is modelled using the `MADGRAPH5_AMC@NLO v2.3.3` generator at

NLO with the NNPDF3.0NLO PDF set, and interfaced with PYTHIA8.210 using A14 tune. It is normalized to the inclusive $t\bar{t}l^+l^-$ cross section computed at NLO, including off-shell Z and γ^* contributions with $M_{ll} > 5$ GeV. The production of $t\bar{t}W$ is modelled using the SHERPA v2.2.1 [17] generator with the NNPDF3.0NLO PDF set. The ME was calculated for up to one additional parton at NLO and up to two additional partons at LO using Comix and OpenLoops [18,19], and merged with the SHERPA parton shower [20] using the MEPS@NLO prescription [21-24] and a merging scale of 30 GeV. The production of $t\bar{t}H$ is modelled using the POWHEGBOX generator at NLO with the NNPDF3.0NLO PDF set, interfaced with PYTHIA8.230 using the A14 tune. tWZ production is modelled using the MADGRAPH5_AMC@NLO v2.3.3 generator at NLO with the NNPDF3.0NLO PDF set, interfaced with PYTHIA8.212 using the A14 tune. Other rare top quark processes are modelled using the MADGRAPH5_AMC@NLO generator at LO interfaced with PYTHIA8 using the A14 tune.

V+jets production is simulated with the SHERPA v2.2.1 generator at NLO for up to two additional jets, and at LO up to four additional jets calculated with the Comix and OpenLoops. SHERPA is used for parton shower and parameter tuning. The NNPDF3.0nnlo [5] PDF set is used and the samples are normalized to NNLO prediction.

Diboson(VV) production is simulated with the SHERPA v2.2.1 or v2.2.2 generator at NLO for up to one additional parton and at LO for up to three additional partons. SHERPA is used for parton shower. The NNPDF3.0nnlo PDF set is used.

Triboson(VVV) production is simulated with the SHERPA or v2.2.2 generator at NLO for the inclusive process and at LO for up to three additional partons. SHERPA is used for parton shower. The NNPDF3.0nnlo PDF set is used.

Reference:

- [1] M. Aaboud et al., Luminosity determination in pp collisions at $\sqrt{s} = 8$ TeV using the ATLAS detector at the LHC, *Eur. Phys. J. C* 76 (2016) 653, arXiv: 1608.03953 [hep-ex].
- [2] S. Agostinelli, J. Allison, K. Amako, et al., Geant4-a simulation toolkit, *Nuclear Instruments and Methods in Physics Research Section A: Accelerators, Spectrometers, Detectors and Associated Equipment* 506 no. 3, (2003) 250-303.
- [3] ATLAS Collaboration, The ATLAS Simulation Infrastructure, *The European Physical Journal C* 70 no. 3, (2010) 823-874, arXiv:1005.4568 [physics.ins-det].
- [4] J. Alwall et al., The automated computation of tree-level and next-to-leading order differential cross sections, and their matching to parton shower simulations, *JHEP* 1407 (2014) 079, arXiv: 1405.0301 [hep-ph].
- [5] NNPDF Collaboration, R.D.Ball et al., Parton distributions for the LHC Run II, *JHEP* 04 (2015) 040, arXiv: 1410.8849 [hep-ph].
- [6] R.Frederix, D.Pagani and M. Zaro, Large NLO corrections in $t\bar{t}W$ and $t\bar{t}t\bar{t}$ hadroproduction from supposedly subleading EW contributions, *JHEP* 02 (2018) 031, arXiv: 1711.02116 [hep-ph].
- [7] T. Sjostrand et al., An Introduction to PYTHIA 8.2, *Comput. Phys. Commun.* 191 (2015) 159, arXiv: 1410.3012 [hep-ph].
- [8] ATLAS Collaboration, ATLAS Pythia 8 tunes to 7 TeV data, [ATL-PHYS-PUB-2014-021](#), 2014.
- [9] S. Frixione, P. Nason and G.Ridolfi, A Positive-weight next-to-leading-order Monte Carlo for heavy flavour hadroproduction, *JHEP* 09 (2007) 126, arXiv: 0707.3088 [hep-ph].
- [10] P. Nason, A New method for combining NLO QCD with shower Monte Carlo algorithms, *JHEP* 0411 (2004) 040, arXiv: hep-ph/0409146.
- [11] S. Frixione, P. Nason and C. Oleari, Matching NLO QCD computations with Parton Shower simulations: the POWHEG method, *JHEP* 11 (2007) 070, arXiv: 0709.2092 [hep-ph].
- [12] S. Alioli, P. Nason, C. Oleari and E. Re, A general framework for implementing NLO calculations in shower Monte Carlo programs: the POWHEG BOX, *JHEP* 1006 (2010) 043, arXiv: 1002.2581 [hep-ph].
- [13] ATLAS Collaboration, Studies on top-quark Monte Carlo modelling for Top2016, [ATL-PHYS-PUB-2016-020](#), 2016.
- [14] E. Re, Single-top Wt-channel production matched with parton showers using the POWHEG method, *Eur. Phys. J. C* 71 (2011) 1547, arXiv: 1009.2450 [hep-ph].
- [15] R. Frederix, E. Re and P. Torrielli, Single-top t-channel hadroproduction in the four-flavour scheme with POWHEG and aMC@NLO, *JHEP* 09 (2012) 130, arXiv: 1207.5391 [hep-ph].
- [16] S. Alioli, P. Nason, C. Oleari and E. Re, NLO single-top production matched with shower in POWHEG: s- and t-channel contributions, *JHEP* 09 (2009) 111, [Erratum: *JHEP*02,011(2010)], arXiv: 0907.4076 [hep-ph].
- [17] E. Bothmann et al., Event Generation with Sherpa 2.2, (2019), arXiv: 1905.09127 [hep-ph].
- [18] F. Cascioli, P. Maierhofer and S. Pozzorini, Scattering Amplitudes with Open Loops, *Phys. Rev. Lett.* 108 (2012) 111601, arXiv: 1111.5206 [hep-ph].
- [19] A. Denner, S. Dittmaier and L. Hofer, Collier: a fortran-based Complex One-Loop Library in Extended Regularizations, *Comput. Phys. Commun.* 212 (2017) 220, arXiv: 1604.06792 [hep-ph].

- [20] S. Schumann and F. Krauss, A Parton shower algorithm based on Catani-Seymour dipole factorisation, JHEP 03 (2008) 038, arXiv: 0709.1027 [hep-ph].
- [21] S. Hoeche, F. Krauss, M. Schonherr and F. Siegert, A critical appraisal of NLO+PS matching methods, JHEP 09 (2012) 049, arXiv: 1111.1220 [hep-ph].
- [22] S. Hoeche, F. Krauss, M. Schonherr and F. Siegert, QCD matrix elements + parton showers: The NLO case, JHEP 04 (2013) 027, arXiv: 1207.5030 [hep-ph].
- [23] S. Catani, F. Krauss, R. Kuhn and B. R. Webber, QCD matrix elements + parton showers, JHEP 11 (2001) 063, arXiv: hep-ph/0109231 [hep-ph].
- [24] S. Hoeche, F. Krauss, S. Schumann and F. Siegert, QCD matrix elements and truncated showers, JHEP 05 (2009) 053, arXiv: 0903.1219 [hep-ph].

Chapter 6

Event Selection

Experimentally, the $t\bar{t}$ signal has a signature of several high p_T leptons with missing transverse energy and several high p_T jets of which at least four are b-jets. Since the top quark exclusively decays to a bottom quark and a W boson, the final states of $t\bar{t}$ production depends on the WWWW decay modes. Branching ratios for the different WWWW decay modes are shown in Figure 6.1, where l refers to lepton (electron or muon in the analysis), h refers to hadron, SS refers to same sign lepton pair and OS refers to opposite sign lepton pair.

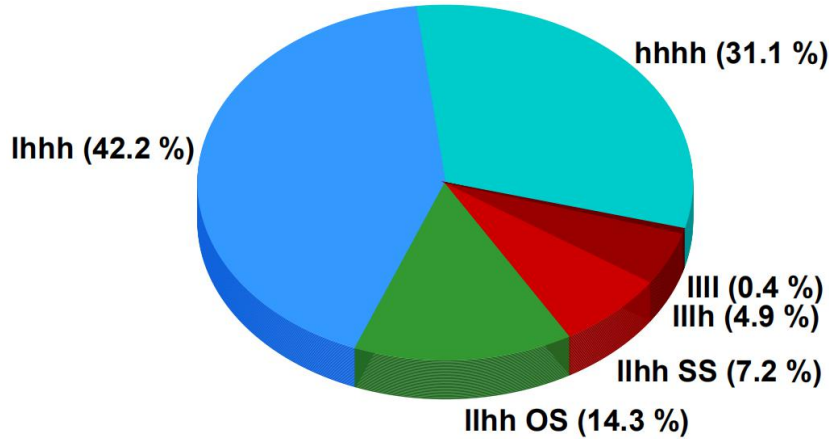


Figure 6.1 Branching ratios of the $t\bar{t}$ decay modes

This thesis focuses on the search for Standard Model $t\bar{t}$ production in the same sign dilepton and multilepton channel (SSML). The total branching ratio of this channel is around 12.5%, which is small compared to other channels, but it also benefits from a lower level of background contamination.

Events considered in this analysis need to satisfy trigger requirement, object overlap removal and kinematic requirement, as well as a loose pre-selection requirement. These are discussed below.

6.1 trigger list

In the SSML analysis, in order to increase the signal acceptance, a logical OR of the single lepton triggers and the dilepton triggers are used. The list of the specific triggers used for each data taking year is shown in Table 6.1 and 6.2.

Year	List of ORed triggers
Single electron triggers	
2015	e24_lhmedium_L1EM20VH, e60_lhmedium, e120_lhloose
2016-2018	e26_lhtight_nod0_ivarloose, 60_lhmedium_nod0, e140_lhloose_nod0
Single muon triggers	
2015	mu20_iloose_L1MU15, mu50
2016-2018	mu26_ivarmedium, mu50

Table 6.1 List of single lepton triggers used in the analysis for each data period

Year	List of ORed triggers
di-electron triggers	
2015	2e12_lhloose_L12EM10VH
2016	2e17_lhvloose_nod0
2017-2018	2e24_lhvloose_nod0
electron-muon triggers	
2015	e17_lhloose_mu14, e7_lhmedium_mu24
2016-2018	e17_lhloose_nod0_mu14, e7_lhmedium_nod0_mu24
di-muon triggers	
2015	2mu10, mu18_mu8noL1
2016-2018	2mu14, mu22_mu8noL1

Table 6.2 List of dilepton triggers used in the analysis for each data period

The triggers are named following certain naming conventions. Take e26_lhtight_nod0_ivarloose for instance: e indicates an electron trigger, 26 indicates the transverse energy threshold, lhtight indicates that it is a likelihood based trigger with tight requirement, nod0 indicates that no transverse impact parameter cuts are required and ivarloose indicates a variable sized cone isolation requirement. L12EM10VH indicates that the L1 trigger is seeded from 2 EM clusters with energy threshold of 10 GeV, and detailed selections include variable thresholds (V) and hadronic isolation (H). The trigger efficiency for the signal is measured in a region similar to the pre-selected signal region (see section 6.3), except that the trigger requirement is removed. The trigger efficiency is measured by calculating the fraction of events passing the trigger requirement in 2015-2016 data samples. The measured trigger efficiencies are 97.51% for the same sign di-lepton channel and 98.95% for the multi-lepton channel respectively.

6.2 Object overlap removal and definition

The requirements on the object identification and the selection criteria are summarized in Table 6.3. Here FCTight indicates the FixedCutTight isolation working point. Detailed information about the working points shown in the table can found in section 4.2-4.5.

After object reconstruction and identification, the same particle going through the detector could possibly be reconstructed as different physics objects. The procedure of overlap removal is used to remove this kind of double counting. In the analysis, the overlap removal procedure corresponds to the following steps:

- An electron candidate track overlapping with another electron is removed.
- A calorimeter muon sharing a track with an electron is removed.

- If ΔR between a jet and a baseline electron is smaller than 0.2, the jet is dropped. In case of multiple jets fulfilling this criteria, only the jet with the smallest ΔR is removed.
- A jet with fewer than three tracks associated to it is removed if it has a muon inner-detector track ghost-matched to it.
- The muon is removed if the distance between a jet and the baseline muon is $\Delta R < 0.4$.
- The muon is removed if the distance between a remaining jet and the baseline muon is $\Delta R < 0.4 + 10 \text{ GeV}/p_{T\mu}$, where $p_{T\mu}$ is the transverse momentum of the muon.

	Electrons		Muons		Jets	b-jets
	loose	tight	loose	tight		
pT [GeV]	> 28		> 28		> 25	> 25
$ \eta $	< 1.37 or 1.52 - 2.47		< 2.5		< 2.5	< 2.5
ID quality	mediumLH	tightLH	medium		cleaning	MV2c10
	ECIDS(ee,e μ)				+ JVT	77%
Isolation	none	FCTight	none	FixedCutTight		
			TrackOnly			
Track vertex :						
$- d_0/\sigma_{d0} $	< 5		< 3			
$- z_0\sin\theta $ [mm]	< 0.5		< 0.5			

Table 6.3 Summary of object identification and definitions

6.3 Event pre-selection and categorization

The pre-selection criteria for the SSML channel [1] requires the event to have at least two same sign leptons. The events are further separated into seven sub-channels depending on the lepton flavor. Namely, they are same sign ee, e μ , $\mu\mu$, eee, ee μ , e $\mu\mu$ and $\mu\mu\mu$ channels. In the eee, ee μ , e $\mu\mu$ and $\mu\mu\mu$ channels, events with the invariant mass of two opposite sign leptons within $81 < M_{ll} < 101 \text{ GeV}$ are vetoed (Z-veto) in order to reduce background from Z decays. A Z-veto is also applied in the same sign ee channel in order to reduce the possible charge mis-identification background. The ECIDS requirement (see section 4.2.2) is applied in the same sign ee and e μ channels in order to further reduce the background originating from the charge mis-identification. For the signal region, the event is required to have at least 6 jets, among which at least 2 are b-jets, and $H_T > 500 \text{ GeV}$. H_T is defined as the scalar sum of the transverse momentum of all the physics objects. Events with lower jet and b-jet multiplicities are defined as control and validation regions, in order to test and validate the quality of the background modelling. A detailed definition of the different control regions is introduced in chapter 7.

Reference:

[1] ATLAS Collaboration, Evidence for $t\bar{t}\bar{t}$ production in the multilepton final state in proton-proton collisions at $\sqrt{s}=13$ TeV with the ATLAS detector, accepted by EPJC, arXiv: 2007.14858 [hep-ex].

Chapter 7

Background Modelling

Background estimation is extremely important in the search for rare signals like $t\bar{t}t\bar{t}$. In the SM $t\bar{t}t\bar{t}$ SSML analysis, the background contributions are divided into three categories.

- Prompt physics background. This type of background refers to the physics processes which can produce exactly the same final states as the $t\bar{t}t\bar{t}$ signal. In this analysis, prompt physics background includes contributions mainly from $t\bar{t}W$, $t\bar{t}Z$, $t\bar{t}H$ and diboson or triboson production together with jets, where events with prompt leptons from the on-shell vector boson (W or Z) decay or Higgs decay can pass our event selections. This type of background is usually estimated using Monte Carlo simulation, since these processes are already well known and can be precisely calculated in theory so that we can trust the results. However, the cross section for $t\bar{t}W$ production is found to be underestimated in simulation, according to the previous analyses, so the normalization factor of this process is left free floating in a combined fit (see Section 7.2).

- Charge mis-identification background. This type of background is mainly due to the mis-identification of the reconstructed track charge of the lepton, or due to the trident process (see Section 7.1), where an electron is reconstructed with the wrong charge. This type of background is estimated using a data-driven method.

- Non-prompt and fake background. This type of background mainly refers to non-prompt leptons from b-jet decay, c-jet decay or gamma conversions, and fakes which are jets mis-identified as leptons. In this analysis, the non-prompt and fake background is estimated using a template fit method, where the shape of the background is determined with Monte Carlo simulation, and the normalization factors of the different types of fake or non-prompt background are determined by fitting MC to data in specific control regions.

Usually, dedicated validation regions are defined in order to validate that our background estimation is reasonable, so that we can use the estimated background in our signal region to search for the signal.

Since the prompt physics backgrounds (except for $t\bar{t}W$) are directly estimated from MC simulation, we will mainly discuss about the estimation of the charge mis-identification background and the non-prompt/fake background.

7.1 Estimation of the charge mis-identification background

The charge mis-identification background estimation is my major contribution to the analysis. I'm responsible for the calculations of the electron-level charge mis-identification rate as well as the event-level charge mis-identification weight, application of the weight to estimated the yields of charge mis-identification background, systematic implementation of the charge mis-identification rate/weight, and all the relevant validations and checks needed during the study.

There are two ways that the charge of a prompt electron can be mis-identified. The first case is when the transverse momenta of the electron is very large so that a straight trajectory is left in the ID. There is a possibility that the charge of the straight track is wrongly reconstructed. The second case is the so-called trident process, where the initial electron radiates a photon through bremsstrahlung, and the radiated photon is further converted into an electron-positron pair. Charge

mis-identification occurs when the electron with the wrong charge is reconstructed by the algorithm. The charge mis-identification is negligible for muons because the probability for a muon to have bremsstrahlung is much smaller than an electron due to the large muon mass. In addition, the large level arm of the muon spectrometer makes the muon track reconstruction more precise. Illustrations of the two ways introducing charge mis-identification are shown in Figure 7.1-7.2.

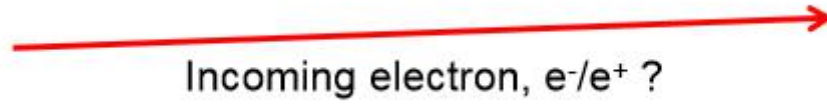


Figure 7.1 Charge mis-identification due to a straight track

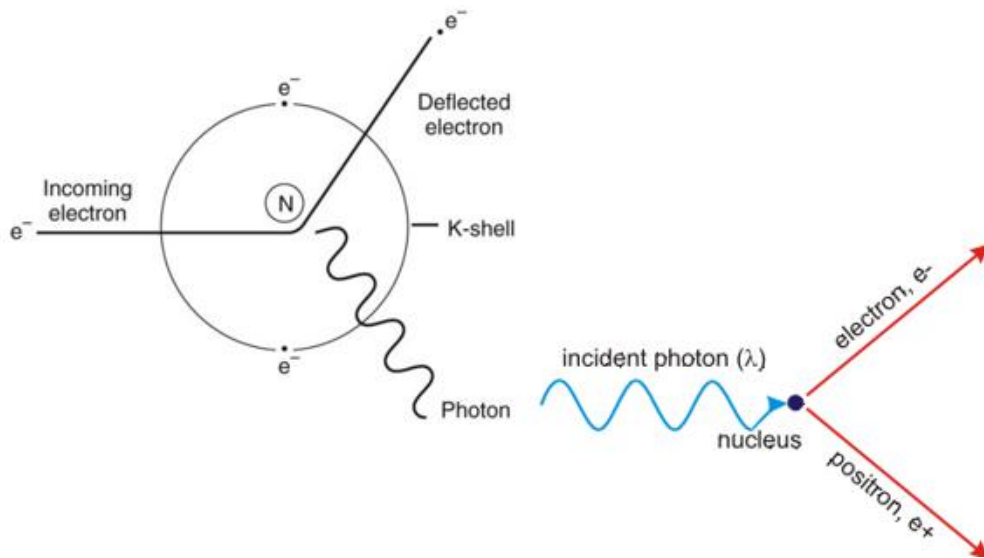


Figure 7.2 Charge mis-identification due to bremsstrahlung and photon conversion

The charge mis-identification background is an important background component in the same sign di-lepton channel. Lepton pairs from $t\bar{t}$ or Z decay are originally opposite signed, and could be faked as the signal when one of the leptons' charge is mis-identified. The charge mis-identification background is estimated using a data-driven method. In the nominal case, the electron charge mis-identification rate, which is the probability for an electron to have its charge mis-identified, is measured with events in the $Z \rightarrow ee$ enriched region in data, as a function of the electron's p_T and the electron's $|\eta|$. The $Z \rightarrow ee$ enriched region is selected by requiring the invariant mass of the di-electron pair to be within a mass window of 10 GeV around the on-shell Z mass. The value of the Z mass is obtained by performing a Gaussian fit on the di-electron invariant mass distribution. Different values of Z mass are used for the same sign region and opposite sign region respectively. Results of the Z mass fit are shown in Figure 7.3.

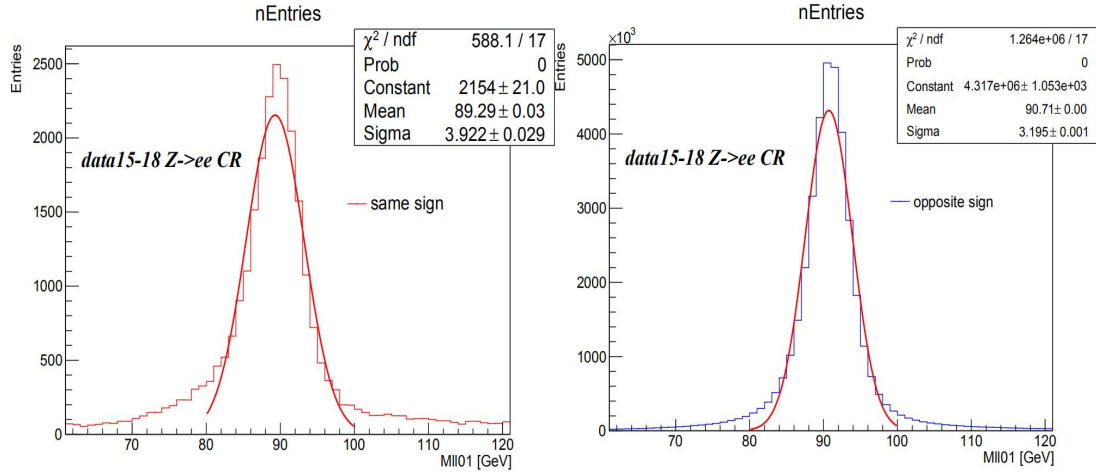


Figure 7.3 Z mass fit on di-electron invariant mass distributions for same sign events (left) and opposite sign events (right) in a data $Z \rightarrow ee$ enriched region

The peak shift in the same sign di-electron invariant mass distribution is expected. It is mainly due to the energy loss of the system in the photon conversion process, where only one of the electrons in the trident topology is selected.

To validate that the $Z \rightarrow ee$ enriched region is properly selected, Data/MC comparisons of some kinematic variables' distributions in the Z peak region are shown in Figures 7.4 and 7.5, for same sign and opposite sign electron pairs respectively.

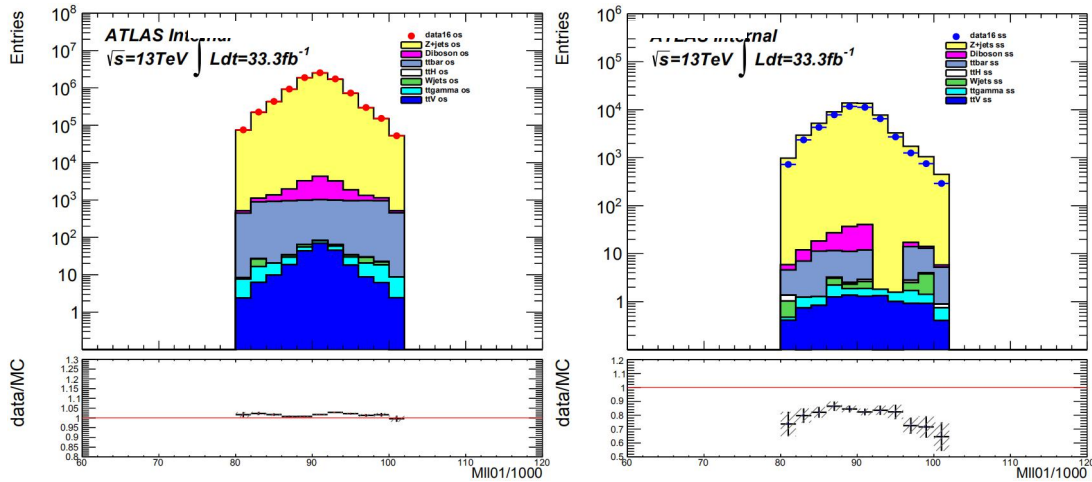


Figure 7.4 Data/MC comparison of the di-electron invariant mass distribution for the opposite sign (left) and same sign (right) electron pairs in the Z peak region using 2016 data

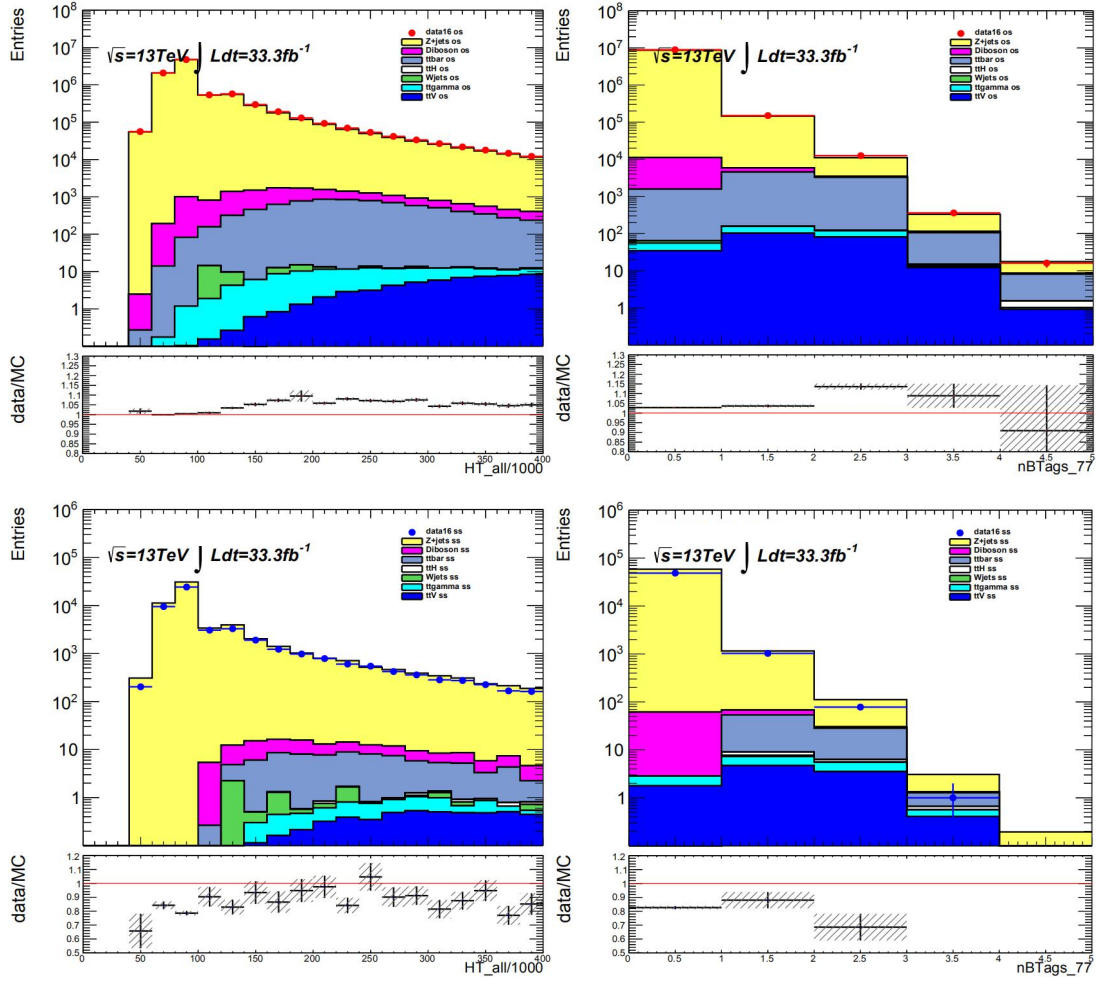


Figure 7.5 Kinematic distributions of opposite sign events (top) and same sign events (bottom) in the Z peak region using 2016 data

It is observed that in the opposite sign region, data and Monte Carlo distributions agree well, while in the same sign region, there are more events in Monte Carlo samples. So the charge mis-identification rates in Z+jets sample is expected to be higher. This is possibly due to the mis-modelling of the calorimeter in which the structure of the calorimeter will impact the photon conversion process.

In the case of the electron charge mis-identification, where the total number of events is large and the charge mis-identification rate is small, a Poisson likelihood can be used to express the probability of observing k charge mis-identified events given the expected value λ :

$$f(k, \lambda) = \frac{\lambda^k e^{-\lambda}}{k!} \quad 7.1$$

The relationship between the expected number of charge mis-identified events and the number of total events is:

$$N_{ss}^{ij} = N^{ij} (\varepsilon_i + \varepsilon_j - 2\varepsilon_i \varepsilon_j) \approx N^{ij} (\varepsilon_i + \varepsilon_j) \quad 7.2$$

where N^{ij} is the number of total observed events, ε_1 and ε_2 are the charge mis-identification rates respectively for the first and the second lepton. The quadratic term takes into account the case of double counting in the linear terms, as well as the case where two leptons are

simultaneously charge mis-identified. It is negligible compared to the linear terms.

If we replace λ with N_{ss}^{ij} , and replace k with N^{ij} , and take the negative logarithm on both sides, we can obtain the final form of the likelihood function:

$$-\ln L(\varepsilon | N_{ss}, N) \approx -\sum_{i,j} \ln[N^{i,j}(\varepsilon_i + \varepsilon_j)]N_{ss}^{i,j} - N^{i,j}(\varepsilon_i + \varepsilon_j) \quad 7.3$$

where the summation runs over all the parameter bins (usually in lepton's p_T and lepton's $|\eta|$). The charge mis-identification rates are then extracted by minimizing the likelihood function.

The measured electron charge mis-identification rates as a function of electron's p_T and electron's $|\eta|$ are shown in Figure 7.6, respectively for data and Z+jets MC events.

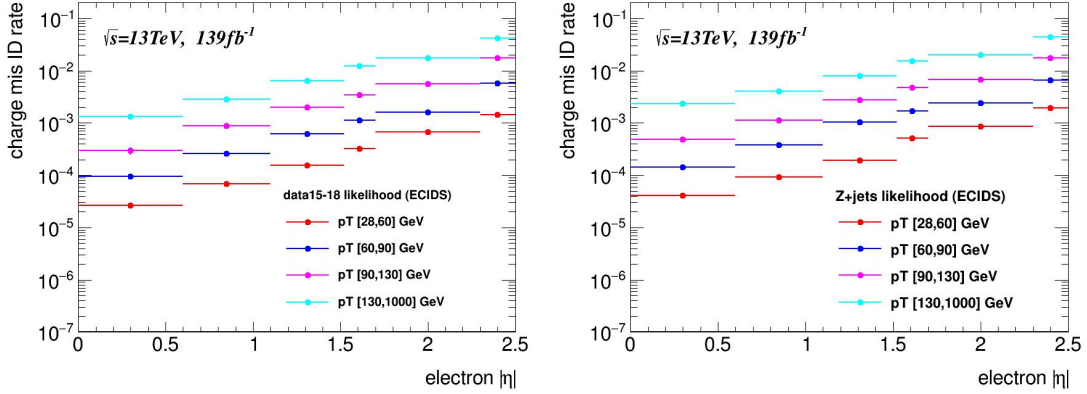


Figure 7.6 Extracted charge mis-identification rates using the likelihood method in data (left) and Z+jets MC (right) samples as a function of electron's p_T and $|\eta|$

It is expected that the charge mis-identification rates increase with respect to the electron's p_T and electron's $|\eta|$. Indeed as the p_T of the electron increases, the track of the electron left in the ID will be straighter, so the probability of the track charge mis-identification also increases. The $|\eta|$ dependency is actually related to the detector structure. Since the detector material in the high $|\eta|$ region is denser than in the low $|\eta|$ region, the probability that a radiated photon interacts with the detector material and is then converted into an electron-positron pair is higher in the high $|\eta|$ region, and therefore the corresponding charge mis-identification rate is higher.

The previous measured rates are electron-level, and we need to convert the rates into an event-level charge mis-identification weight so that we can use the weights to estimate the charge mis-identification background yields. The event-level charge mis-identification weight is written as:

$$w = \frac{\varepsilon_1 + \varepsilon_2 - 2\varepsilon_1\varepsilon_2}{1 - \varepsilon_1 - \varepsilon_2 + 2\varepsilon_1\varepsilon_2} \quad 7.4$$

where ε_1 and ε_2 are the charge mis-identification rates for the first and the second lepton. ε is assumed to be 0 if the lepton is a muon.

In order to validate the charge mis-identification rates are properly measured, closure test is then made by applying back the event-level charge mis-identification weights on the opposite sign events in the Z peak region, and compare the weighted distributions with the original same sign event distributions in the Z peak region. It turns out that the agreement between the two is well within the statistical uncertainty, which proves that the measured charge mis-identification rates are reasonable. The disagreement in the M_{ee} distributions between the same sign and the opposite sign electron pairs is understandable. The peak shift of the same sign events' distribution is due to

the energy loss in the system when the trident process occurs and only one of the electrons is selected.

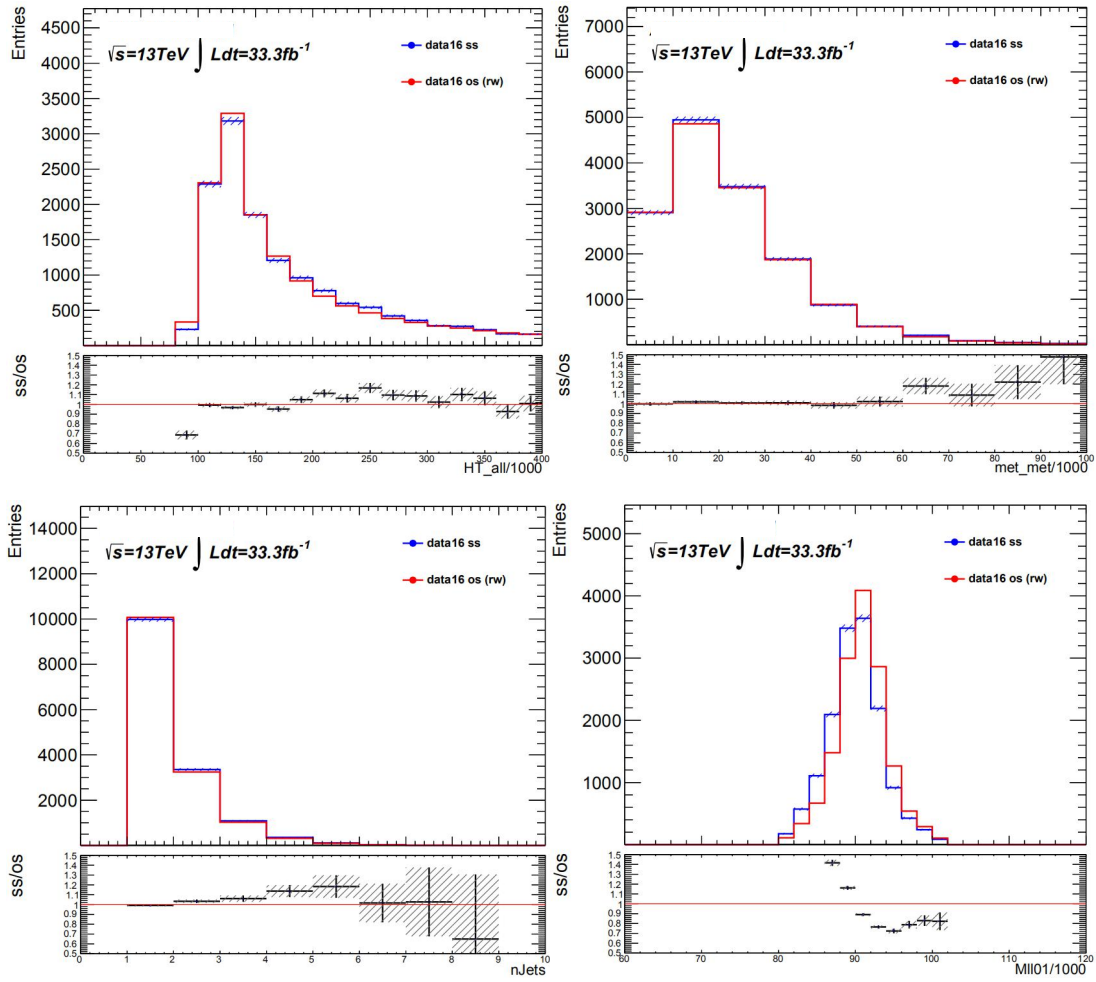


Figure 7.7 Closure test of kinematic distributions in the Z peak region in 2016 data sample with charge mis-identification weights applied on the opposite sign events

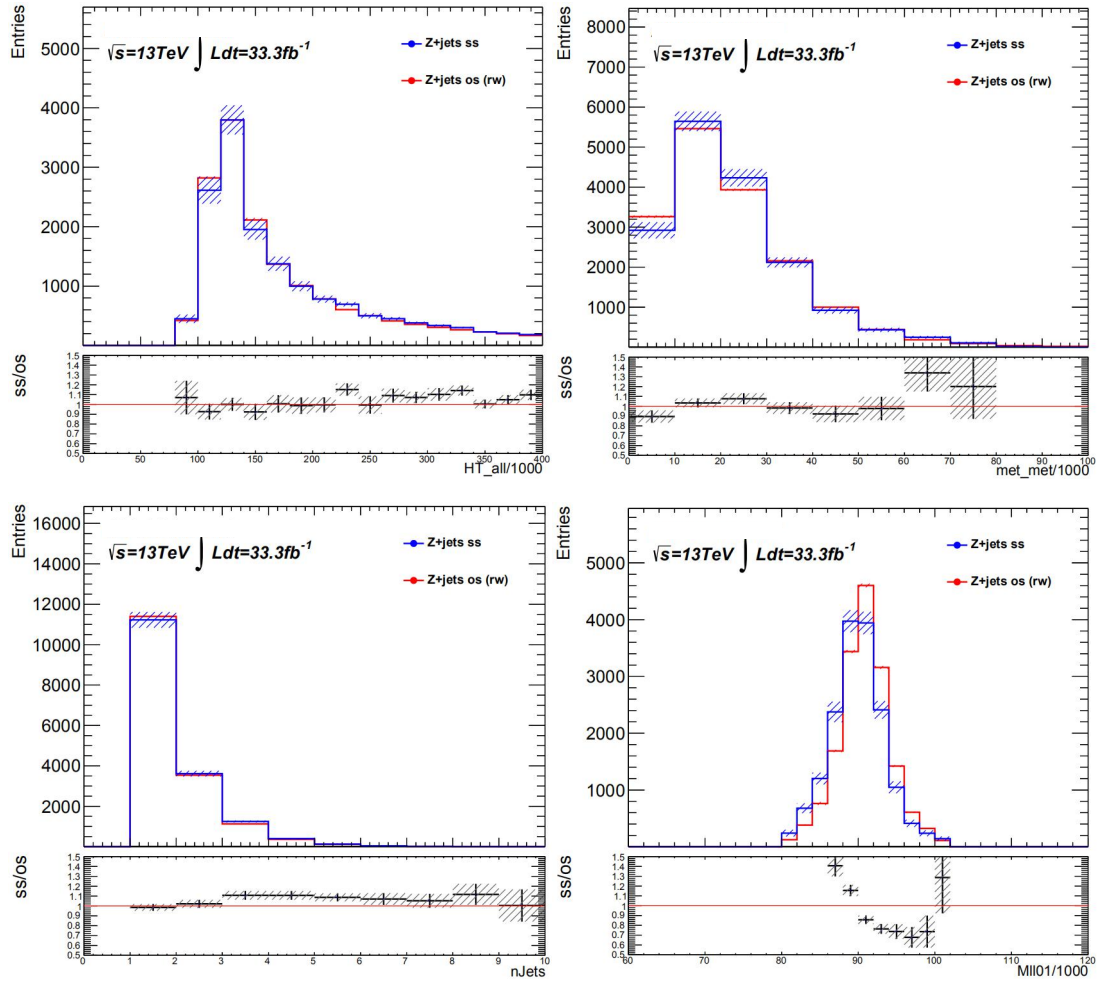


Figure 7.8 Closure test of kinematic distributions in the Z peak region in Z+jets sample with charge mis-identification weights applied on the opposite sign events

In addition to the nominal charge mis-identification rates, there are also requirements for dedicated rates in the $t\bar{t}W$ control region and the $t\bar{t}$ conversion control region. These two regions are defined in the template fit method, which is used for the fake estimation in the analysis. The template fit method will be introduced in section 7.2. In the $t\bar{t}W$ control region, the same electron's p_T and electron's $|\eta|$ binnings are used as in the nominal case. In the conversion control region, the charge mis-identification rates are provided in a three-dimensional format, as a function of electron's p_T , electron's $|\eta|$ and electron's invariant mass at the primary vertex. The extracted rates in these two regions are shown in Figures 7.9 and 7.10.

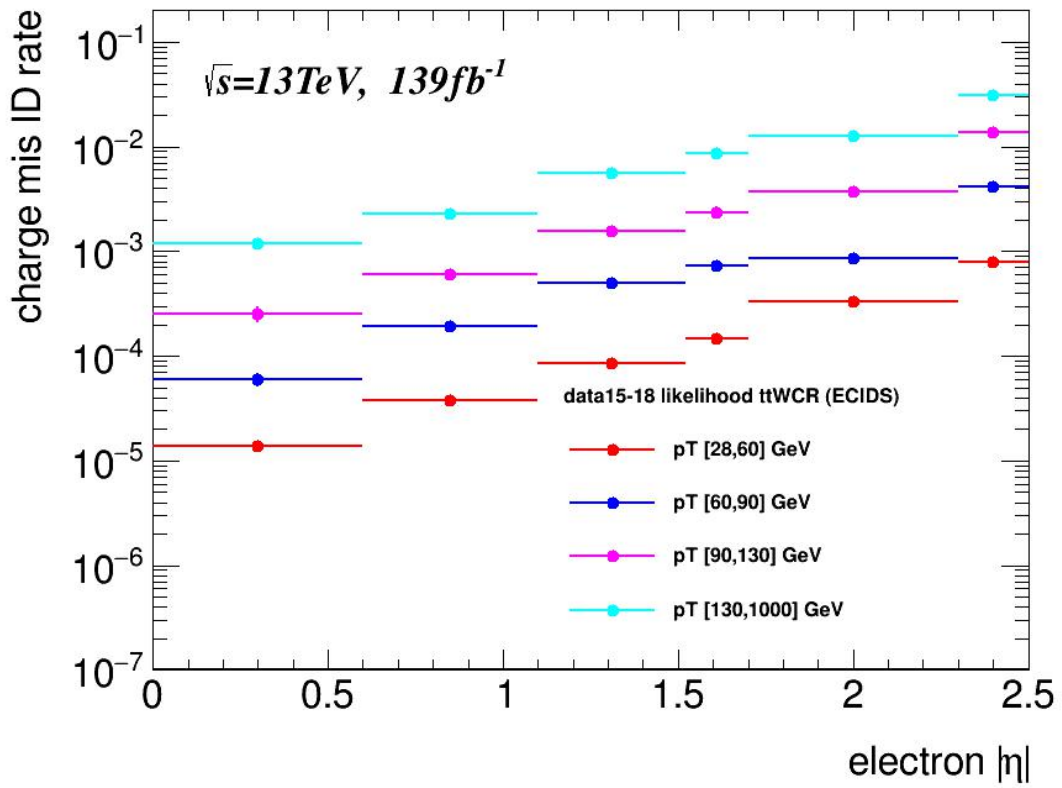


Figure 7.9 Extracted charge mis-identification rates using a likelihood method in data samples as a function of electron's p_T and $|\eta|$ in the $t\bar{t}W$ control region

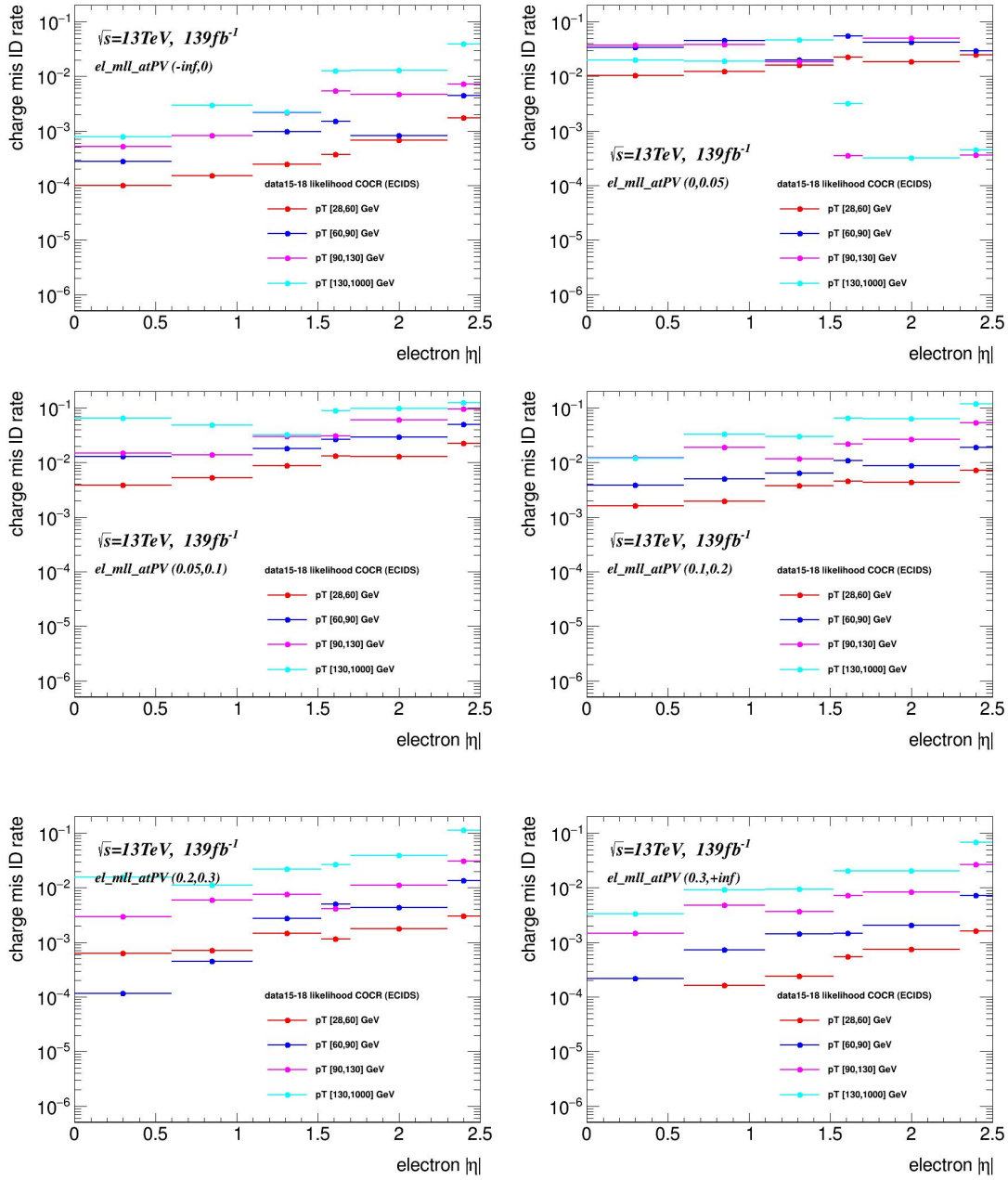


Figure 7.10 Extracted charge mis-identification rates using a likelihood method in data samples as a function of electron's p_T , $|\eta|$ and $M_{ee}@PV$ in the conversion control region (See definition of $M_{ee}@PV$ in Section 7.2.1)

7.2 Estimation of the non-prompt and fake background

7.2.1 The template fit method

Non-prompt and fake backgrounds are estimated using a template fit method. The general idea of the method is that we can define each non-prompt and fake composition with the Monte Carlo truth information so that we can get the shape of the kinematic distributions for each fake component. Then we define several dedicated control regions for these fake components, and the corresponding normalization factors are extracted by fitting the Monte Carlo distributions to the

data in these control regions. A data-driven matrix method is used as a cross-check.

Based on the Monte Carlo truth information, there are four main components for the non-prompt and fake backgrounds, with a normalization factor (NF) assigned to each of them. They are:

- NF HF e: The normalization factor for events with one non-prompt electron from heavy flavor decay
- NF HF mu: The normalization factor for events with one non-prompt muon from heavy flavor decay
- NF CO: The normalization factor for events with one non-prompt electron from photon material conversion
- NF Low mass γ^* : The normalization factor for events with one non-prompt electron from γ^* internal conversion

Apart from that, the non-prompt and fake leptons from light flavor decay correspond to a minor contribution and therefore this contribution is directly taken from Monte Carlo simulation. Since the measured $t\bar{t}W$ cross section in previous analyses [1] is found to be higher than the current prediction, it seems that the current simulation of the $t\bar{t}W$ process is not reliable. So there is a free floating normalization factor for the $t\bar{t}W$ background.

The corresponding control regions (CRs) in which we perform the fits to get the normalization factors are defined below.

The ‘CR Conv.’ is defined as: two same sign electron or electron-muon with a low value of the invariant mass between the electron and a close-by track pointing to the conversion vertex, at least four jets but less than six, at least one b-jet and $200 < H_T < 500$ GeV. The invariant mass of the two leptons at the primary vertex is fitted to constrain both NF CO and NF γ^* .

The ‘CR HF e’ is defined as: three leptons with at least two electrons, exactly one b-jet and $100 < H_T < 250$ GeV, the number of events is used in the maximum likelihood fit.

The ‘CR HF μ ’ is defined as: three leptons with at least two muons, exactly one b-jet and $100 < H_T < 250$ GeV, the number of events is used in the maximum likelihood fit.

The ‘CR $t\bar{t}W$ ’ is defined as: two same sign electron-muon or muons, at least four jets, at least two b-jets, with electron’s $|\eta|$ less than 1.5, orthogonal to the CR Conv region, the sum of the lepton p_T is fitted to constrain NF $t\bar{t}W$.

A summary of the control region definitions used in the template fit is shown in Table 7.1. $M_{ee@CV}$ ($M_{ee@PV}$) is defined as the invariant mass between the track associated to the electron and the closest track at the conversion (primary) vertex.

Region	channel	N_j	N_b	Other requirements	Fitted variable
SR	SS + 3L	≥ 6	≥ 2	$H_T > 500$ GeV	BDT
CR Conv.	SSee SSem	$4 \leq N_j < 6$	≥ 1	$0 < M_{ee@CV} < 0.1$ $200 < H_T < 500$ GeV	$M_{ee@PV}$
CR HF e	eee eem	-	= 1	$100 < H_T < 250$	counting
CR HF μ	emm mmm	-	= 1	$100 < H_T < 250$	counting
CR $t\bar{t}W$	SSem SSmm	≥ 4	≥ 2	$M_{ee@PV} < 0$ or $M_{ee@PV} > 0.1, \eta(e) < 1.5$ for $N_b = 2, H_T < 500$ GeV or $N_j < 6$ for $N_b \geq 3, H_T < 500$ GeV	$\sum_{Pr(l)}$

Table 7.1 Summary of the different control regions and the signal region definitions used in the analysis.

In the blinded stage of the analysis, the template fit is performed in the control regions only, and the extracted normalization factors (NFs) and nuisance parameters (NPs) are injected to the full fit model including the signal region, where the expected sensitivity of the analysis can be obtained. In that setup, pseudo-data built with the injected parameters are used in the signal region.

Pre-fit distributions in the signal region are shown in Figure 7.11.

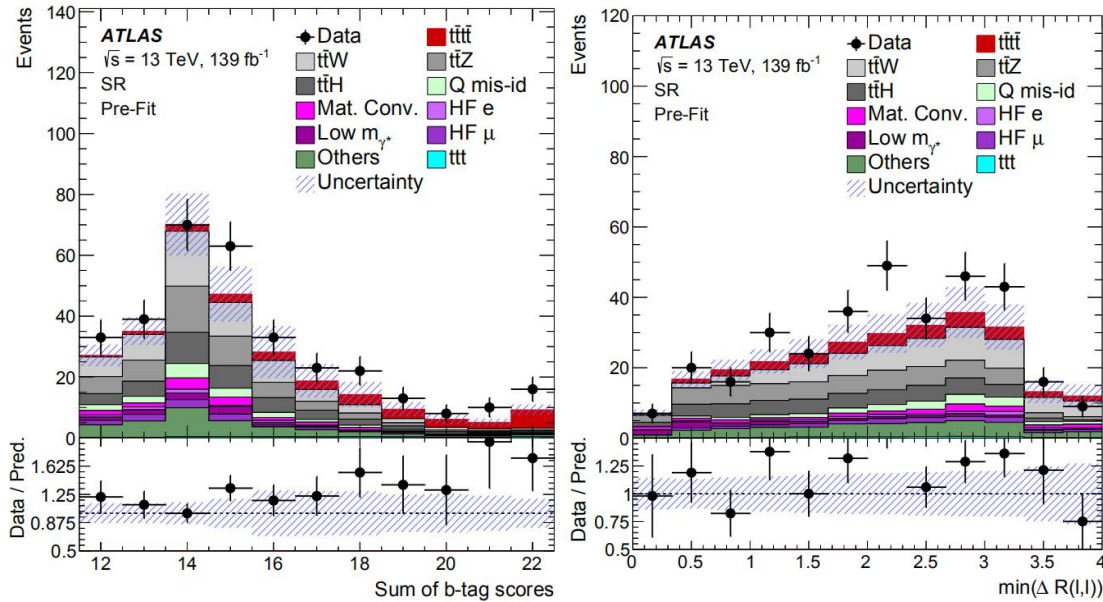


Figure 7.11 Pre-fit distributions in the signal region

A summary of the normalization factors for various backgrounds determined from the fit to all the control regions is shown in Table 7.2:

Parameter	NF $t\bar{t}W$	NF CO	NF Low mass γ^*	NF HF e	NF HF μ
Value	1.6 ± 0.3	1.6 ± 0.5	0.9 ± 0.4	0.8 ± 0.4	1.0 ± 0.4

Table 7.2 Fitted values of the normalization factors from the simultaneous fit in all CRs

7.2.2 The data-driven matrix method

The data-driven matrix method is also used for the fake estimation as a cross check of the template fit method.

The matrix method [2] is based on the definitions of two sets of samples: the Loose sample (L) and the Tight sample (T). The definitions of the Loose leptons and the Tight leptons are the same as the definitions in Section 6.3, except for the additional loose lepton isolation requirement, where FCLoose is used for electrons and FixedCutLoose is used for muons instead of no isolation requirement. This choice is proved to provide a better performance in the closure test. The idea is based on measuring the efficiency of Loose to Tight (L->T) selections for each type of lepton. Once these efficiencies are known, we can estimate the real non-prompt or fake events from the number of observed Loose and Tight events by performing a matrix calculation.

The probabilities $r(f)$ that a prompt (non-prompt/fake) loose lepton passes the tight lepton requirement are measured in data samples, using single lepton events enriched in prompt (non-prompt/fake) leptons. Since the efficiencies need to be measured for leptons with p_T down to 28 GeV and must be measured with a sample that is not biased by the trigger isolation requirement, the following trigger menu is added in order to include events from prescaled support triggers.

- 2015 data: HLT_mu20_L1MU15, HLT_e24_lhmedium_L1EM20VH
- 2016 data: HLT_mu24, HLT_e24_lhmedium_nod0_L1EM18VH
- 2017 data: HLT_mu24, HLT_e26_lhmedium_nod0_L1EM20VH
- 2018 data: HLT_mu24, HLT_e26_lhmedium_nod0_L1EM22VH

Events that fire only one of the prescaled triggers are weighted according to the prescale factors when combining them with events that fire a single-lepton unprescaled trigger.

Both r and f are measured separately for events with 0 b-jets and with at least one b-jets. The measured rates are presented as a function of the lepton's p_T , the lepton's $|\eta|$ and the closest distance between the lepton and a jet $\Delta R_{\min}(l,j)$. Only p_T dependence is considered for the fake estimation.

The selections for the single lepton data control sample are summarized in Table 7.3:

Quantity measured	N_{bjet}	N_{jet}	Additional selection
Electron r	$0b, \geq 1b$	$1j, \geq 2j$	$E_T^{miss} > 150 \text{ GeV}$
Electron f	$0b, \geq 1b$	$1j, \geq 2j$	$m_T(W) < 20 \text{ GeV}$ and $E_T^{miss} + m_T(W) < 60 \text{ GeV}$
Muon r	$0b, \geq 1b$	$1j, \geq 2j$	$m_T(W) > 100 \text{ GeV}$
Muon f	$0b, \geq 1b$	$1j, \geq 2j$	$ d_0 /\sigma_{d0} > 5$

Table 7.3 Summary of the selections for the single lepton data control samples used to measure lepton real efficiency and fake rate

In each control sample, all of the four (N_{bjet} , N_{jet}) combinations are considered. Efficiencies measured with at least 1 b-tagged jet are used for the analysis, while efficiencies measured with 0 b-tagged jets are used for validation regions that impose the same requirement. Different requirements on N_{jet} are used to optimize the event pre-selection criteria. $m_T(W)$ is defined as the transverse mass of the reconstructed W boson (lepton and missing E_T pair).

The measured prompt and fake efficiencies as a function of lepton's p_T for each data period are shown in Figures 7.12 to 7.14:

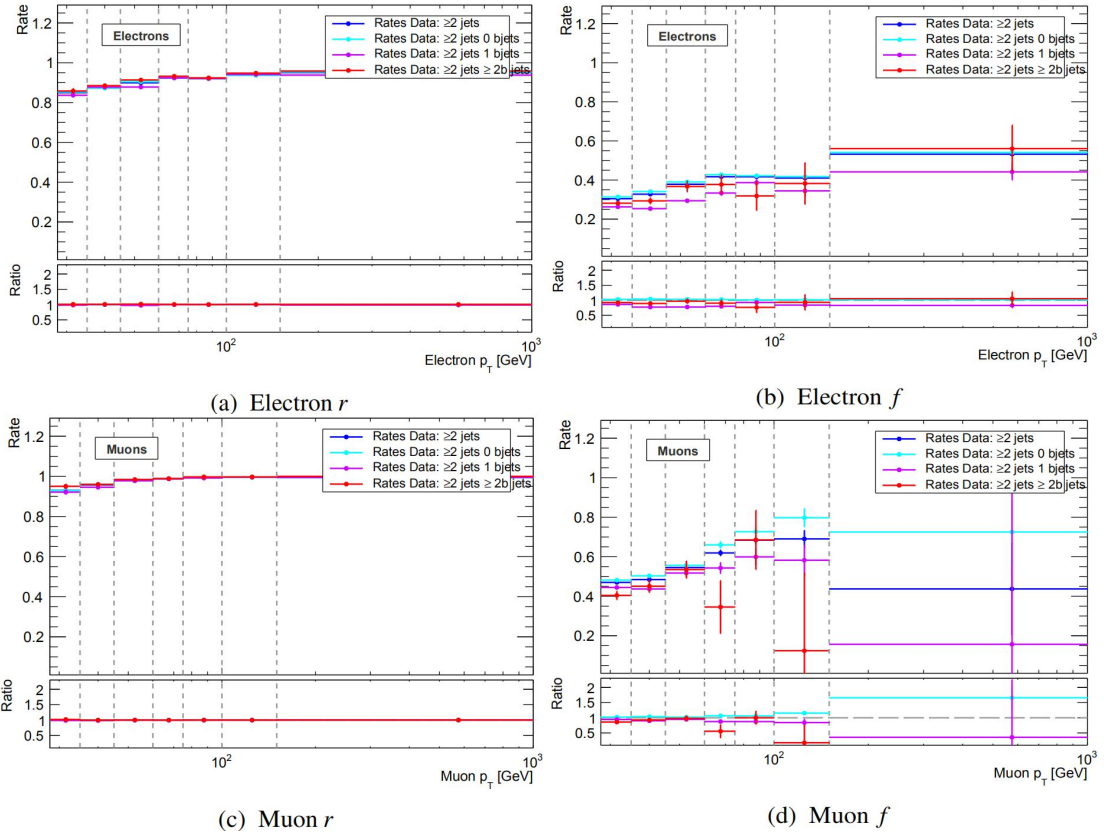


Figure 7.12 Measured prompt and fake efficiencies as a function of lepton's p_T in 2015-2016 data

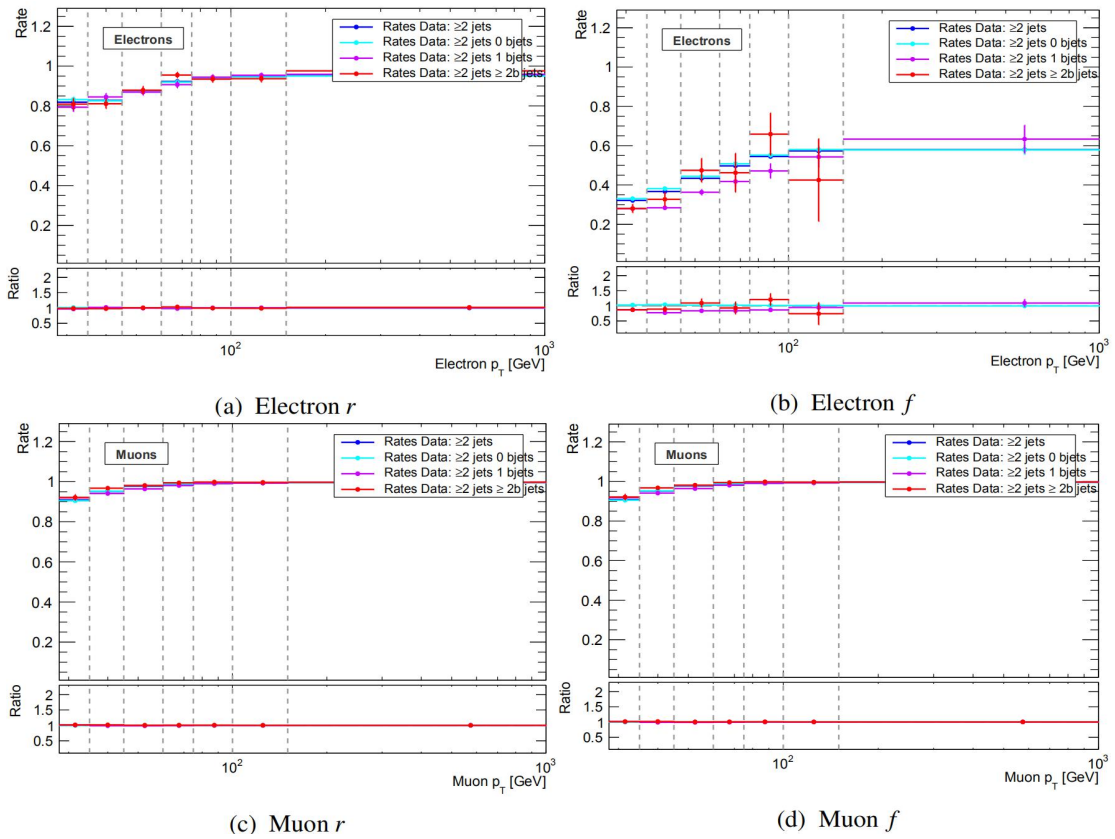


Figure 7.13 Measured prompt and fake efficiencies as a function of lepton's p_T in 2017 data

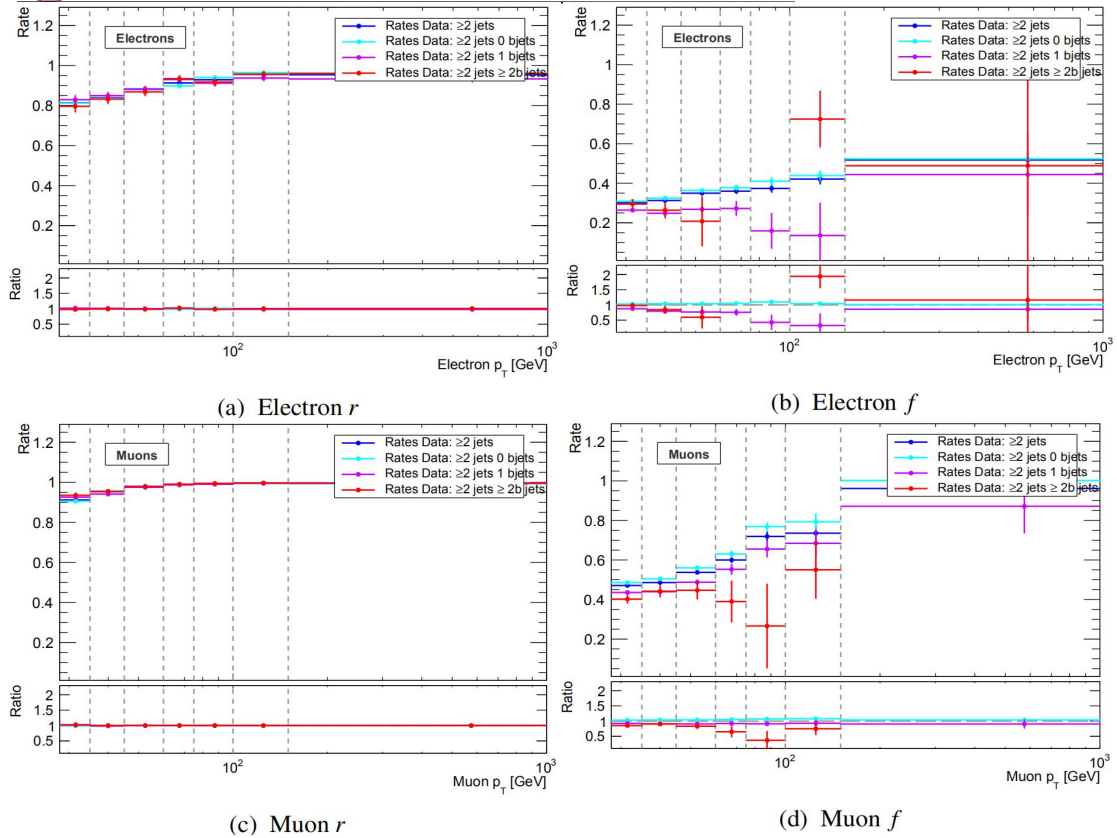


Figure 7.14 Measured prompt and fake efficiencies as a function of lepton's p_T in 2018 data

After the efficiencies are extracted, we can create a matrix equation, and in the dilepton case, it is written as equation 7.5:

$$\begin{pmatrix} N^{tt} \\ N^{t\bar{t}} \\ N^{\bar{t}t} \\ N^{\bar{t}\bar{t}} \end{pmatrix} = \begin{pmatrix} r_1 r_2 & r_1 \bar{f}_2 & f_1 r_2 & f_1 \bar{f}_2 \\ r_1 \bar{r}_2 & r_1 \bar{f}_2 & f_1 \bar{r}_2 & f_1 \bar{f}_2 \\ \bar{r}_1 r_2 & \bar{r}_1 \bar{f}_2 & \bar{f}_1 r_2 & \bar{f}_1 \bar{f}_2 \\ \bar{r}_1 \bar{r}_2 & \bar{r}_1 \bar{f}_2 & \bar{f}_1 \bar{r}_2 & \bar{f}_1 \bar{f}_2 \end{pmatrix} \begin{pmatrix} N_{rr}^{ll} \\ N_{rf}^{ll} \\ N_{fr}^{ll} \\ N_{ff}^{ll} \end{pmatrix} \quad 7.5$$

where N^{tt} is the number of events with both of the leptons being tight, $N^{t\bar{t}}$ is the number of events with the leading lepton being tight and the sub-leading lepton being loose etc. N_{rr}^{ll} is the number of events in the loose sample where both of the leptons are prompt, N_{rf}^{ll} is the number of events in the loose sample where the leading lepton is prompt and the sub-leading lepton is non-prompt/fake etc. \bar{r} and \bar{f} denote $1-r$ and $1-f$.

This matrix equation is solved event by event, where for a given event, N^{tt} , $N^{t\bar{t}}$, $N^{\bar{t}t}$ and $N^{\bar{t}\bar{t}}$ is fixed and N_{rr}^{ll} , N_{rf}^{ll} , N_{fr}^{ll} and N_{ff}^{ll} will be calculated. N_{rr}^{ll} , N_{rf}^{ll} , N_{fr}^{ll} , N_{ff}^{ll} could be interpreted as the probability of the event to have zero non-prompt/fake leptons, one non-prompt/fake lepton and two non-prompt/fake leptons. In the multilepton case, the idea is similar but the matrix is presented in an 8-dimension form.

The closure test with data/MC comparison plots using the data-driven matrix method fakes in the control region is shown in Figure 7.15. The control region is defined as events passing the pre-selection and either $N_{\text{jet}} \leq 5$, $N_{\text{bjet}} \leq 2$ or $H_T < 500$ GeV.

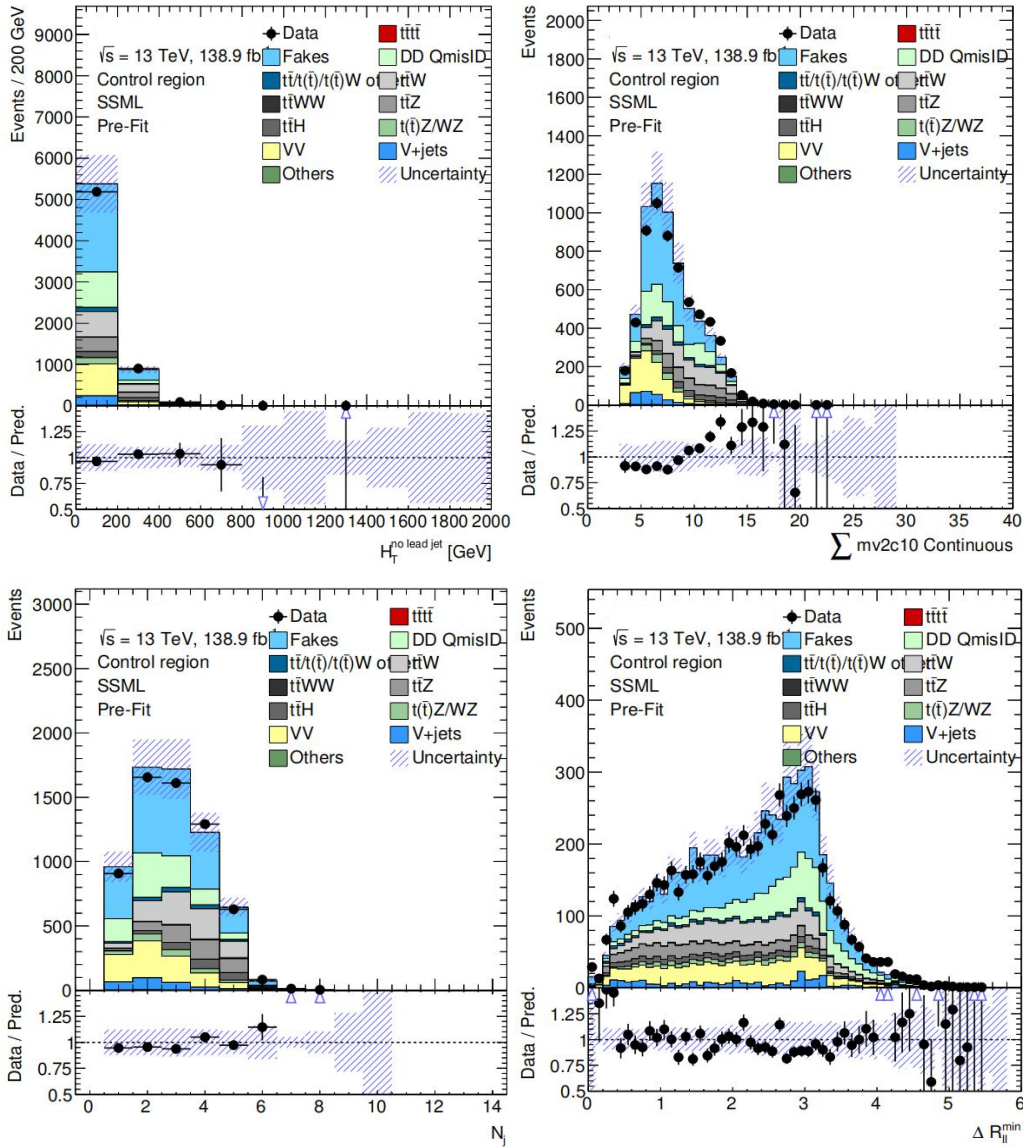


Figure 7.15 Distributions of different kinematic variables in the control region using data-driven Matrix Method fake estimation

The comparison between the event yields with the template fit fakes and the matrix method fakes is shown in Table 7.5.

7.3 Pre-fit and post-fit Data/MC comparison

After the different types of background are properly estimated, further data/MC comparisons in the dedicated control regions are needed in order to test the quality the background modelling.

Figure 7.16 shows the pre-fit and post-fit kinematic distributions in the region with $BDT < 0$ (Detailed information about the BDT study is discuss in Chapter 8). This is used to test the quality of the overall background modelling. ‘post-fit’ here corresponds to the final data fit (described in Chapter 10).

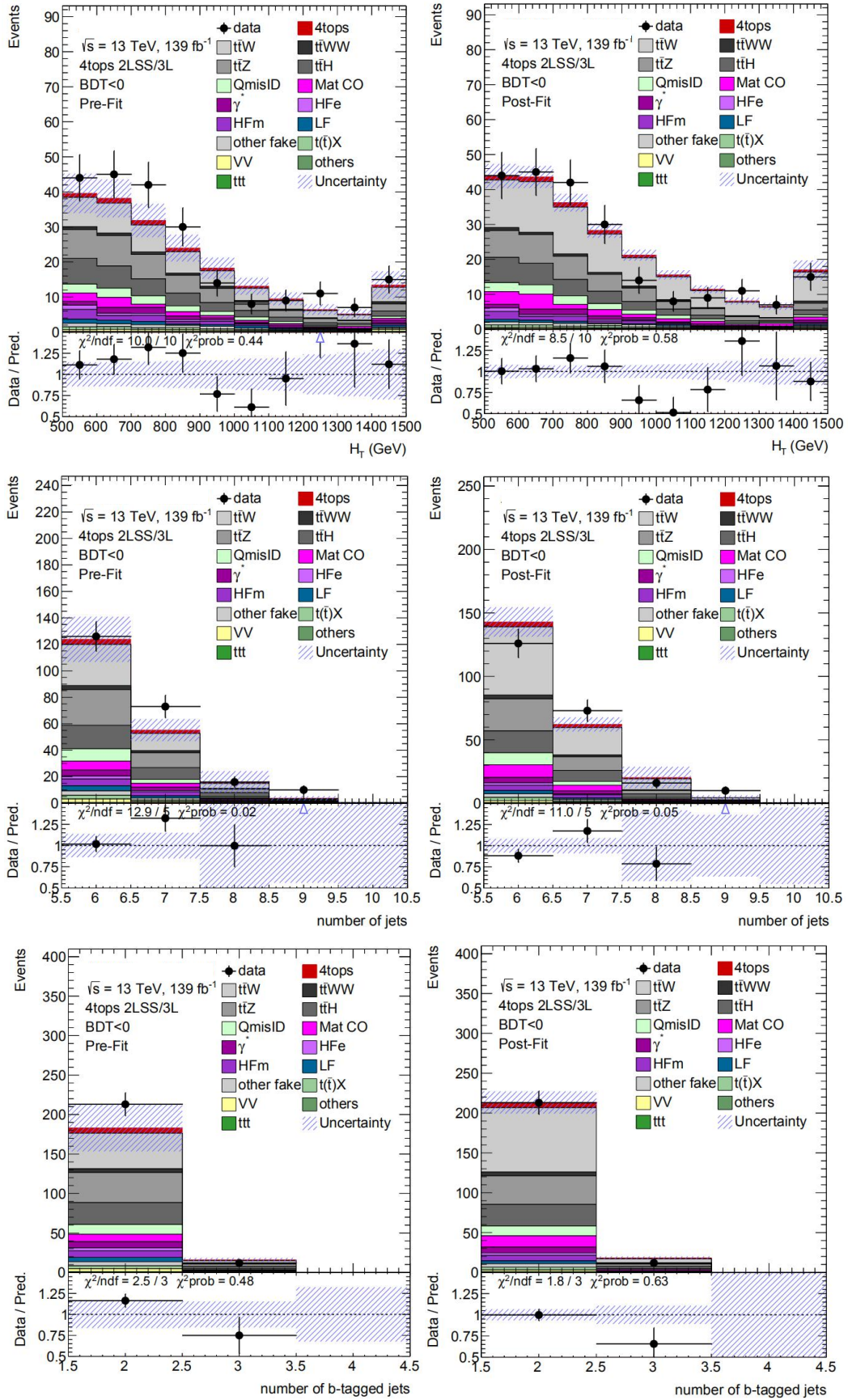


Figure 7.16 Pre-fit (left) and post-fit (right) kinematic distributions in the region with BDT<0

Data/MC comparison in the $t\bar{t}Z$ validation region is shown in Figure 7.17. The $t\bar{t}Z$ validation region is defined as tripleton events failing the Z veto with at least two b-jets, at least six jets and $H_T > 500$ GeV.

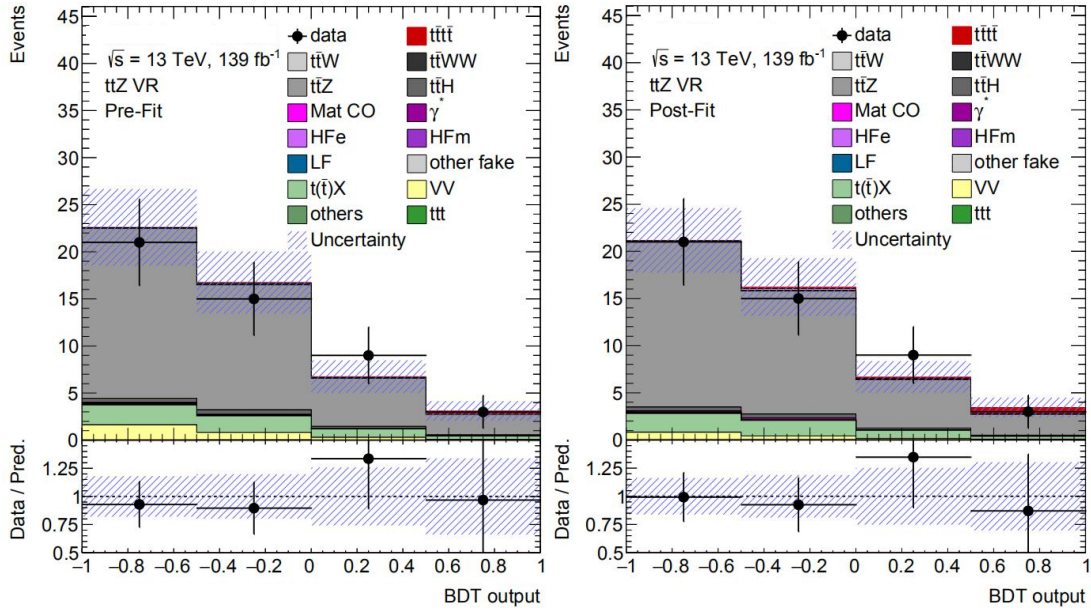


Figure 7.17 Pre-fit and post-fit BDT distribution in the $t\bar{t}Z$ control region

Data/MC comparison in $t\bar{t}W$ validation region is shown in Figures 7.18-7.19. The definition of the $t\bar{t}W$ validation region is based on the fact that $t\bar{t}W$ is the main process which provides charge asymmetry in the $N_{\text{bjets}} \geq 2$ region in the SSML channel. The difference between the number of events with all positively charged leptons and with all negatively charged leptons is a particularly sensitive quantity to the $t\bar{t}W$ process. Therefore this number difference is built bin by bin for the multivariate discriminant (see Chapter 8) with events with $N_{\text{bjets}} \geq 2$ and $N_{\text{jets}} \geq 3$.

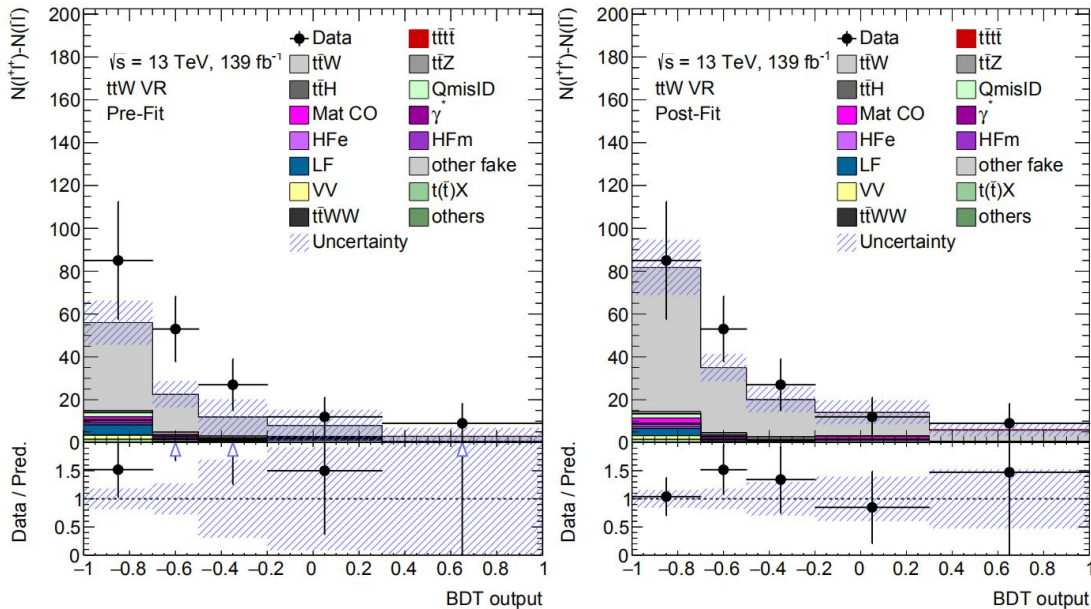


Figure 7.18 Pre-fit and post-fit event yields difference between all positively charged leptons and all negatively charge leptons as a function of the multivariate discriminant

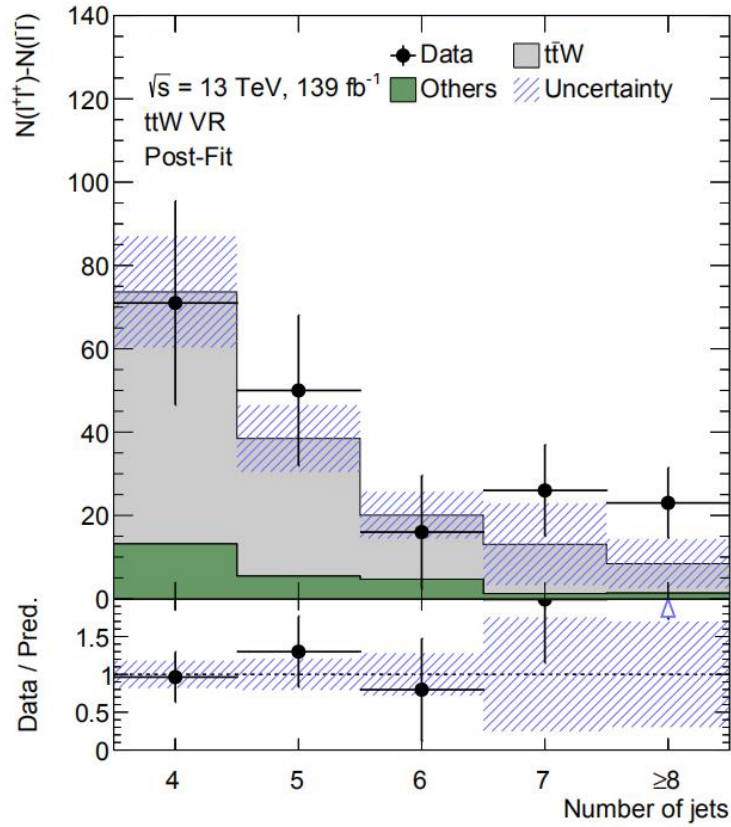


Figure 7.19 Post-fit event yields difference between all positively charged leptons and all negatively charge leptons as a function of the number of jets

The post-fit event yields in the signal region are summarized in Table 10.3. From the yields table, a rough estimation of the significance is $s / \sqrt{b} \approx 3.27$, and the signal efficiency is $60 / (11.97 \text{ fb} * 139.0 \text{ fb}^{-1}) = 3.61 \%$.

A comparison between the post-fit event yields with template fit and matrix method fakes in $\text{BDT} > 0$ region is shown on Table 7.4, ‘post-fit’ here corresponds to the final data fit (described in Chapter 10).

	SR (BDT>0) template fit	SR (BDT>0) matrix method
$t\bar{t}\bar{t}$	24.3 ± 9.4	22.838 ± 0
$t\bar{t}W$	29.9 ± 7.1	22.2 ± 0.54
$t\bar{t}WW$	3.2 ± 1.6	2.9 ± 0.2
$t\bar{t}Z$	13.2 ± 2.8	14.0 ± 0.4
$t\bar{t}H$	12.3 ± 2.9	10.9 ± 0.1
QmisID	3.6 ± 0.5	3.5 ± 0.2
Mat CO	5.9 ± 2.2	/
γ^*	1.3 ± 0.7	/
HFe	2.0 ± 1.2	/
HFm	2.8 ± 1.4	/
LF	0.7 ± 0.8	/
Other fake	2.0 ± 0.8	/
All fakes	14.7 ± 3.2	14.4 ± 6.8
$t(\bar{t})X$	1.3 ± 0.4	1.6 ± 0.2
VV	0.3 ± 0.2	0.9 ± 0.1
V+jets	0.03 ± 0.01	0.03 ± 0.02
others	2.2 ± 1.1	2.0 ± 0.0
Total	105.2 ± 8.7	95.3 ± 9.64

Table 7.4 Comparison between the signal and background yields with template fit fakes and matrix method fakes (post-fit)

The estimated fake yields between the two methods are compatible. The differences in the yields of other processes arise from the additional requirements in the matrix method that events passing exclusively triggers with isolation are rejected, as well as the FCLoose isolation requirement on top of the existing muon isolation criteria. The uncertainties shown in the table are discussed in detail in Chapter 9.

Reference:

- [1] ATLAS Collaboration, Measurement of the $t\bar{t}W$ and $t\bar{t}Z$ production cross sections in pp collisions at 8 TeV with the ATLAS detector, JHEP 11 (2015) 172, arXiv: 1509.05276 [hep-ex].
- [2] ATLAS Collaboration, Estimation of non-prompt and fake lepton backgrounds in final states with top quarks produced in proton-proton collisions at $\sqrt{s}=8\text{TeV}$ with the ATLAS detector, ATLAS-CONF-2014-058.

Chapter 8

Multivariate Analysis

In order to enhance the sensitivity of the $t\bar{t}t\bar{t}$ search, a multivariate analysis is performed. A commonly used Boosting Decision Tree (BDT) method is applied in this analysis.

For this part, my contribution to the analysis is the early stage hyper-parameter optimization of the BDT, using the fitted significance as the metric.

The BDT is meant to discriminate the $t\bar{t}t\bar{t}$ signal against all of the backgrounds. It is performed in the signal region of the SSML channel (see section 6.3). A train-test-validation procedure is used.

All the events are divided into the training samples, testing samples and validation samples. Training samples are used to train and build the BDT model, and the trained model is then applied on the testing samples to see the prediction accuracy of the model. This procedure can be repeated many times in order to do the hyper-parameter optimization. A hyper-parameter is a parameter of the BDT, which are optimized manually. The final BDT with all the hyper-parameters optimized is applied on validation samples to eventually assess separation power of the model on unseen data. All of the background samples used are produced at NLO accuracy. A LO signal sample is 100% used for the training as we want to avoid the issue of negative weights appeared when we train the NLO signal sample. 80% of the NLO signal sample is used for testing, with the remaining 20% used for validation. For all the background samples, 20% of the events are used for validation. The remaining 80% of the events are divided into two equivalent sub-samples, 40% each, based on the event number being odd or even. The BDT trained with odd events are tested on even events, and the BDT trained with even events are tested on odd events. The illustration of the whole procedure is shown in Figure 8.1.

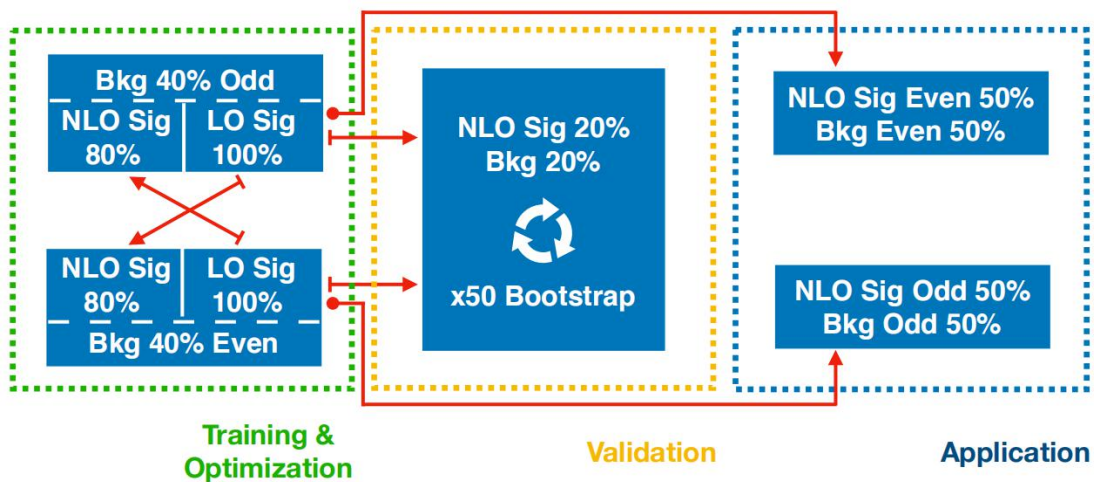


Figure 8.1 Illustration of the train-test-validation procedure for the BDT analysis

There are several metrics to evaluate the performance of a trained BDT. In this analysis the Receiver Operating Characteristic (ROC) curve is used as metric. The ROC curve is created by plotting the true positive rate against the false positive rate at various BDT threshold values. The true positive rate is the fraction of signal events which are predicted to be signal by the BDT. The

false positive rate is the fraction of the background events which are predicted to be signal by the BDT. Usually the Area Under ROC Curve (AUC) is the final value used to evaluate the performance of the model. The AUC actually represents the overall probability of the model to make correct predictions among all the events.

The hyper-parameter optimization is performed by scanning over the entire hyper-parameter phase space and by selecting the point which provides the best performance. There are 6 hyper-parameters to be optimized, and each hyper-parameter has 5 tested values, except for nTrees (number of trees) which has 6 test values. So the hyper-parameter phase space has $6 \times 5^5 = 18750$ points to evaluate. The performance is evaluated by the AUC of each BDT. For the odd and even splitting case, we take the average AUC of the two models as the performance metric. An initial set of 21 input variables is used in this step.

A typical ROC curve of a trained model is shown in Figure 8.2.

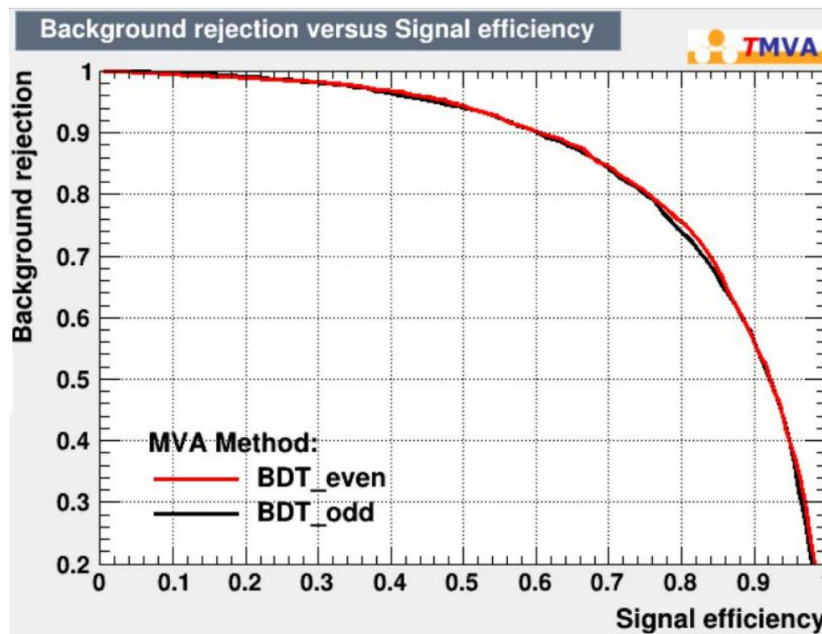


Figure 8.2 Example of a typical ROC curve for the trained BDT model

The AUC values of the different trained BDTs range from 0.80 to 0.854. The final optimized hyper-parameters are listed in Table 8.1.

Parameter	Optimized value	Definition
Max.D.	6	Number of maximum split BDT nodes allowed
nCuts	15	Granularity of variable distributions used
nMin%	3	Minimum number of allowed fraction of events in a leaf
Shrinkage	0.01	Learning rate of the optimization procedure
Bagging	0.7	Fraction of the random sampling size
nTrees	800	Number of trees grown during the iteration

Table 8.1 Optimized BDT hyper-parameters

The AUC corresponding to the optimized model is 0.854.

After the optimized hyper-parameters are fixed, an iterative removal (IR) method [1] is used to optimize the input variables list. In the IR method, a variable is removed and the BDT is trained again. The loss on the final separation power due to removal of this variable is then probed. If it is

below a certain threshold or negligible, the variable is dropped and the process is repeated. After the IR procedure, a list of 12 variables are selected as the final input. Detailed information of these variables is listed in Table 8.2:

Variable	Category	Description
$\sum W_{MV2c10}$	B-tagging	Sum of MV2c10 pseudo-continuous b-tagging score over all jets
p_T^{l0}	Lepton	Transverse momentum of the leading lepton
E_T^{miss}	Energy	Missing transverse energy
$\Delta R(l,l)_{min}$	Distance	Minimum distance between any lepton pair
p_T^{jet5}	Jet	Transverse momentum of the 6 th leading jet
$\Delta R(l,b)_{max}$	Distance	Maximum distance between leptons and b-tagged jets
$H_T^{no\ lead\ jet}$	Energy	Scalar sum of all lepton and jet p_T except the leading jet
$\sum \Delta R(l,l)_{min}$	Distance	Sum of the distance between the first two leptons in SS and the first three leptons in 3L
p_T^{jet0}	Jet	Transverse momentum of leading jet
$\Delta R(j,b)_{min}$	Distance	Minimum distance between jets and b-tagged jets
p_T^{b-jet0}	Jet	Transverse momentum of the leading b-tagged jet
p_T^{jet1}	Jet	Transverse momentum of the sub-leading jet

Table 8.2 Information of the final BDT input variables list

Among the above variables, $\sum W_{MV2c10}$ provides the highest separation power since normally four b-jets are produced in the signal events. The pseudo-continuous b-tagging score is an integer variable assigned to a jet, with a value from 1 to 5, each corresponding to a specific region in the continuous MV2c10 distribution. Value 5 indicates that the jet is like a b-jet most. $\Delta R(l,l)_{min}$ is the second important variable in term of the separation power.

The post-fit Data/MC comparison of the input BDT variables in the region with $BDT < 0$ is shown in Figures 8.3 to 8.4. ‘post-fit’ here corresponds to the final data fit described in Chapter 10. The Data/MC agreement of the input BDT variables is checked to be acceptable.

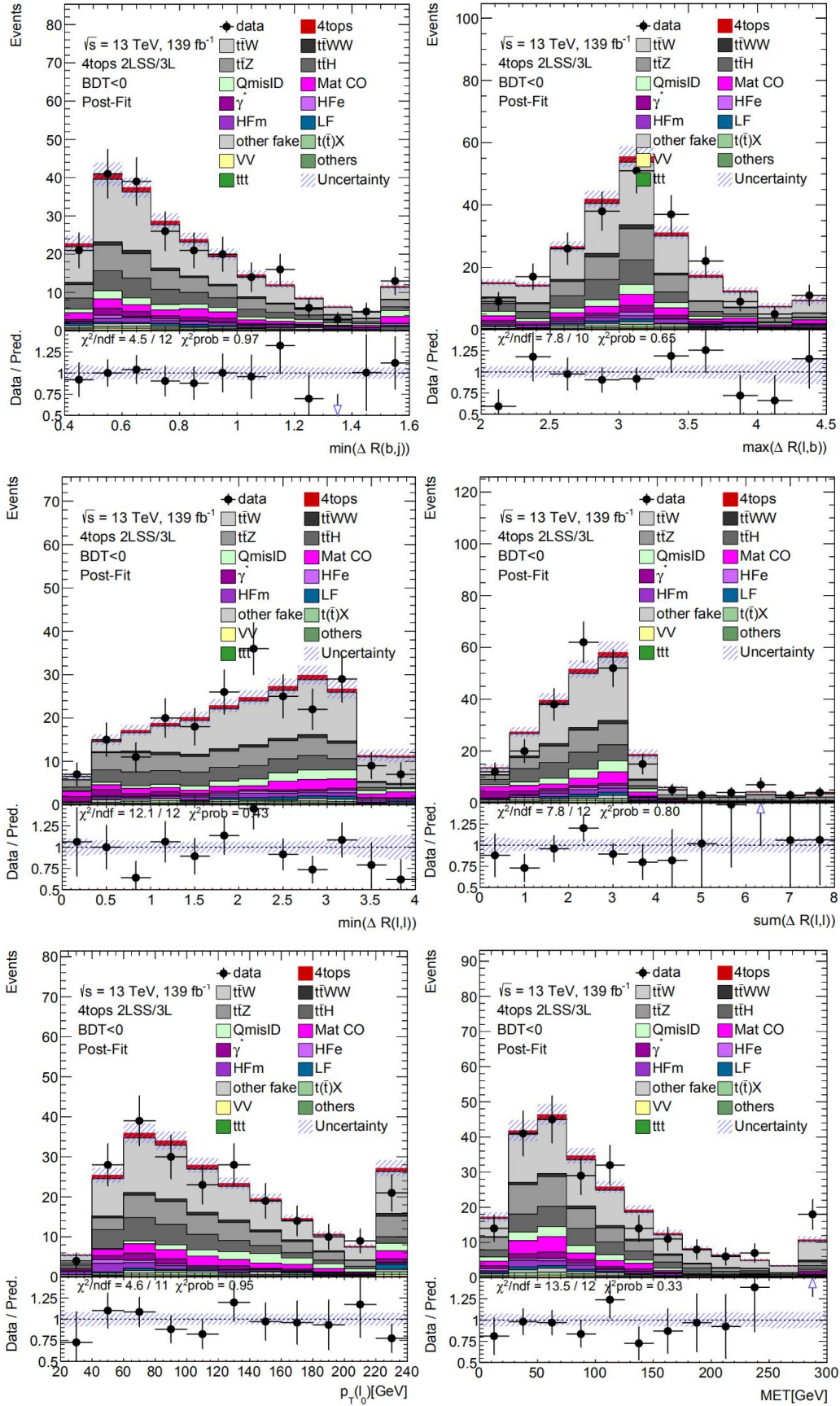


Figure 8.3 Post-fit data/MC comparison of BDT input variables in the region with $BDT < 0$

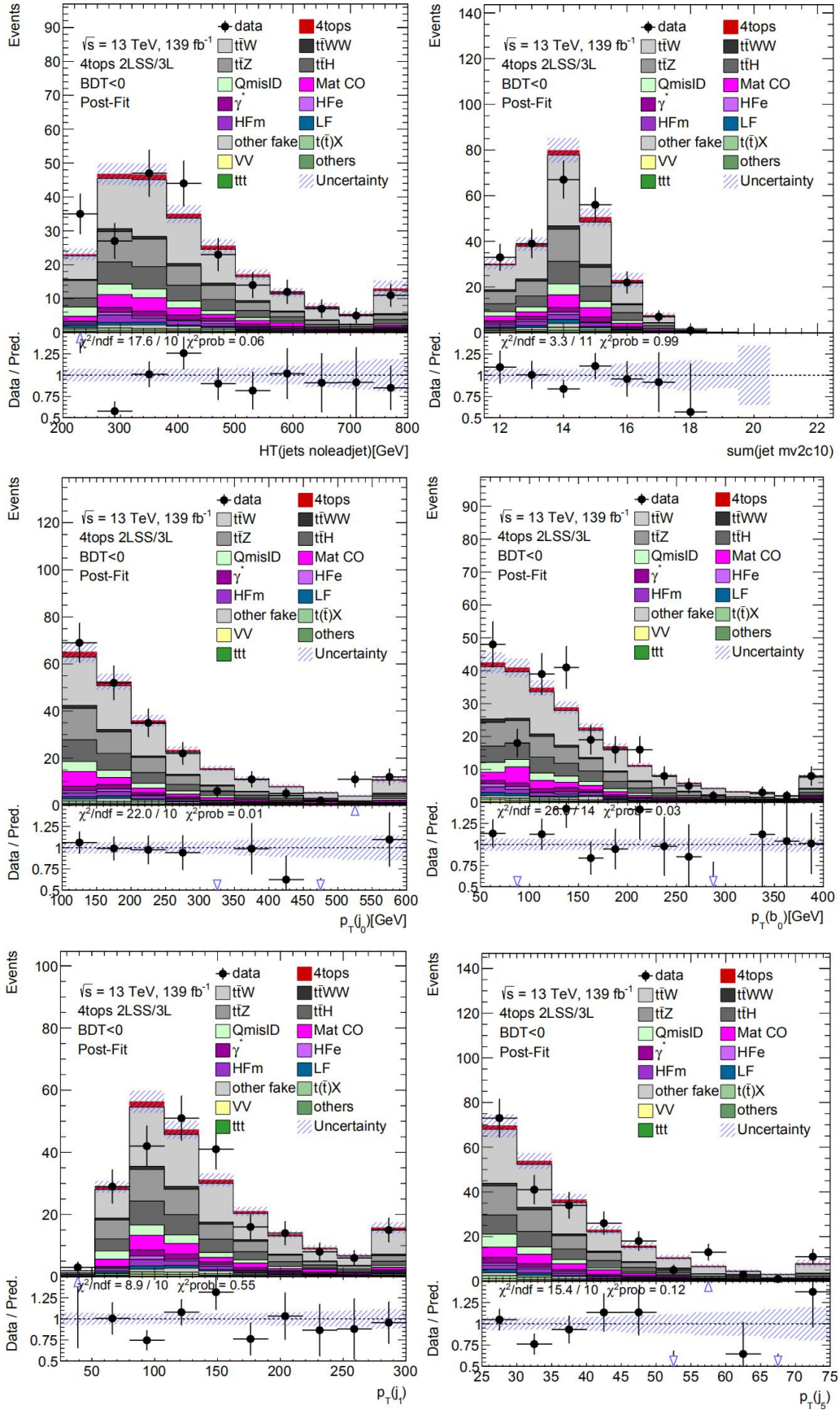


Figure 8.4 Post-fit data/MC comparison of BDT input variables in the region with $BDT < 0$

The input variables' shape comparison between signal and all the backgrounds is shown in Figure 8.5. It's observed that the

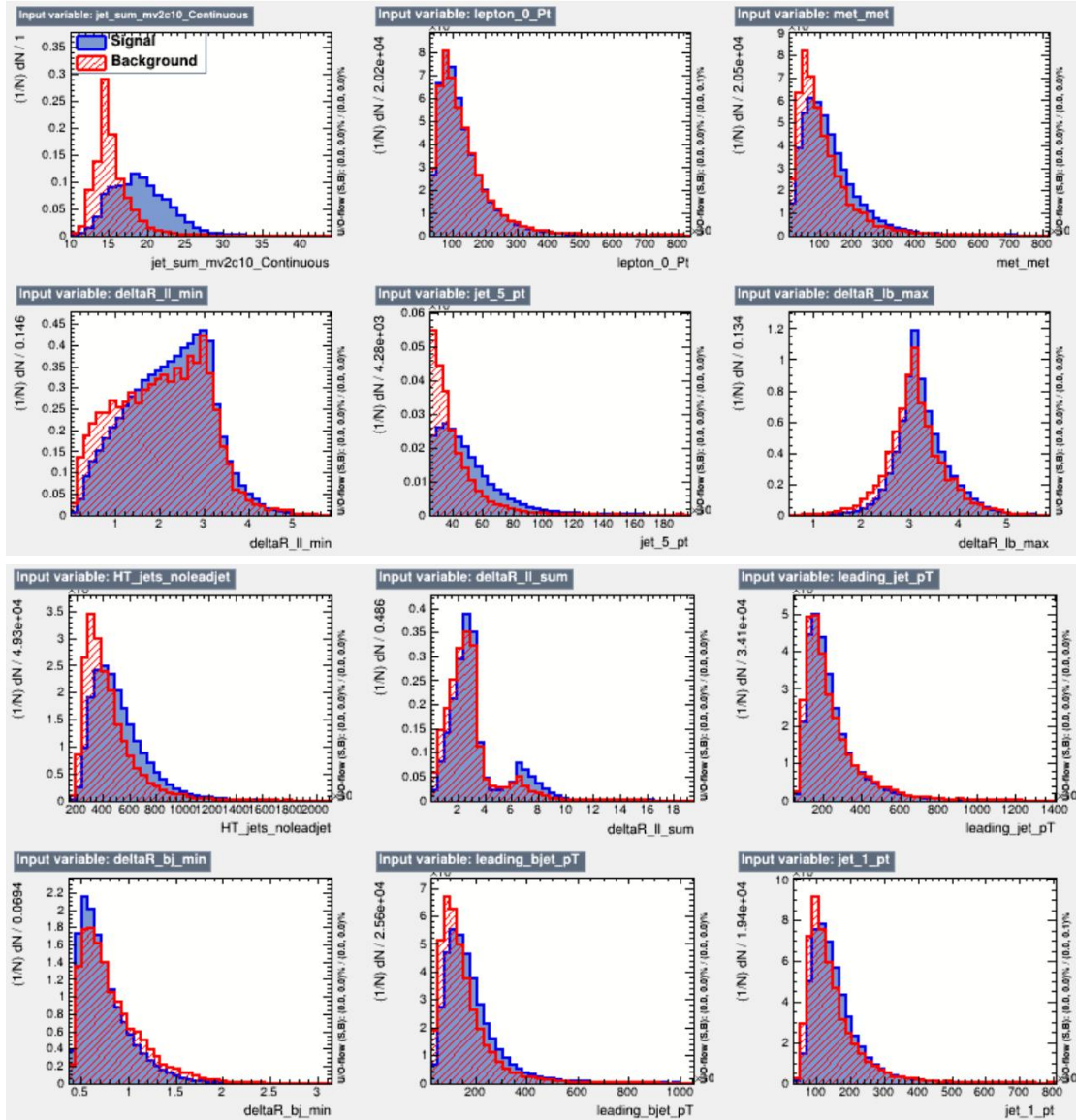


Figure 8.5 Shape comparison between signal and all background for BDT input variables

The unblinded pre-fit and post-fit BDT distributions in the signal region are shown in Figure 8.6.

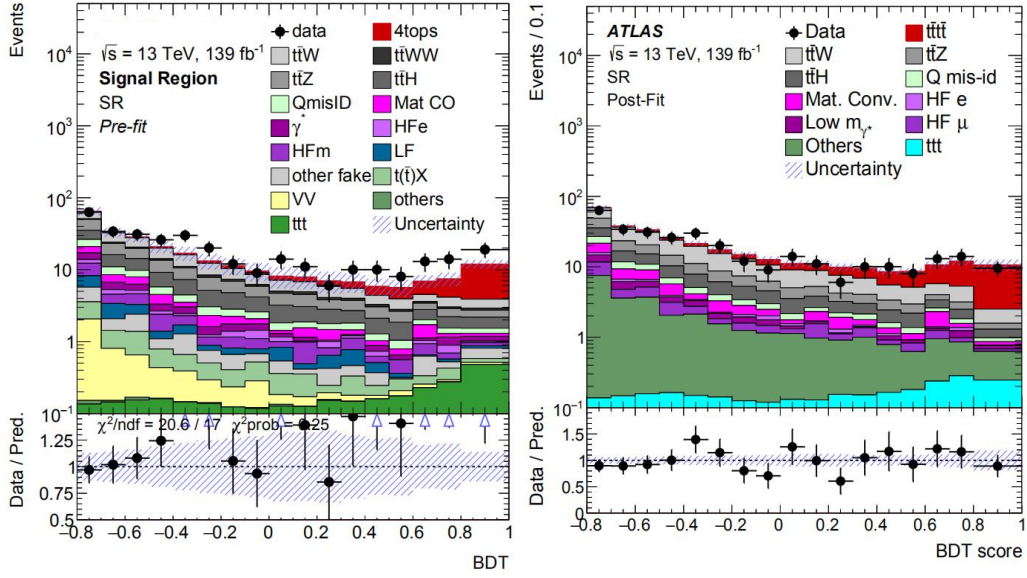


Figure 8.6 pre-fit (left) and post-fit (right) BDT distributions in the signal region

The data/MC agreement in the post-fit distribution is remarkably good. The excess of data over background is quite signal like. The signal to background ratio in the high BDT region is high, which indicates that the trained BDT has a good separation power between signal and background.

Reference:

- [1] Paul Glaysher, Judith M. Katzy, Sitong An, Iterative subtraction for feature ranking, arXiv: 1906.05718 [physics.data-an]

Chapter 9

Systematic Uncertainties

Several sources of systematic uncertainties are considered in the analysis. These systematic uncertainties will be propagated to get their impacts on the final measured $t\bar{t}t\bar{t}$ cross section. Therefore a detailed investigation and description of the systematic uncertainties is of great importance.

Generally, the systematic uncertainties can be divided into experimental uncertainties, background modelling uncertainties and signal modelling uncertainties.

9.1 Experimental uncertainties

Experimental uncertainties are introduced by the detector and object reconstruction procedure. They also include the uncertainties introduced in the data taking.

- **Data-taking.** The uncertainty of the integrated luminosity in the full Run2 dataset is 1.7% [1]. It is evaluated using the calibration of the luminosity scale using x-y beam-separation scans, following the methodology described in [2]. The uncertainty of the difference between pile-up conditions in data and MC is considered by applying an uncertainty in the applied MC scale factors so that the MC conditions match the ones in data.

- **Leptons.** There are 7 systematic uncertainties related to electrons. 2 of them are associated with the energy scale and 1 associated with energy resolution. The remaining 4 are associated to the scale factors of the electron trigger, reconstruction, identification and isolation efficiencies. For muons, there are 13 systematic uncertainties grouped into two categories [3]. The first category contains 1 uncertainty for the ID track smearing, 1 for the MS track smearing, 1 for the charge-independent momentum scale and 2 for charge-dependent momentum scale. The second group contains systematic uncertainties related to the scale factors of the muon trigger, track-to-vertex association, identification and isolation efficiencies, and each of them are further divided into the statistical and systematic components.

- **Jets.** The uncertainty related to the jet vertex tagging (JVT) is evaluated by varying the JVT cut. The jet energy scale (JES) related uncertainties correspond to a set of 29 nuisance parameters [4]. Among them, 15 are effective nuisance parameters (2 detector related, 4 modeling related, 3 mixing both aspects and 6 statistical related). 4 of them are nuisance parameters related to the η inter-calibration (1 modeling related, 2 for non-closure of high energy and high η and 1 statistical related). 3 nuisance parameters are related to the jet flavour and 3 are related to the pile-up subtraction. There are another 2 parameters related to the treatment of punch-through. 1 related to the non-closure of AFII [5] and 1 related to the single particle response at high p_T . The jet energy resolution (JER) is measured separated in data and MC using in-situ techniques [6]. The uncertainties related to JER is considered by 9 nuisance parameters, where 7 of them are effective nuisance parameters resulting from the correlation matrix diagonalization of the JER measurement and 2 of them accounting for the difference between data and simulation (1 for full simulation and 1 for fast simulation).

- Heavy-flavour jets. The uncertainties related to heavy-flavour jets correspond to 85 independent nuisance parameters. These nuisance parameters are obtained by diagonalizing the error matrix across every pair of kinematic bins which are used to calculate heavy-flavour efficiency corrections. 45 of them are related to the b-jets identification efficiency, and two sets of 20 nuisance parameters are related to c-jets and light jets mis-tagging rates, respectively.

- Missing transverse energy. The systematic uncertainty of the missing transverse energy is accounted for by three nuisance parameters, which are related to the soft terms [7]. The uncertainty is estimated in a $Z \rightarrow ee$ MC sample, where no missing transverse energy is expected, to check the ability of MC to model the soft terms.

9.2 Background modelling uncertainties

9.2.1 $t\bar{t}$ +jets related backgrounds

- Charge mis-identification

The systematic uncertainties of the charge mis-identification rates include the following sources:

- 1) The statistical uncertainty that is taken from the likelihood fit.
- 2) The difference between the rates obtained with the likelihood minimization method and the truth method performed in a Z +jets sample.
- 3) The variation of the Z peak mass window size. 8 and 12 GeV window sizes are used to assess the uncertainty, while 10 GeV is used as the nominal window size.

The total systematic uncertainty is the quadratic sum of all the above components.

The results for the total systematic uncertainty and the different systematic components in two-dimensional map of the electron's p_T and the electron's $|\eta|$ are shown in Appendix A.

The systematic uncertainty on the lepton-level charge mis-identification rates needs to be propagated to the event-level weights so that we can assess the impact of the systematics on the background yields estimation. The uncertainty of the event-level charge mis-identification weights takes the following form [8]:

$$\Delta w = \frac{\sqrt{(1-2\varepsilon_1)^2 \Delta\varepsilon_2^2 + (1-2\varepsilon_2)^2 \Delta\varepsilon_1^2 + (1-2\varepsilon_1)(1-2\varepsilon_2)\rho_{12}\Delta\varepsilon_1\Delta\varepsilon_2}}{(1-\varepsilon_1-\varepsilon_2+2\varepsilon_1\varepsilon_2)^2} \quad 9.1$$

where $\Delta\varepsilon_1$ and $\Delta\varepsilon_2$ stand for the lepton-level charge mis-identification uncertainty of the first lepton and the second lepton, and ρ_{12} stands for the correlation coefficient between ε_1 and ε_2 . When the lepton is a muon, the uncertainty is assumed to be 0. The correlation coefficients between the charge mis-identification rates are directly taken from the likelihood fit.

In the conversion control region, in order to reduce the impact of low statistics, the systematics of the charge mis-identification rates are provided in two-dimensional format, as a function of the electron's p_T and the electron's invariant mass at the primary vertex. Detailed results of the systematic uncertainties are shown in Appendix A.

- Non-prompt and Fake lepton

- 1) Material photon conversion and virtual photon conversion. The normalization factor of this component is determined in the combined fit, so no corresponding normalization uncertainty is assigned. The shape uncertainty is obtained by comparing data with a POWHEG+PYTHIA8 $Z \rightarrow \mu\mu$ sample in $Z(\mu\mu)+\gamma$ enriched region.

2) Heavy flavor decay. The uncertainty of this component is estimated from a bin-by-bin comparison between the data and MC prediction, respectively for electrons and muons.

3) Light flavor fakes. Since this part has a minor contribution to the analysis, an ad hoc normalization uncertainty of 100% is assigned, according to previous studies [9].

4) Other fakes. This part mainly refers to jets misidentified as leptons and also has a minor contribution. An normalization uncertainty of 30% is assigned. This value corresponds to some conservative estimations coming from the comparison between data and prediction in loose regions.

An additional uncertainty of 30% is assigned to the $t\bar{t}$ +jets events with three truth b-jets and a separate 30% uncertainty to the events with four or more truth b-jets.

9.2.2 non- $t\bar{t}$ +jets backgrounds

- $t\bar{t}W$, $t\bar{t}Z$ and $t\bar{t}H$ production. These three processes share the same modelling uncertainties. The uncertainty of the choice of generator is assessed by comparing different MC generator settings. For $t\bar{t}W$, NLO SHERPA with 1 additional jet is the nominal setting and $M_{ADGRAPH5_AMC@NLO}$ is the alternative setting. For $t\bar{t}Z$, $M_{ADGRAPH5_AMC@NLO}$ is the nominal setting and NLO SHERPA with no additional jets is the alternative setting. For $t\bar{t}H$, POWHEG is the nominal setting and $M_{ADGRAPH5_AMC@NLO}$ is the alternative setting. The uncertainty of the renormalization and factorization scales is assessed by varying the scales by a factor of 2 and 0.5 compared to the nominal value. The uncertainty of the flavour content is considered by assigning an ad hoc 50% uncertainty respectively for events with three truth b-jets and four or more truth b-jets. The uncertainties of $t\bar{t}Z$ and $t\bar{t}H$ cross sections are assigned to be 15% for $t\bar{t}Z$ and 20% for $t\bar{t}H$. Since the $t\bar{t}W$ cross section is measured in the combined template fit, no corresponding uncertainty is assigned. An additional 125% (300%) uncertainty is assigned for $t\bar{t}W$ in the $N_{jet} = 7$ ($N_{jet} \geq 8$) region to account for the possible mis-modeling in the high jet multiplicity region (see Figure 7.18).

- Production of single top related processes. These mainly include tZ and tWZ processes, since other productions are mainly treated as part of the $t\bar{t}$ +jets background. According to previous analyses [10], a total uncertainty of 30% is applied.

- Other processes have minor contribution to this analysis. The total uncertainty of the cross-section is 30% for V+jets and 40% for diboson (VV) production respectively, according to previous analysis [10]. The uncertainty of the ttt cross section is 100%. Uncertainties related to the flavor content is assigned to be 50% for events with three truth b-jets and 50% for events with four truth b-jets or more.

9.3 Signal modelling uncertainties

The uncertainty of the parton shower and hadronization for the $t\bar{t}t\bar{t}$ signal is assessed by the comparing $M_{ADGRAPH5_AMC@NLO}$ interfaced with PYTHIA8 and interfaced with HERWIG7. The uncertainty of the factorization and renormalization scale is assessed by varying the scale value by a factor of 2 and 0.5 compared to the nominal value.

The impact of the leading systematic uncertainties on the post-fit signal strength ($\pm 1\sigma$ variation) is summarized in Table 9.1. The systematics are divided into different categories, and in each category, different systematic sources are ordered by their impact on the fitted signal

strength.

Systematic Source	$\Delta\mu (-1\sigma)$	$\Delta\mu (+1\sigma)$
Signal modelling		
$t\bar{t}t\bar{t}$ theoretical cross section	-0.31	+0.56
$t\bar{t}t\bar{t}$ modeling	-0.09	+0.15
Background modelling		
$t\bar{t}W$ +jets modelling	-0.27	+0.26
ttt modelling	-0.07	+0.10
Non-prompt leptons modelling	-0.04	+0.05
$t\bar{t}H$ +jets modelling	-0.01	+0.04
$t\bar{t}Z$ +jets modelling	-0.04	+0.02
Other background modelling	-0.02	+0.03
Charge misassignment	-0.02	+0.01
Instrumental		
Jet uncertainties	-0.08	+0.12
Jet flavour tagging (light-flavour jets)	-0.06	+0.11
Simulation sample size	-0.06	+0.06
Luminosity	-0.03	+0.05
Jet flavour tagging (b-jets)	-0.02	+0.04
Jet flavour tagging (c-jets)	-0.01	+0.03
Other experimental uncertainties	-0.01	+0.03
Total systematic uncertainty	-0.44	+0.70
Statistical		
Non-prompt leptons normalization	-0.04	+0.05
$t\bar{t}W$ normalization	-0.04	+0.04
Total uncertainty	-0.60	+0.83

Table 9.1 Summary of the impact of the leading systematic uncertainties on the post-fit signal strength

In the above table, the uncertainty of the $t\bar{t}t\bar{t}$ theoretical cross section is an artificial uncertainty that does not affect the final measured $t\bar{t}t\bar{t}$ cross section, but only the ratio of the measured cross section to the SM expected one (μ , see Chapter 10). Apart from this unique source, the $t\bar{t}W$ modeling is the dominant systematic among all the other sources, where the uncertainty ranges from -0.27 to 0.26. The second dominant source is the signal modeling, where the uncertainty ranges from -0.09 to 0.15. The uncertainties related to the jets come next. The statistical uncertainty which is comparable to the total systematic uncertainty has a large contribution to the total uncertainty.

Reference:

- [1] G. Avoni et al., The new LUCID-2 detector for luminosity measurement and monitoring in ATLAS, JINST 13 (2018) P07017.
- [2] ATLAS Collaboration, Luminosity Determination in pp Collisions at $\sqrt{s} = 8$ TeV using the ATLAS Detector at the LHC, Eur. Phys. J. C 76 (2016) 653, arXiv: 1608.03953 [hep-ex].
- [3] ATLAS Internal, [MCP Analysis Guidelines](#), 2018.
- [4] ATLAS Internal, [JetEtMiss Recommendations R21](#), 2018.
- [5] ATLAS Collaboration, The ATLAS Simulation Infrastructure, The European Physical Journal C 70 no. 3, (2010) 823-874, arXiv:1005..4568 [physics.ins-det].
- [6] G. Aad et al., Jet energy measurement with the ATLAS detector in proton-proton collisions at $\sqrt{s} = 7$ TeV, Eur. Phys. J. C73 (2013) 2304, arXiv: 1112.6426 [hep-ex].
- [7] ATLAS Collaboration, E_{τ}^{miss} performance in the ATLAS detector using 2015-2016 LHC pp collisions, [ATLAS-CONF-2018-023](#), 2018.
- [8] ATLAS Collaboration, Search for new physics using events with b-jets and a pair of same charge leptons in pp collisions from 2015-16 at $\sqrt{s} = 13$ TeV with the ATLAS detector.
- [9] ATLAS Collaboration, Analysis of $t\bar{t}H$ and $t\bar{t}W$ production in multilepton final states with the ATLAS detector, [ATLAS-CONF-2019-045](#) (2019).
- [10] M.Aaboud et al., Search for new phenomena in events with same-charge leptons and b-jets in pp collisions at $\sqrt{s} = 13$ TeV with the ATLAS detector, JHEP 12 (2018) 039, arXiv: 1807.11883 [hep-ex].

Chapter 10

Statistical Treatment and Results

A statistical analysis is performed to extract the final parameter of interest (POI). In this analysis the POI is the $t\bar{t}t\bar{t}$ signal strength μ : i.e. the ratio of the measured $t\bar{t}t\bar{t}$ cross section to the expected Standard Model $t\bar{t}t\bar{t}$ cross section. A Poisson likelihood represents the probability of having the observed number of events in data when the number of expected events is given:

$$L(\mu, \theta) = \prod_{i \in \text{bins}} P(n_i | \mu s_i(\theta) + b_i(\kappa, \theta)) \prod_{j \in \theta} G(\theta_j), \quad 10.1$$

where n_i is the number of observed events, s_i is the number of expected signal yields and b_i is the number of expected background yields in each bin. κ is the background normalization factor. In this analysis, the normalization factors for the $t\bar{t}W$ process and for the different fake components are left free floating and determined in the fit. The normalization factors for other backgrounds are fixed at 1, which means we completely rely on the MC predictions for these backgrounds. θ are the nuisance parameters, which represent the systematic uncertainties. $G(\theta)$ are the Gaussian functions, which are used to add constraints on the nuisance parameters. The product index i runs over all the bins in all of the regions considered, and j runs over all the nuisance parameters.

The profile likelihood ratio is used as test statistics, which is expressed in equation 10.2:

$$q_\mu = -2 \ln(L(\mu, \hat{\kappa}_\mu, \hat{\theta}_\mu) / L(\hat{\mu}, \hat{\kappa}, \hat{\theta})), \quad 10.2$$

where $L(\hat{\mu}, \hat{\kappa}, \hat{\theta})$ is the unconditional maximum of the likelihood, and $L(\mu, \hat{\kappa}_\mu, \hat{\theta}_\mu)$ is the conditional maximum of the likelihood for a given μ . q_μ is small when the observation is close to the hypothesized μ . The disagreement between data and the hypothesized μ is quantified by the p-value:

$$p_\mu = \int_{q_{\mu, \text{obs}}}^{\infty} f(q_\mu, \mu) dq_\mu, \quad 10.3$$

where $f(q_\mu, \mu)$ is the probability density function (PDF) of q_μ and is usually obtained with toy MC experiments [1]. For the background only hypothesis where μ is 0, the p-value is expressed as:

$$p_0 = \int_{q_{0, \text{obs}}}^{\infty} f(q_0, 0) dq_0. \quad 10.4$$

p_0 could be interpreted as the probability of the background fluctuation to produce the number of events equal to or larger than the observed value. p_0 could be translated into the standard deviation of Gaussian significance, where for instance $p_0 = 2.8 \times 10^{-7}$ corresponds to a 5σ significance. 5σ is often used as the threshold to claim discovery of a new physics process, and 3σ provides the evidence for a new physics process. However, if no obvious signal excess is found, the Confidence Levels (CLs) method [2] is used to set upper limit on the signal strength.

The constraint of the nuisance parameters is defined as the ratio of the post-fit to the pre-fit uncertainty, and the pulls are defined as the difference between the best-fit and the input values, normalized to the pre-fit uncertainty [3]. Usually the majority of the post-fit nuisance parameters lies within one standard deviation of their pre-fit values, reflecting the good agreement between

nominal simulation and data. More information about constraints and pulls can be found in [4].

Before the final fit where the signal region and all the control regions are included to extract the signal strength, a set of intermediate fitting steps are performed, which is listed below.

- Plain Asimov Fit: Both of the control regions and the signal region are included. The data used in the fit are the pseudo Asimov data [5] which corresponds exactly to the (pre-fit) MC prediction. The purpose of this fit is mainly to obtain the expected constraints on the nuisance parameters as well as the normalization factors.

- Real CR-only Fit: Only the control regions are included in this fit. The data used in the fit are the real data in the control regions. The purpose of this fit is to obtain as close as possible the post-fit background without looking at the signal region. The signal contamination is expected to be small in the control regions, therefore the signal strength is fixed to be 1 at this step.

- Realistic Asimov Fit: Both the control regions and the signal region are included. The data used in the fit are the pseudo Asimov data which corresponds exactly to the post-fit background model obtained in the Real CR-only Fit. The purpose of this fit is to obtain close to final parameter constraints and pulls, as well as the expected significance without looking at real data.

In the above intermediate fitting steps, the normalization factors of the $t\bar{t}W$ process and the different fake components are left free floating, which means they are determined by the fit. The other prompt physics backgrounds depend directly on the MC simulation and the charge mis-identification background depends directly on the data-driven estimation, so the normalization factors of these backgrounds are fixed at 1.

The final data fit is performed using both the control and signal regions and using data in all these regions.

Pre-fit distributions of kinematic variables in the $BDT > 0$ region are shown in Figures 10.1-10.3.

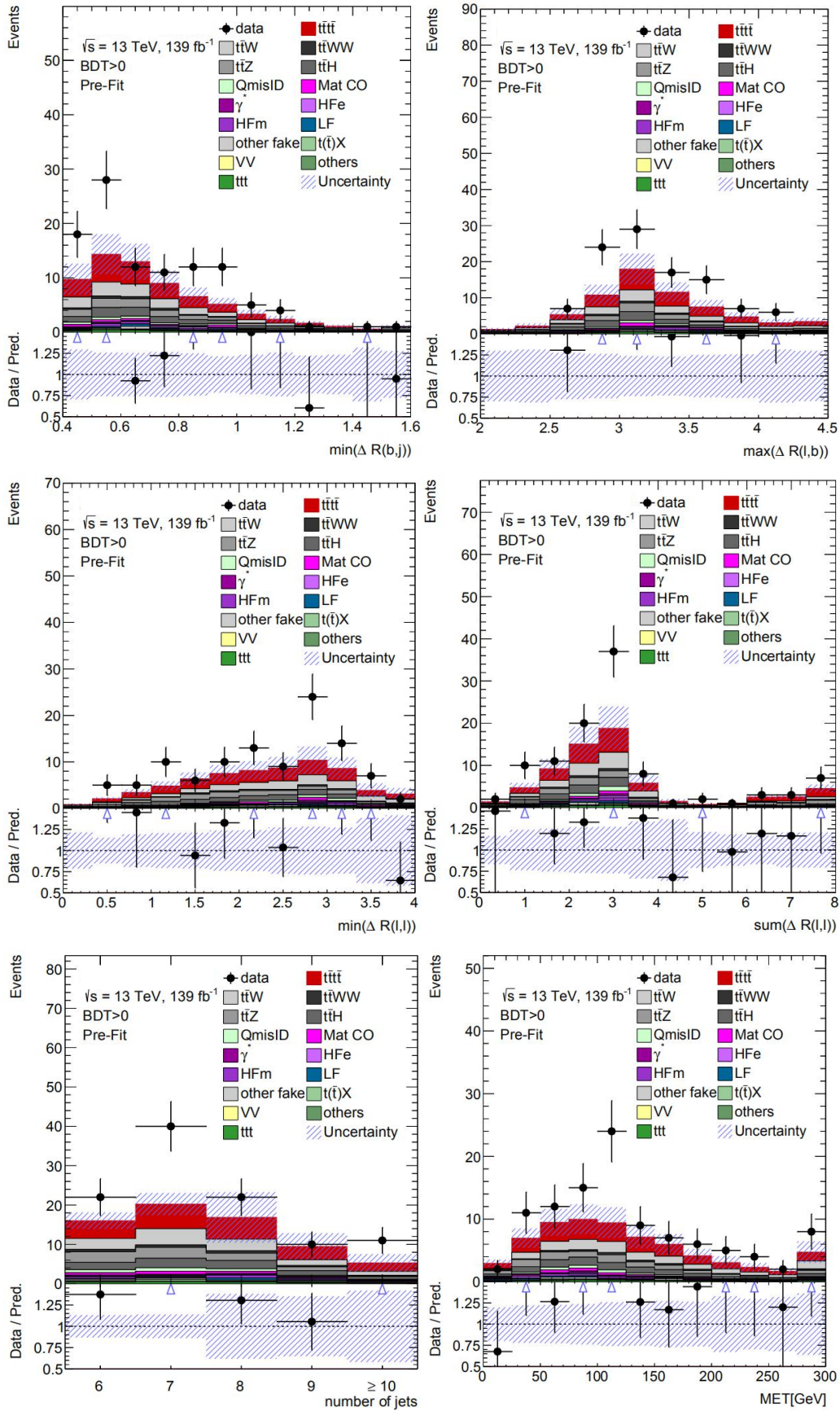


Figure 10.1 Pre-fit distributions in the $BDT > 0$ region

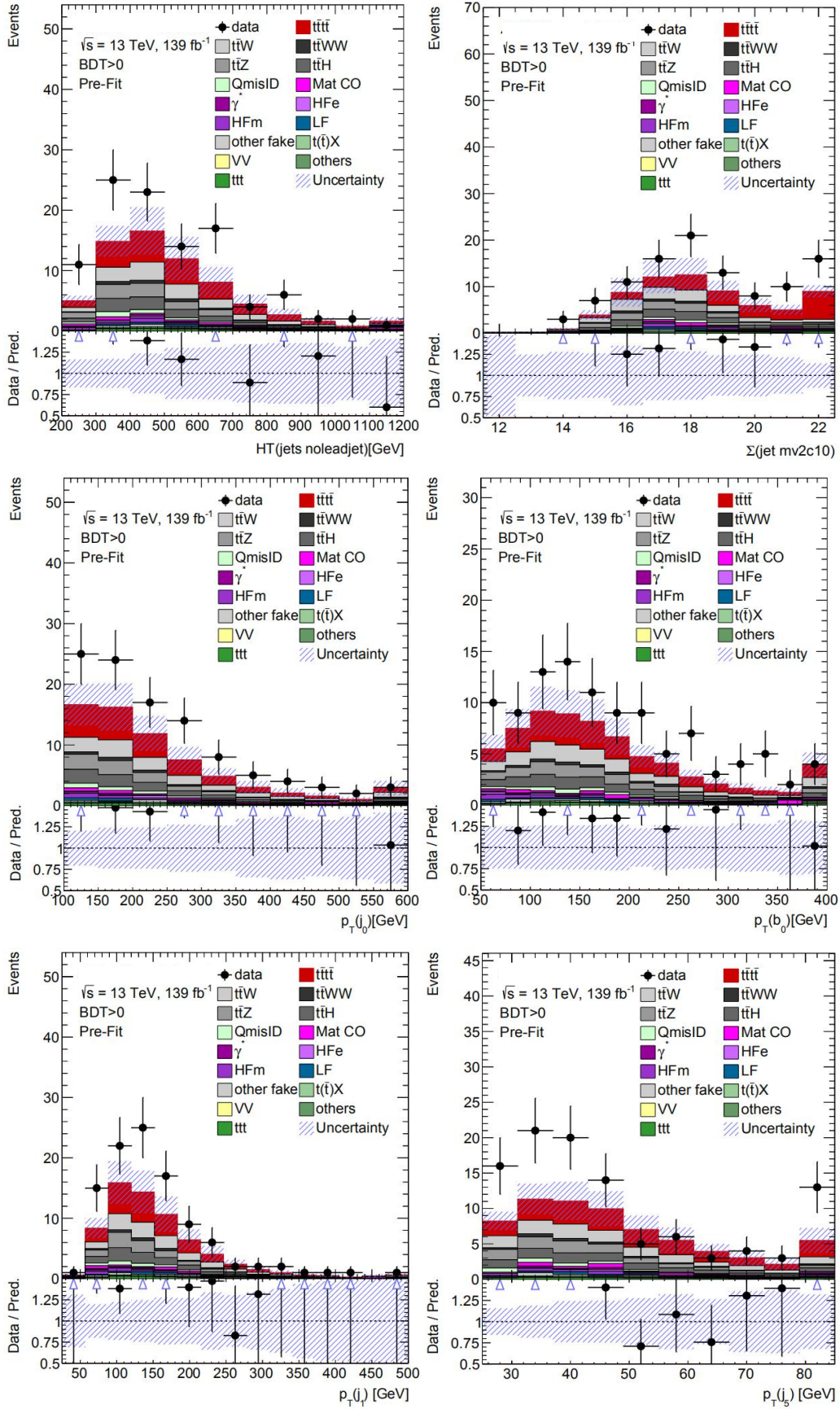


Figure 10.2 pre-fit distributions in the BDT>0 region

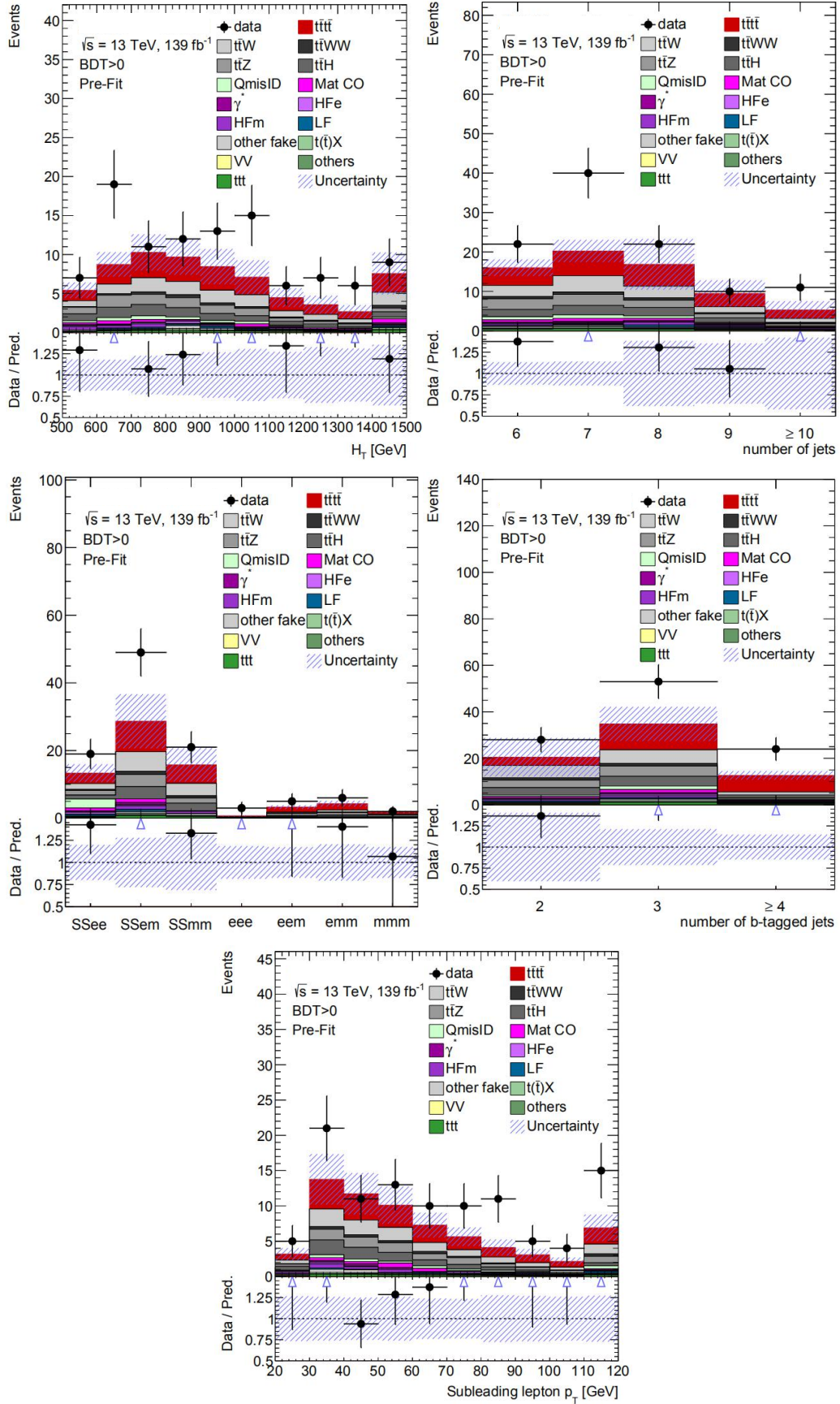


Figure 10.3 pre-fit distributions in the BDT > 0 region

The expected background and signal yields in the signal region and the $BDT > 0$ region after the plain Asimov fit are shown in Table 10.1.

	BDT>0	allBDT SR
4tops	21.9 ± 8.9	29.8 ± 12.1
$t\bar{t}W$	12.4 ± 8.7	61.2 ± 21.7
$t\bar{t}WW$	2.2 ± 1.1	7.5 ± 3.8
$t\bar{t}Z$	8.5 ± 1.9	49.7 ± 9.2
$t\bar{t}H$	8.3 ± 2.1	38.8 ± 8.8
QmisID	2.6 ± 0.2	16.2 ± 1.3
Mat CO	2.3 ± 1.0	12.7 ± 5.4
γ^*	1.1 ± 0.5	9.3 ± 3.7
HFe	0.9 ± 0.7	4.8 ± 3.1
HFm	2.0 ± 1.2	11.0 ± 4.1
LF	1.2 ± 1.2	7.0 ± 6.1
other fake	1.3 ± 0.6	6.7 ± 2.3
$t(\bar{t})X$	1.0 ± 0.4	5.1 ± 1.6
VV	0.3 ± 0.2	4.3 ± 3.0
others	0.016 ± 0.009	0.067 ± 0.034
ttt	1.9 ± 1.7	3.0 ± 2.7
Total	67.9 ± 7.9	267.2 ± 15.3

Table 10.1 Expected background and signal yields in the allBDT signal region and the $BDT > 0$ region after the plain Asimov fit

The fitted values of the normalization factors and signal strength are shown in Figure 10.4 and the ranking plot of the nuisance parameters is shown in Figure 10.5, both in the case of the plain Asimov fit.

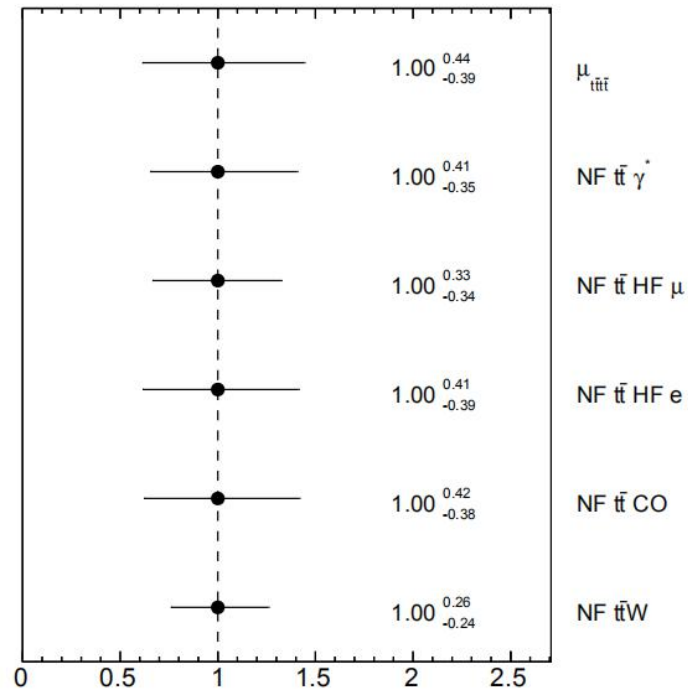


Figure 10.4 Fitted normalization factors and signal strength for the plain Asimov fit.

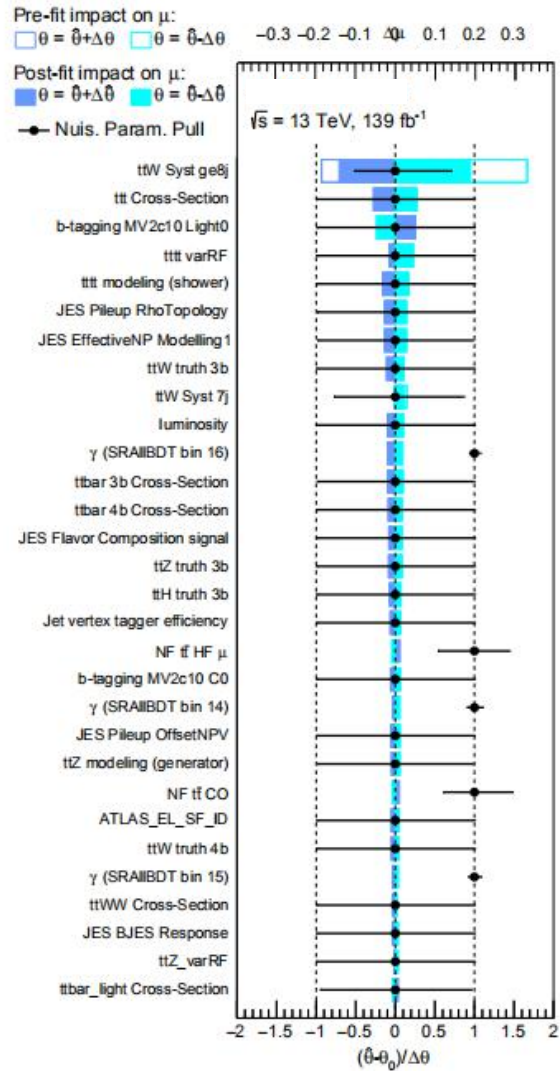


Figure 10.5 Ranking plot of the nuisance parameters for the plain Asimov fit

The fitted values of the normalization factors and signal strength for the realistic Asimov fit are shown in Figure 10.6.

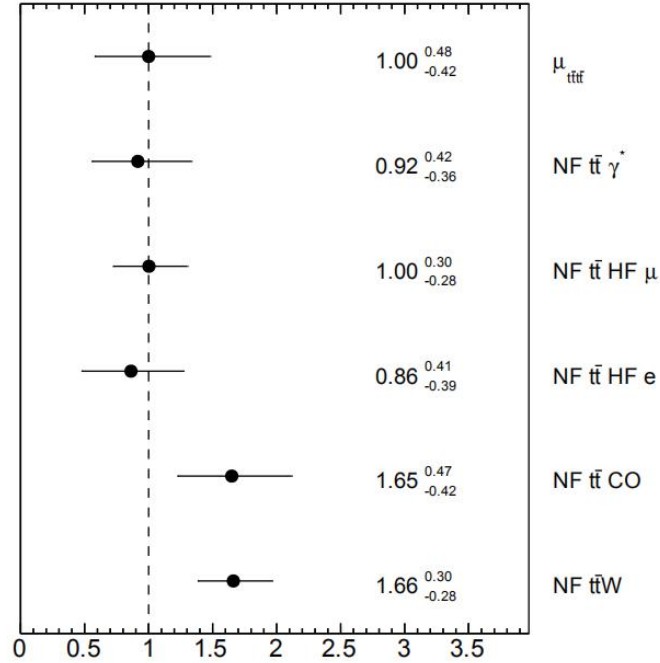


Figure 10.6 Fitted normalization factors and signal strength for the realistic Asimov fit

The fitted values of the constraints and pulls of all the nuisance parameters for the realistic Asimov fit are shown in Figure 10.7. The ranking plot of the nuisance parameters is shown in Figure 10.8.

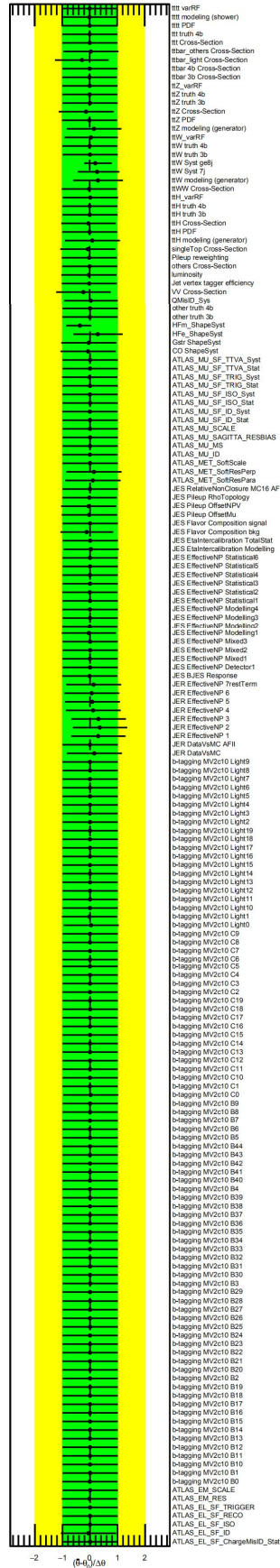


Figure 10.7 Constraints and pulls of all the nuisance parameters for the realistic Asimov fit

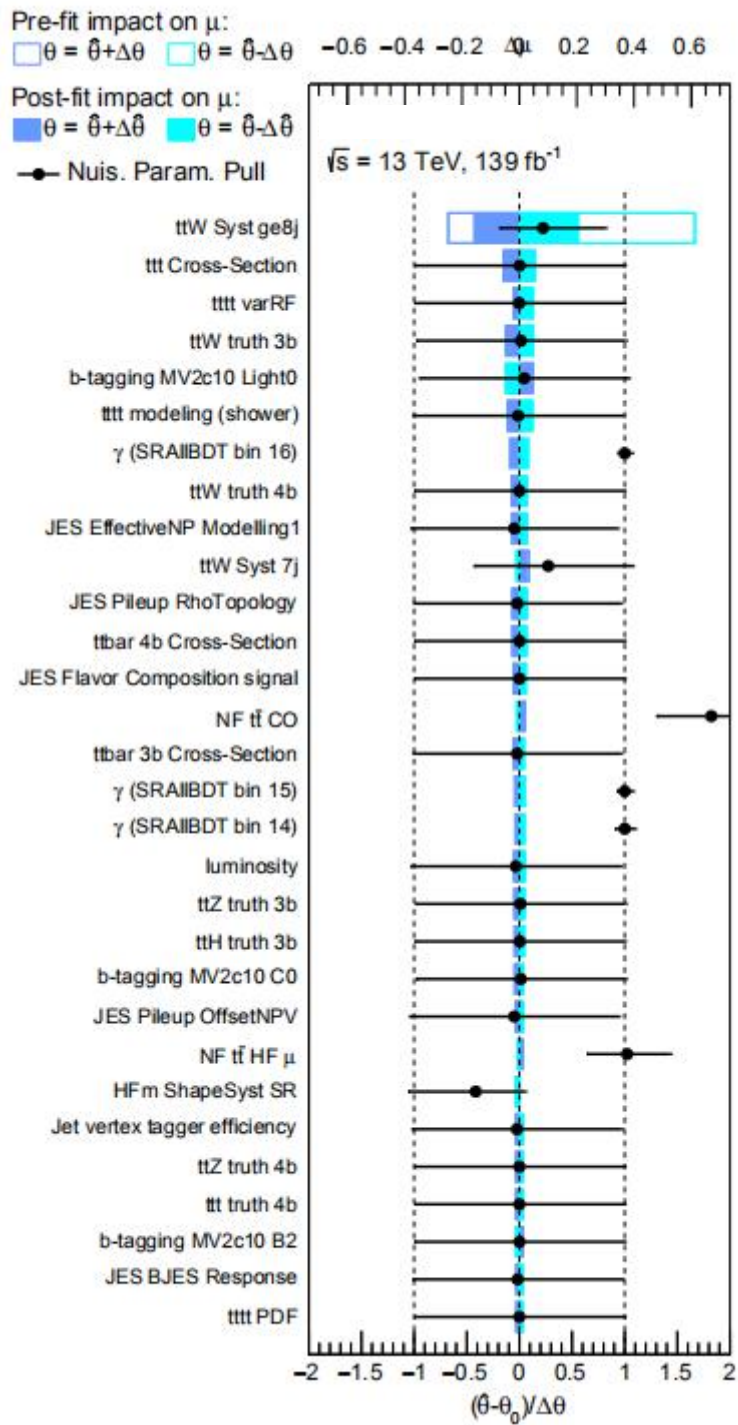


Figure 10.8 Ranking plot of the nuisance parameters for the Realistic Asimov fit

The expected significances of the intermediate fitting steps are summarized in Table 10.2.

	stat+syst	stat-only	stat+syst
SSML	2.92	3.68	2.69

Table 10.2 Expected $t\bar{t}$ significance for different intermediate fitting steps

The expected signal and background yields in the signal region after the fit on data is shown in Table 10.3.

	SR	SR and BDT > 0
$t\bar{t}W$	102 ± 26	23 ± 10
$t\bar{t}WW$	7 ± 4	2 ± 1
$t\bar{t}Z$	47 ± 9	8 ± 2
$t\bar{t}H$	38 ± 9	8 ± 2
QmisID	16 ± 1	2.7 ± 0.2
Mat CO	19 ± 6	3 ± 1
γ^*	9 ± 4	1 ± 1
HFe	3 ± 2	1 ± 1
HFm	11 ± 5	3 ± 2
LF	5 ± 5	1 ± 1
other fake	6 ± 2	2 ± 1
$t(\bar{t})X$	5 ± 2	1.0 ± 0.4
VV	3 ± 2	0.2 ± 0.1
others	4 ± 2	1 ± 1
ttt	3 ± 3	2 ± 2
Total bkg	278 ± 22	59 ± 10
$t\bar{t}t\bar{t}$	60 ± 16	44 ± 12
Total	337 ± 18	103 ± 10
Data	330	105

Table 10.3 Expected background and signal yields in the signal region after the full fit on data

The distributions of the fitted variables in each of the regions after the full data fit are shown in Figure 10.9.

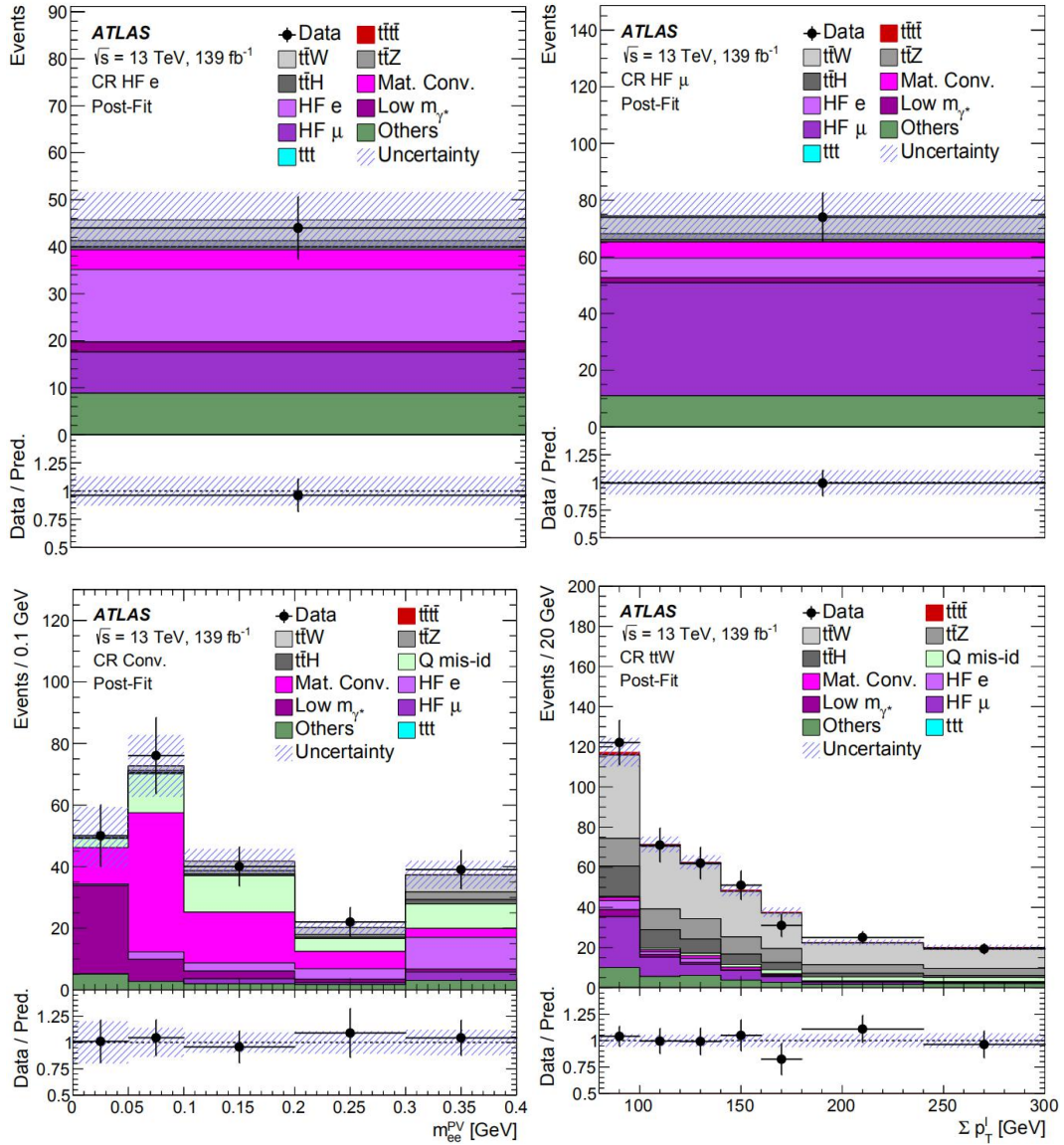


Figure 10.9 post-fit distributions of the fitted variables in each of the regions

The post-fit data/MC agreement in the control regions is remarkably good, which indicates that the backgrounds are well estimated.

The post-fit distributions of other variables in the SR>0 region are shown in Figures 10.10-10.12.

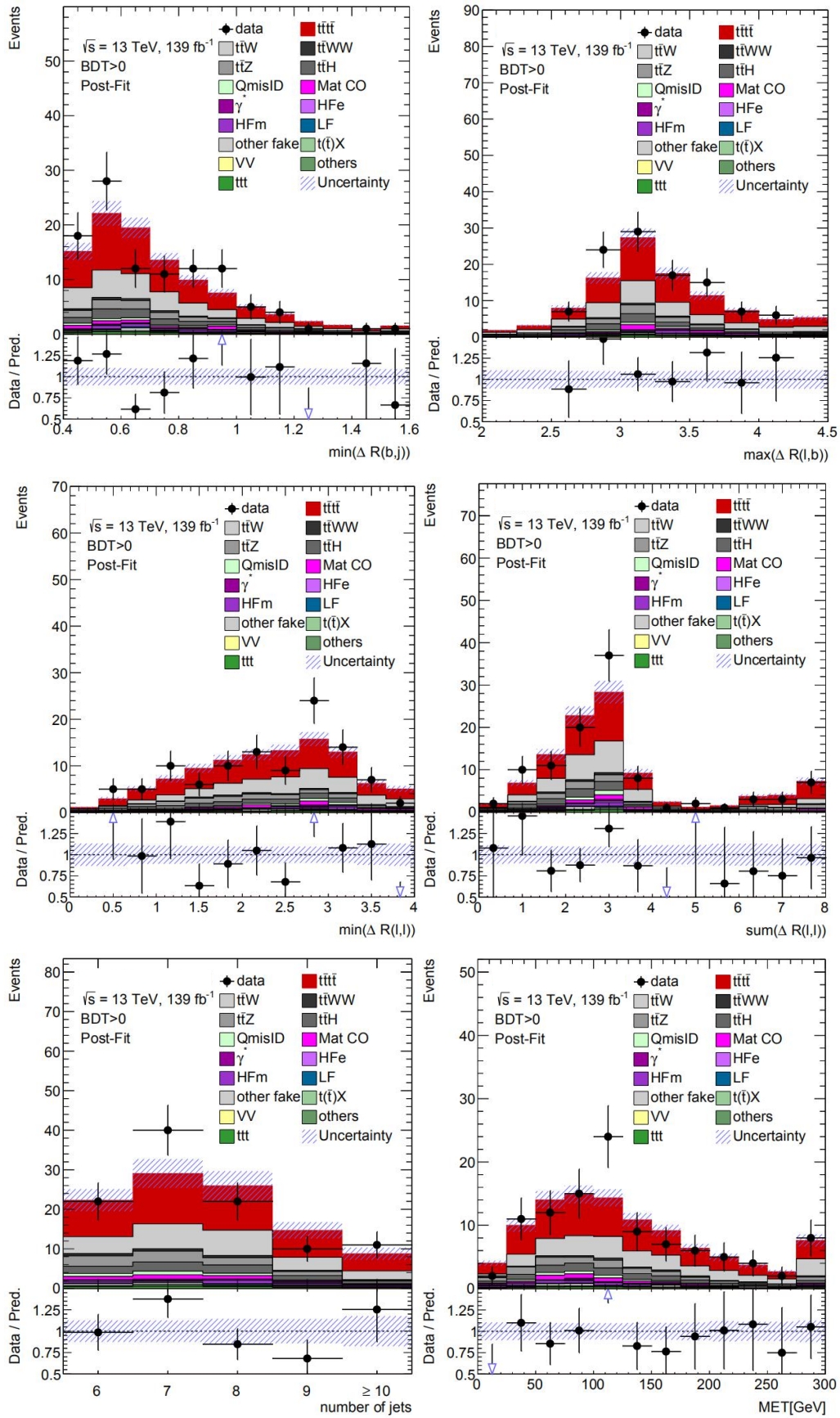


Figure 10.10 post-fit distributions in the BDT>0 region

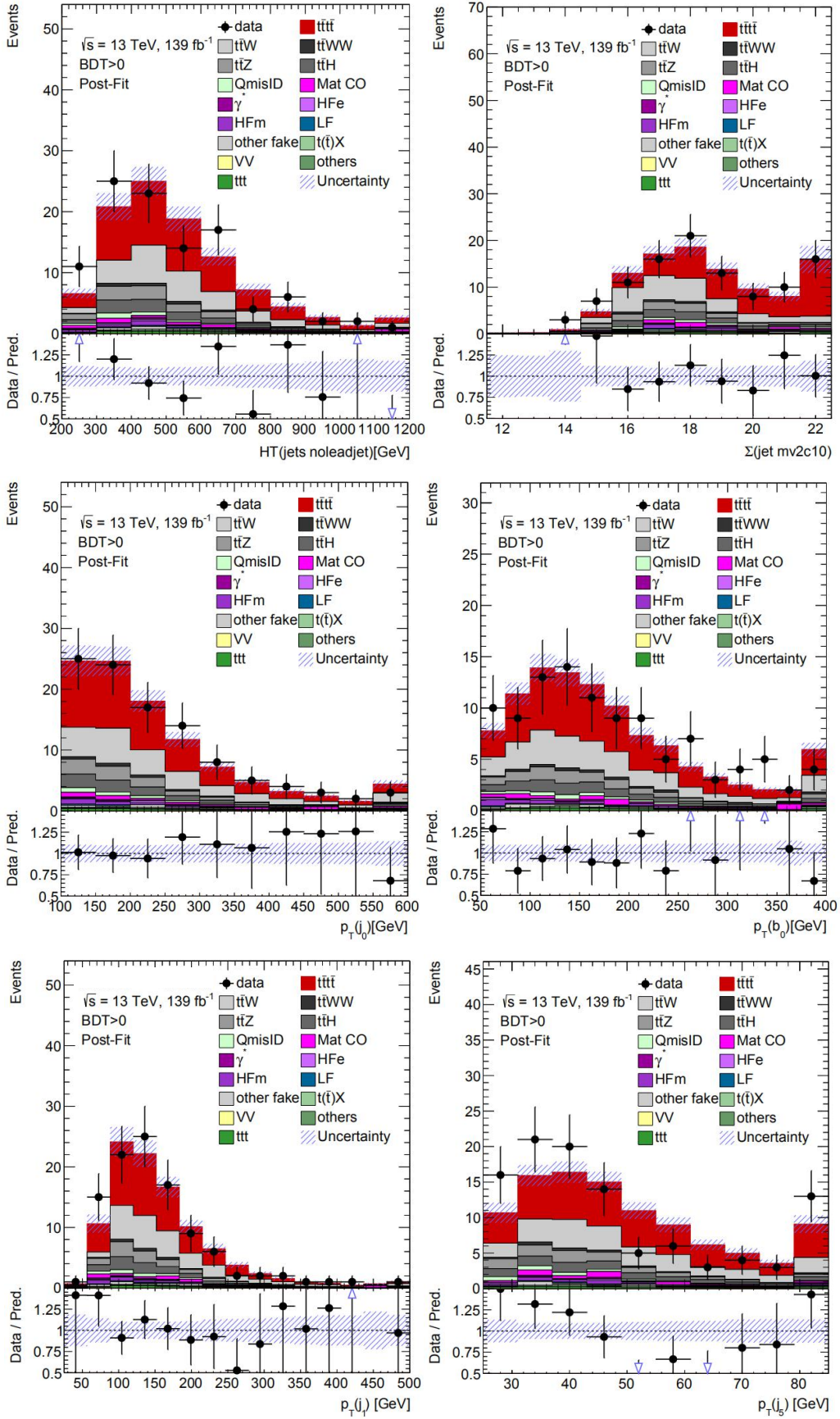


Figure 10.11 post-fit distributions in the $BDT > 0$ region

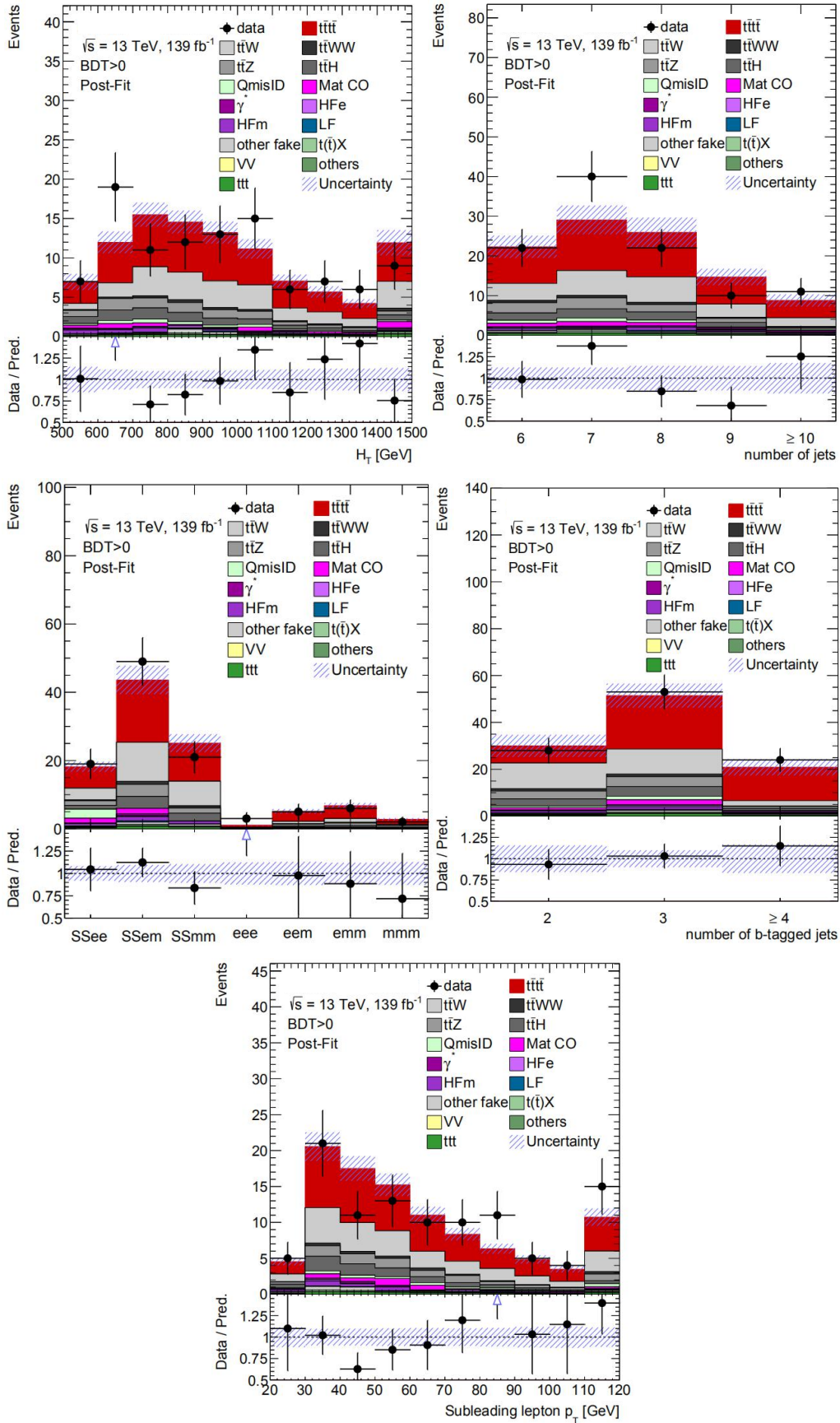


Figure 10.12 post-fit distributions in the $BDT>0$ region

From the above post-fit distributions, we observe that in the signal region, the level of

data/MC agreement is acceptable, and the excess of data over background is quite signal-like.

The fitted normalization factors and signal strength for the full fit on data are shown in Figure 10.13. Constraints and pulls of the nuisance parameters are shown in Figure 10.14. The ranking plot of the nuisance parameters is shown in Figure 10.15.

From the results, we see that the normalization factors for γ^* , HF μ and HF e are close to 1, representing an overall good MC modelling of these processes. The normalization factor for the $t\bar{t}W$ +jets background is compatible with the observation from the previous analysis [6], where the reference theoretical $t\bar{t}W$ +jets background cross section was scaled up by 20% to account for extra jet production and EW effects compared to the theoretical cross section used in this analysis. The post-fit value of the nuisance parameter for the systematic uncertainty in the $t\bar{t}W$ background with $N_{\text{jets}} = 7$ and $N_{\text{jets}} \geq 8$ regions are $0.22^{+0.56}_{-0.42}$ and $0.18^{+0.73}_{-0.61}$ respectively. The constraints are mainly due to the fact that an uncertainty of 125% (300%) is added to the $t\bar{t}W$ $N_{\text{jets}} = 7$ ($N_{\text{jets}} \geq 8$) region in order to cover the the difference between the number of data events and MC yields in that region. Apart from these, no other nuisance parameters are found to be significantly constrained by the fit.

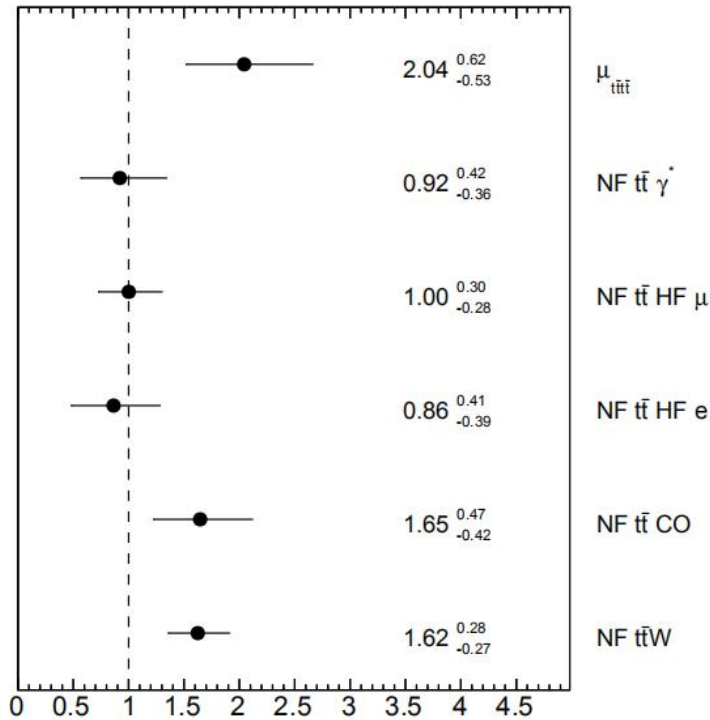


Figure 10.13 Fitted normalization factors and signal strength for the full fit on data

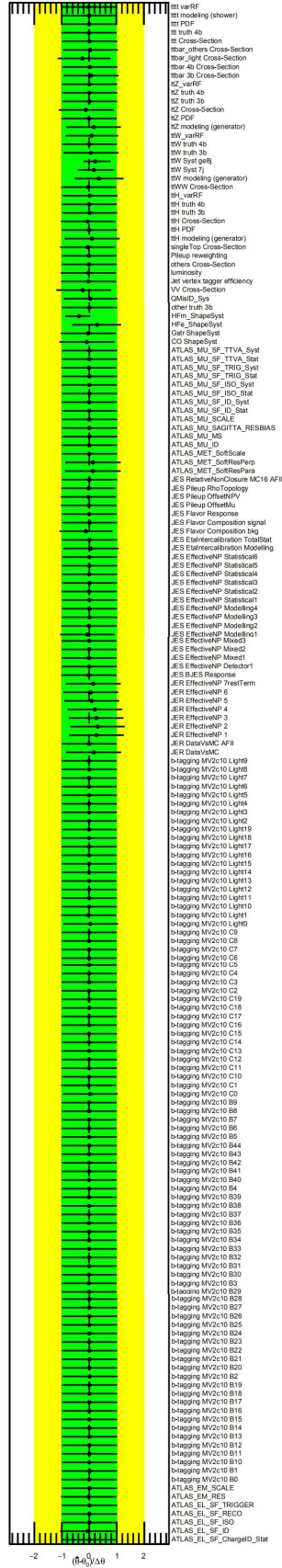


Figure 10.14 Constraints and pulls of all the nuisance parameters for the full fit on data

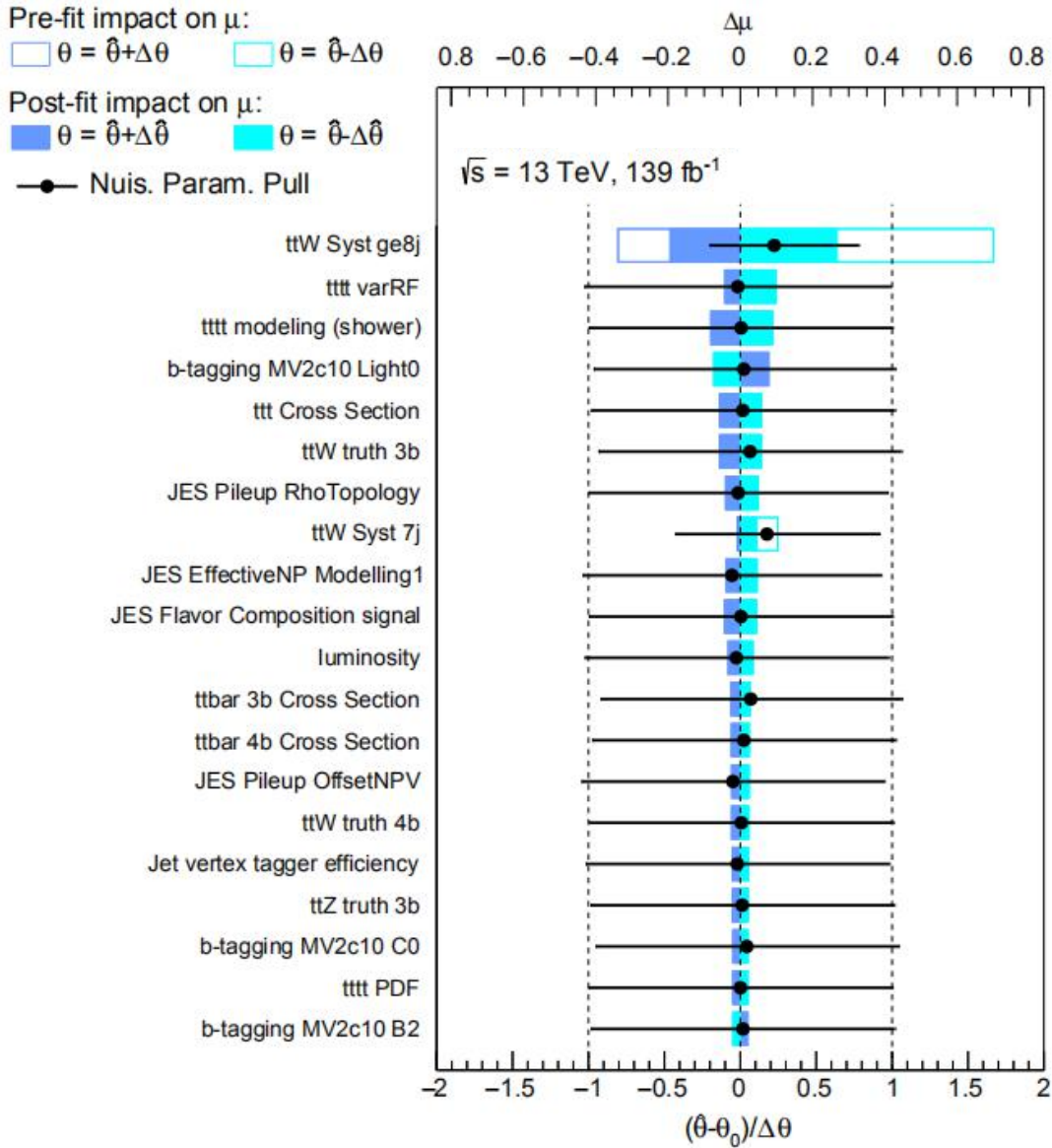


Figure 10.15 Ranking plots of the nuisance parameters for the full fit on data

From the ranking plot, it's observed that the nuisance parameter corresponding to $t\bar{t}W$ $N_{\text{jets}} \geq 8$ region has the largest impact on the fitted signal strength since this region also contributes a lot in the high BDT signal region. Other important nuisance parameters include the uncertainties of the $t\bar{t}t\bar{t}$ renormalization factor, $t\bar{t}t\bar{t}$ shower modelling and the light jet mis-tagging.

Finally, the observed excess of data over background corresponds to a significance of 4.3 standard deviations, with the expected significance of 2.4 standard deviations. The best-fit signal strength is:

$$\mu = 2.0_{-0.4}^{+0.4}(\text{stat})_{-0.4}^{+0.7}(\text{syst}) = 2.0_{-0.6}^{+0.8} \quad 10.5$$

Converting the signal strength into a cross section by multiplying μ with the expected SM $t\bar{t}t\bar{t}$ cross section, the measured $t\bar{t}t\bar{t}$ production cross section gives:

$$\sigma_{t\bar{t}} = 24_{-5}^{+5}(\text{stat})_{-4}^{+5}(\text{syst})fb = 24_{-6}^{+7}fb \quad 10.6$$

The measured $t\bar{t}$ production cross section is consistent within $(24-11.97)/6 = 2$ standard deviations with the SM prediction.

Reference:

- [1] Practical Statistics for the LHC, Kyle Cranmer, CERN-2014-003 (2014) arXiv:1503.07622 [physics.data-an].
- [2] A. L. Read, Presentation of search results: the CLs technique, Journal of Physics G: Nuclear and Particle Physics 28 no. 10, (2002) 2693.
- [3] The CMS Collaboration, Measurement of the $t\bar{t}$ production cross section, the top quark mass, and the strong coupling constant using dilepton events in pp collisions at $\sqrt{s}=13\text{TeV}$, CERN-EP-2018-317 (2018), arXiv: 1812.10505 [hep-ex].
- [4] Till Moritz Karbach, Maximilian Schlupp, Constraints on Yield Parameters in Extended Maximum Likelihood Fits, 2012, arXiv:1210.7141 [physics.data-an].
- [5] Glen Cowan, Kyle Cranmer et al., Asymptotic formulae for likelihood-based tests of new physics, Eur. Phys. J. C71: 1554, 2011, arXiv:1007.1727 [physics.data-an].
- [6] ATLAS Collaboration, Analysis of $t\bar{t}H$ and $t\bar{t}W$ production in multilepton final states with the ATLAS detector, [ATLAS-CONF-2019-045](#), 2019.

Chapter 11

Conclusion and Outlook

This thesis presents the search for the SM $t\bar{t}t\bar{t}$ production in the same sign di-lepton and multi-lepton (SSML) channel. The analysis has been performed using the dataset corresponding to an integrated luminosity of 139 fb^{-1} , collected by the ATLAS detector at $\sqrt{s} = 13 \text{ TeV}$. Events with at least two same sign leptons, high jet and b-jet multiplicities and high system energy are selected. A multivariate analysis is performed to further separate signal from background. An excess of signal over background corresponding to an observed (expected) significance of 4.3 (2.4) standard deviations is found, which provides the first evidence for SM $t\bar{t}t\bar{t}$ production. The CMS collaboration also performed the SM $t\bar{t}t\bar{t}$ search in the SSML and multi-lepton channel using 137 fb^{-1} dataset, which gives an observed (expected) significance of 2.6 (2.7) standard deviations. It is found that we observed more $t\bar{t}t\bar{t}$ signal like events in the ATLAS experiment.

The measured $t\bar{t}t\bar{t}$ production cross section is $\sigma_{t\bar{t}t\bar{t}} = 24_{-5}^{+5}(\text{stat})_{-4}^{+5}(\text{syst}) \text{ fb} = 24_{-6}^{+7} \text{ fb}$, and the corresponding signal strength is $\mu = 2.0_{-0.4}^{+0.4}(\text{stat})_{-0.4}^{+0.7}(\text{syst}) = 2.0_{-0.6}^{+0.8}$. The measured $t\bar{t}t\bar{t}$ production cross section is consistent with the SM prediction within 2 standard deviations.

For the future, in order to reach a significance of 5 standard deviations, the uncertainties need to be further reduced. In the current result, it is shown that the statistical uncertainty is still larger than the total systematic uncertainty. The LHC Run 3 data taking is expected to start from year 2022 and operate until year 2024, at a center of mass energy of 14 TeV. The integrated luminosity of the datasets after Run 3 is expected to reach 350 fb^{-1} . The statistical uncertainty would then be reduced with the larger dataset collected by ATLAS. For the systematic uncertainties, the modeling of $t\bar{t}W$ production is shown to be the dominant source. Therefore a better understanding of the $t\bar{t}W$ process is essential and more investigation on the $t\bar{t}W$ modeling is needed. In this analysis, the fake background is estimated with a semi-data-driven template fit method, where the shapes of the fake components are determined by simulation and the normalization factors are obtained in the fit. Since our knowledge about the fake background is limited, a fully data-driven estimation of the fakes would be ideal. More investigation on the data-driven techniques for the fake estimation is needed. Considering all the above aspects, I think that having a 5σ discovery for the SM $t\bar{t}t\bar{t}$ production with Run 3 data is quite promising.

In terms of the High Luminosity LHC (HL-LHC), the ultimate goal is to collect a dataset corresponding to an integrated luminosity of more than 3000 fb^{-1} at a center of mass energy of 14 TeV. It is over 20 times higher than the current integrated luminosity. In that case, the overall statistical uncertainty is expected to be reduced by a factor of 4 to 5, which means the systematic uncertainty will be dominant. Even we take the current systematic uncertainties, we have $\sigma_{t\bar{t}t\bar{t}} = 24_{-1}^{+1}(\text{stat})_{-4}^{+5}(\text{syst}) \text{ fb} \approx 24_{-4}^{+5} \text{ fb}$, which corresponds to 6 sigma for the background-only hypothesis. For the precision measurement, we should try our best to further reduce the systematic uncertainties. Excellence is our pursuit.

Appendix A

Systematic Uncertainty of the Charge Mis-identification Rates

The total systematic uncertainties and different systematic components of the electron charge mis-identification rates are shown in Figure A.1-A.12, respectively for the nominal case, the $t\bar{t}W$ control region and the conversion control region. In the nominal case and the $t\bar{t}W$ control region, the systematic uncertainties are provided as a function of electron's p_T and electron's $|\eta|$. In the conversion control region, the systematic uncertainties are provided as a function of electron's p_T and the electron's invariant mass at the primary vertex ($M_{ee@PV}$).

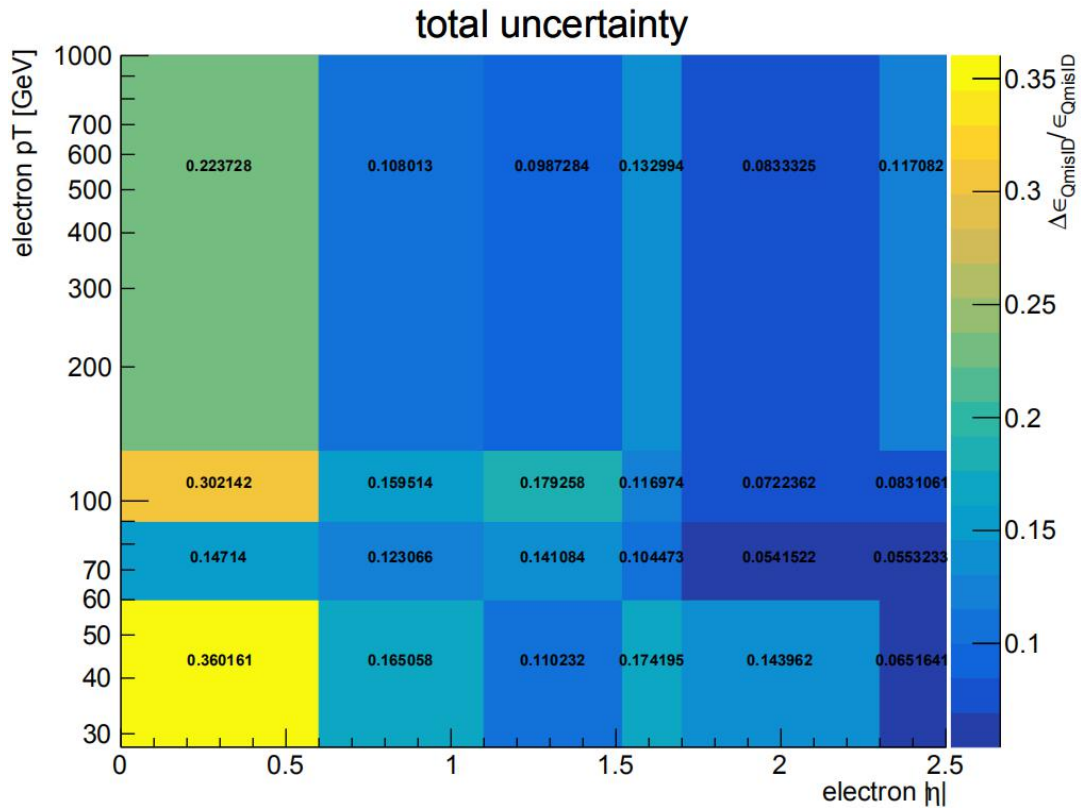


Figure A.1 Total systematic uncertainty of the electron charge mis-identification rates as a function of electron's p_T and $|\eta|$

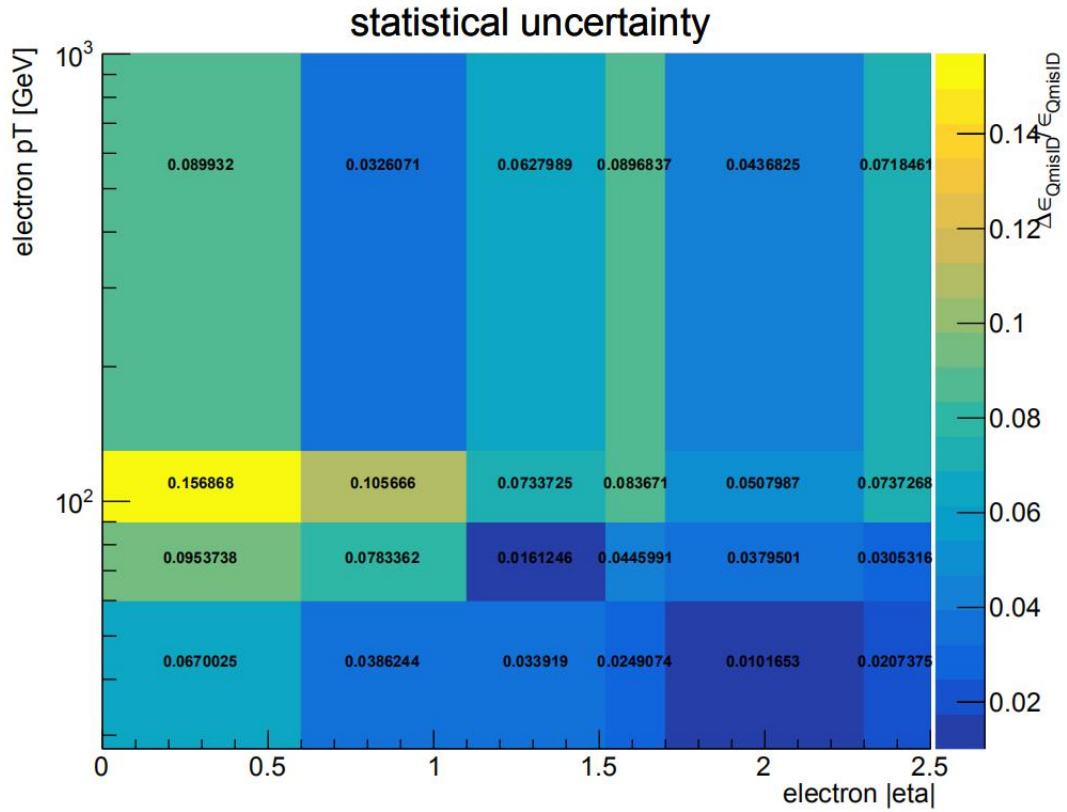


Figure A.2 Statistical uncertainty of the electron charge mis-identification rates as a function of electron's p_T and $|\eta|$

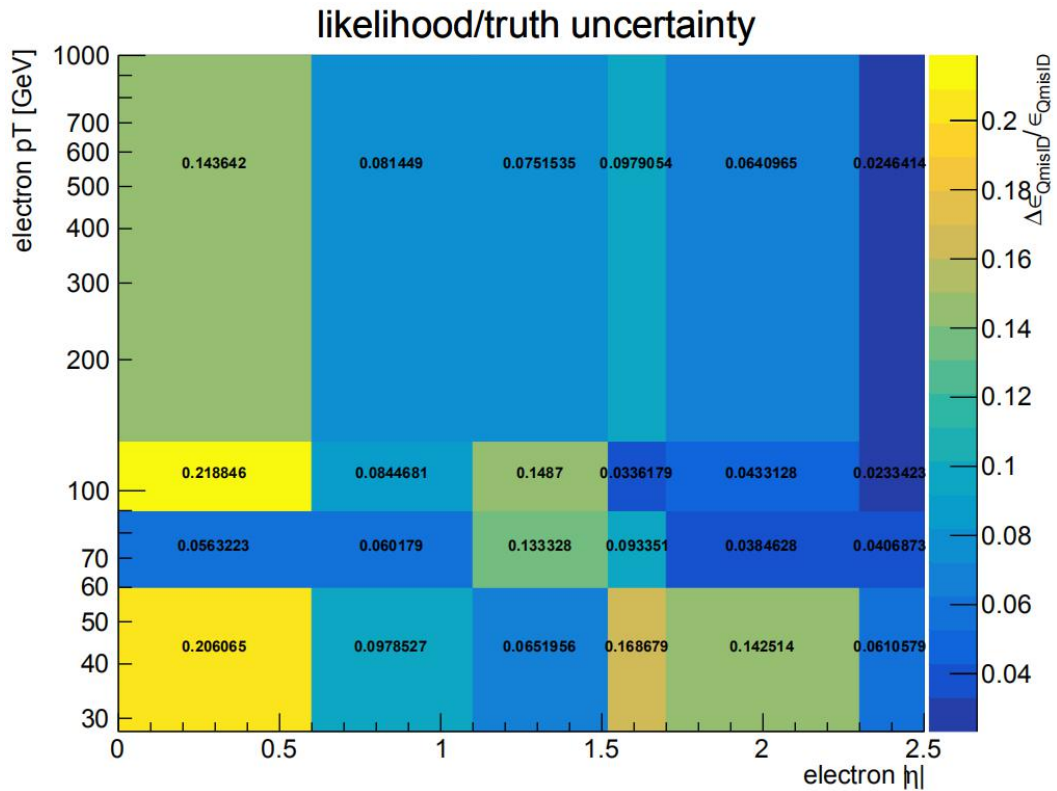


Figure A.3 Difference between the electron charge mis-identification rates from the likelihood fit method and the truth method as a function of electron's p_T and $|\eta|$

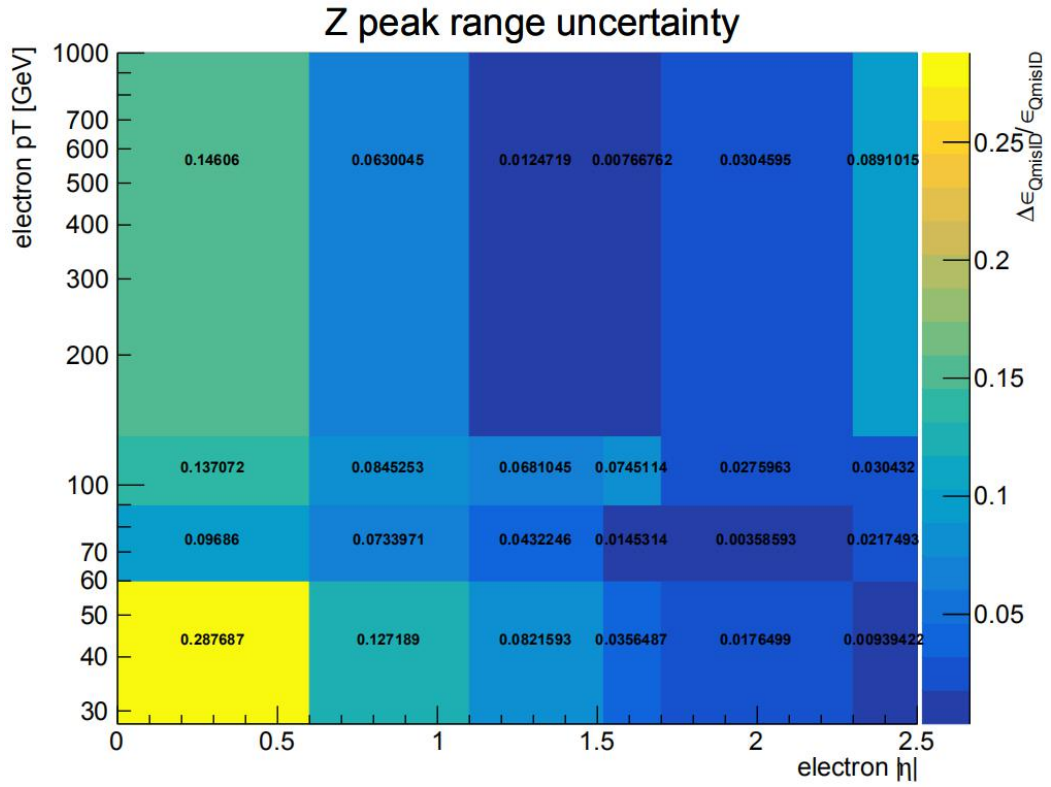


Figure A.4 Z peak range variation uncertainties of the electron charge mis-identification rates as a function of electron's p_T and $|\eta|$

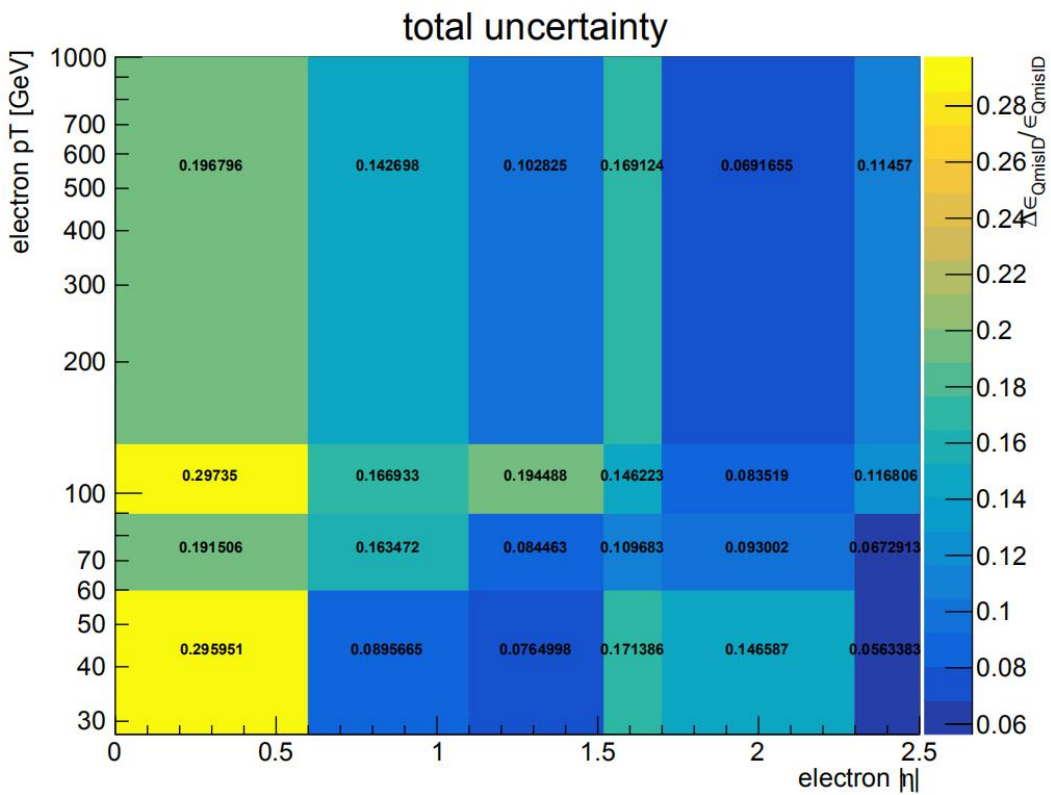


Figure A.5 Total systematic uncertainty of the electron charge mis-identification rates as a function of electron's p_T and $|\eta|$ in $t\bar{t}W$ control region

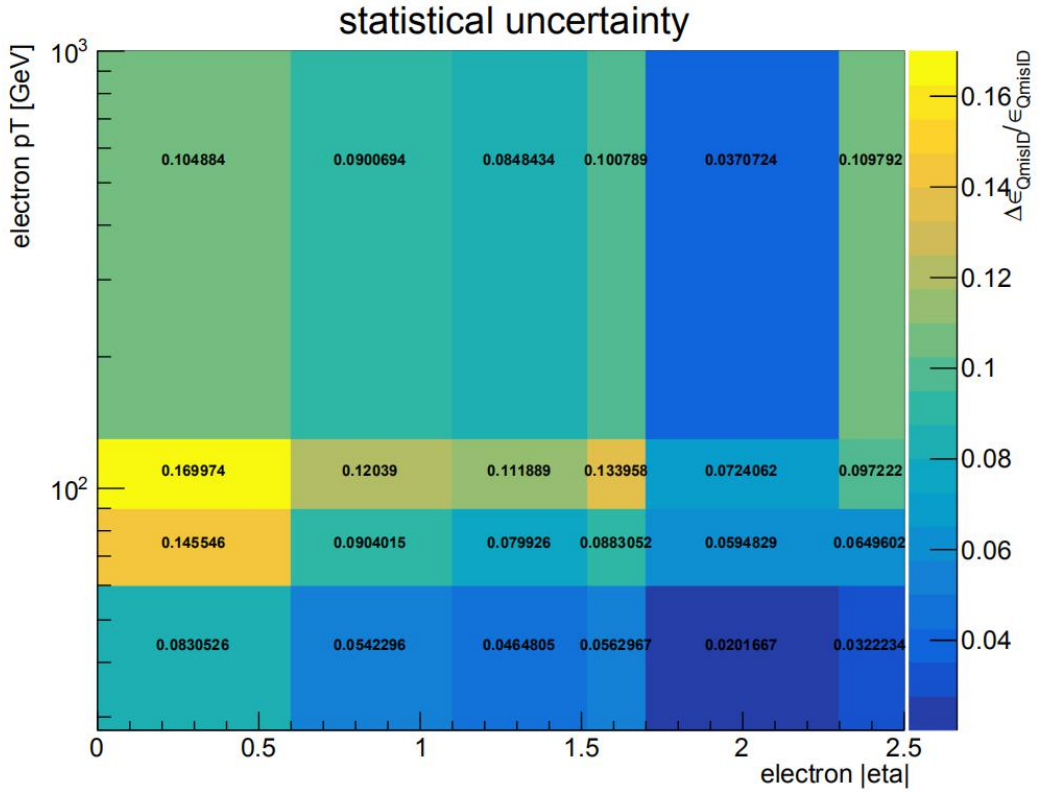


Figure A.6 Statistical uncertainty of the electron charge mis-identification rates as a function of electron's p_T and $|\eta|$ in $t\bar{t}W$ control region

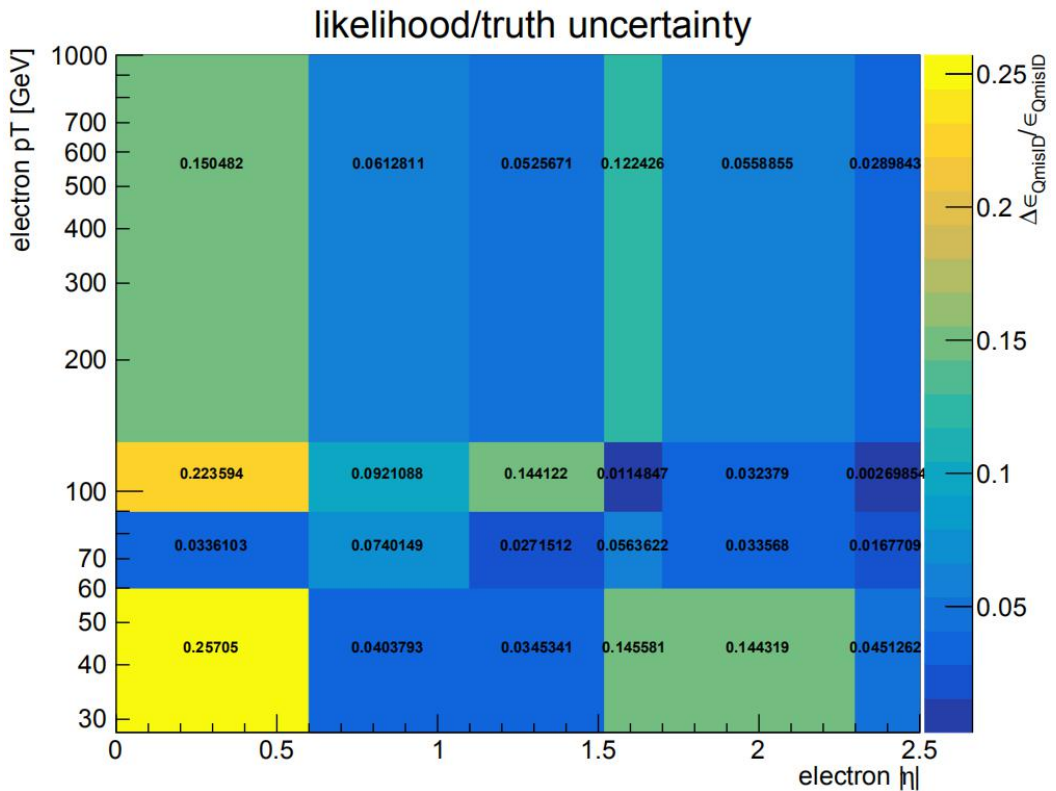


Figure A.7 Difference between the electron charge mis-identification rates from the likelihood fit method and the truth method as a function of electron's p_T and $|\eta|$ in $t\bar{t}W$ control region

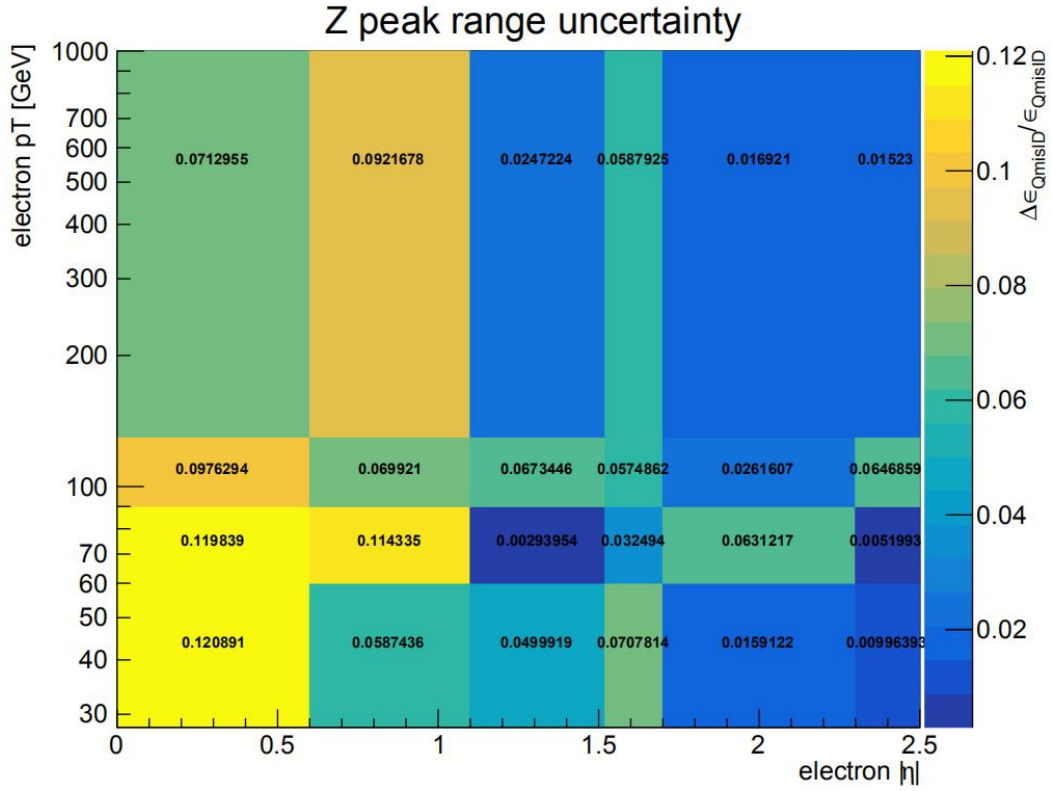


Figure A.8 Z peak range variation uncertainties of the electron charge mis-identification rates as a function of electron's p_T and $|\eta|$ in $t\bar{t}W$ control region

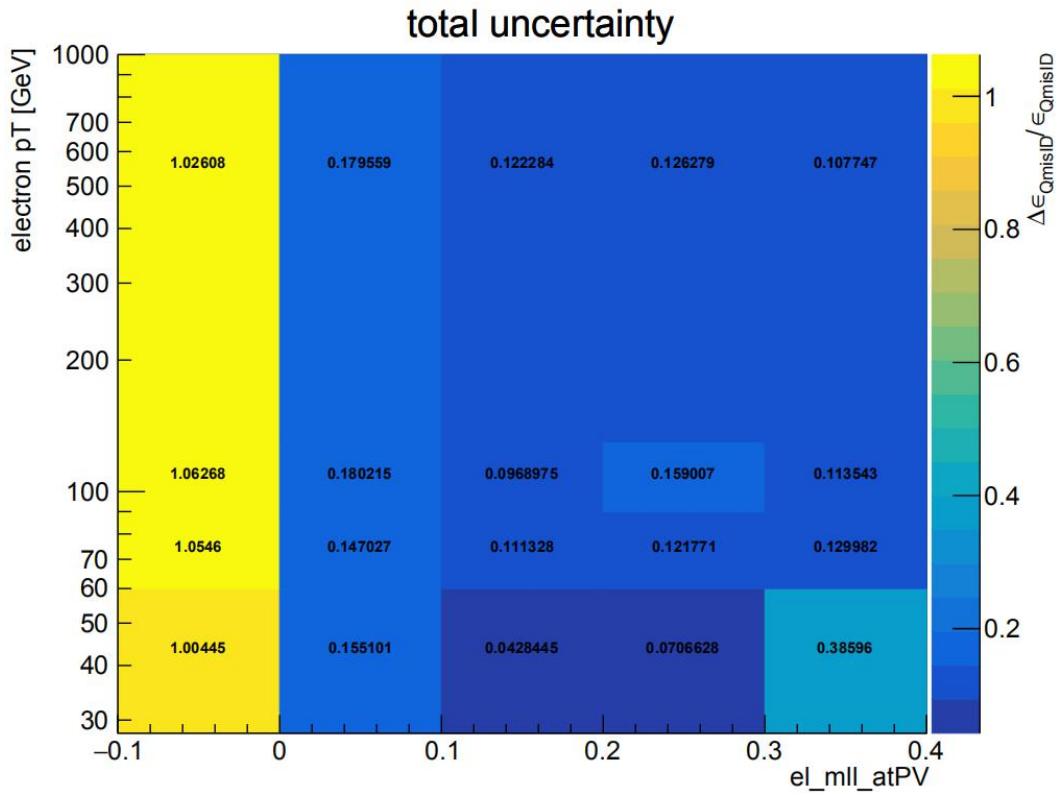


Figure A.9 Total systematic uncertainty of the electron charge mis-identification rates as a function of electron's p_T and $|\eta|$ in conversion control region

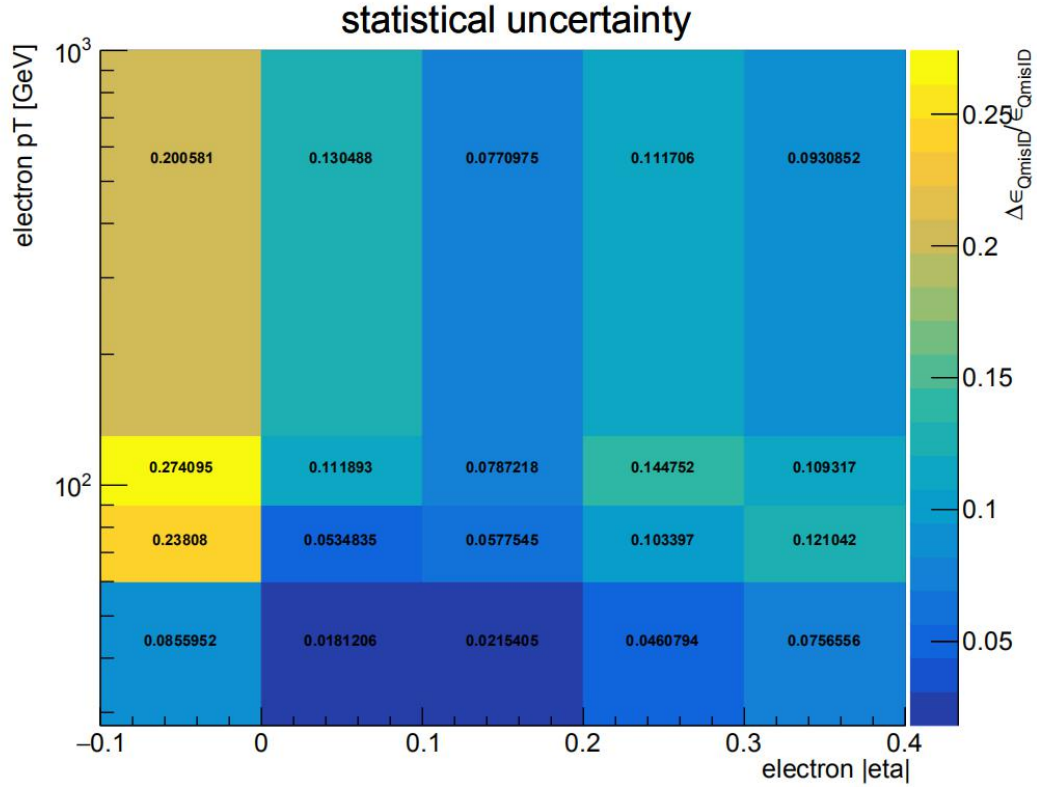


Figure A.10 Statistical uncertainty of the electron charge mis-identification rates as a function of electron's p_T and $|\eta|$ in conversion control region

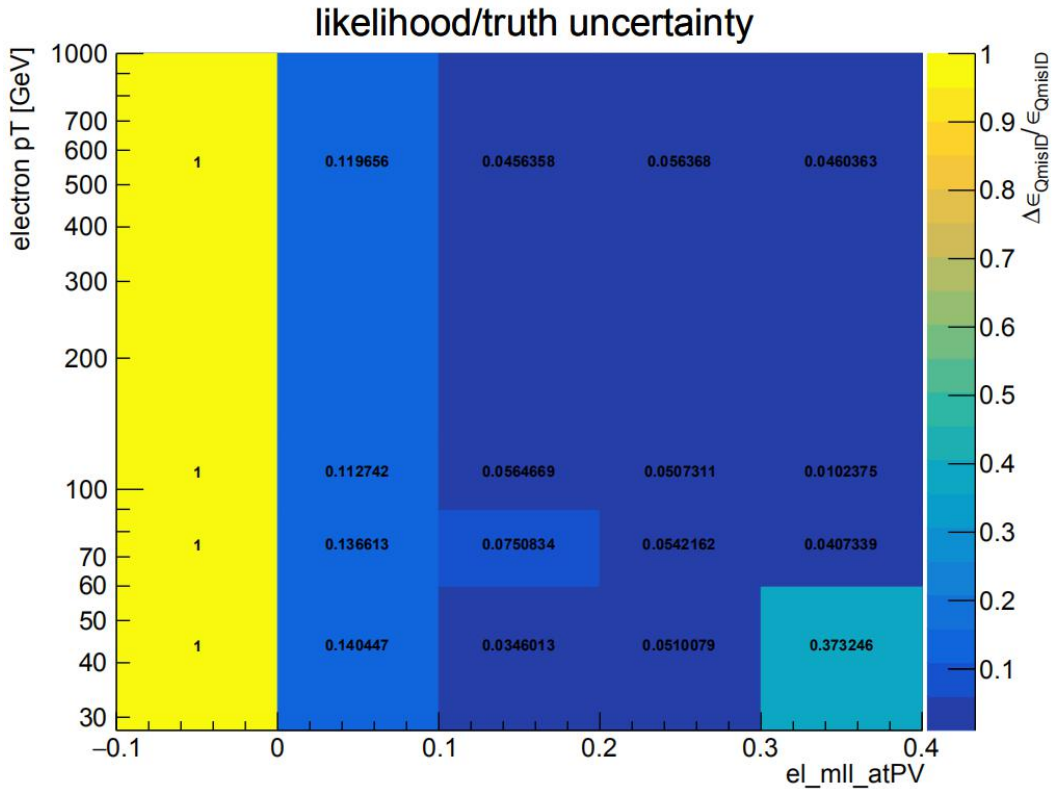


Figure A.11 Difference between the electron charge mis-identification rates from the likelihood fit method and the truth method as a function of electron's p_T and $|\eta|$ in conversion control region

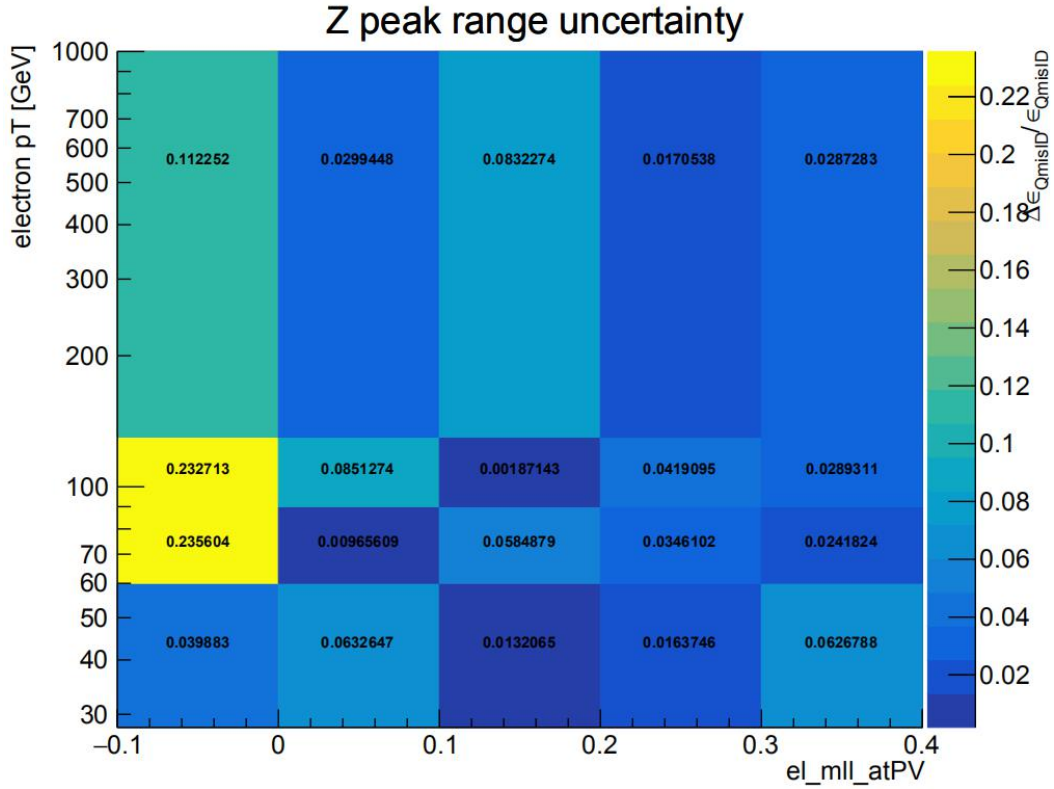


Figure A.12 Z peak range variation uncertainties of the electron charge mis-identification rates as a function of electron's p_T and $|\eta|$ in conversion control region

The charge mis-identification rates are set to be 0 in regions with negative $M_{ee@PV}$ values, since there is no truth-level electron information available. As seen in Figure A.11, the difference between the likelihood rates and the truth rates in the first $M_{ee@PV}$ bin is 100%.

Appendix B

Extended Abstract in French / Résumé en Français

Au cours des dernières années, la physique des particules a connu de grands développements aussi bien du point de vue théorique qu'expérimental. Le modèle standard (MS) est un modèle théorique à succès qui fournit une description unifiée des particules élémentaires et des interactions. Le grand collisionneur de hadrons (LHC) installé au CERN est le plus grand collisionneur du monde à la frontière en énergie. Le champ de Higgs, responsable de gérer une masse aux particules élémentaires, a été considéré comme la pièce manquante du MS pendant des décennies avant sa découverte. Après sa découverte en 2012 par les expériences ATLAS et CMS, le MS est finalement complet.

Malgré les succès du MS, certains processus rares, mais importants, n'ont pas encore été découverts. De plus plusieurs problèmes restent encore inexpliqués, comme le problème de hiérarchie, la masse des neutrinos ou l'origine de la matière noire. C'est pourquoi rechercher des scénarios de physique au-delà du MS (BSM) est important. Pour ces raisons, la production de 4 quarks top est particulièrement intéressant. Il s'agit d'un processus rare prédit par le MS mais non encore observé. Il est aussi sensible à de nombreux modèle BSM en raison de sa grande échelle d'énergie.

La production de quatre quarks top est prédit dans le MS pour avoir une section efficace extrêmement faible. La dernière prédiction du MS est : $\sigma_{t\bar{t}t\bar{t}} = 11.97^{+18\%}_{-21\%}$ fb pour $\sqrt{s} = 13$ TeV. Des analyses récentes ont publié une limite supérieure observée (attendue) sur la section efficace de 4 tops dans le MS de : 69 (29) fb. Un exemple de diagramme de Feynman de production de 4 tops est montré sur la figure B.1.

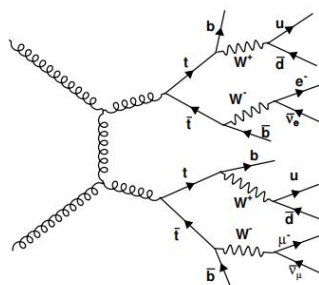


Figure B.1 Exemple de diagramme de Feynman pour la production de 4 tops dans le MS

Le LHC est le dernier étage du complexe d'accélérateurs du CERN. Il est installé 100 mètres sous terre dans un tunnel de 26.7 km de circonférence. Il est construit pour opérer à une énergie dans le centre de masse de 14 TeV, ce qui correspond à 7 TeV pour chaque faisceau de protons. ATLAS est l'un des détecteurs situés au point de collision entre ces faisceaux. C'est un détecteur multi-usage de 25 m de hauteur et de 44m de long pesant approximativement 7000 tonnes. Les sous-systèmes composant ATLAS sont : le détecteur interne (ID) comportant plusieurs systèmes de trajectographie, des calorimètres pour la mesure de l'énergie des particules et un spectromètre à

muons pour le détecteur des muons. Un système d'aimants est installé pour mesurer la courbure des particules et donc leur impulsion ainsi que pour l'identification de leur charge. Un système de déclenchement et d'acquisition de données est également présent afin de collecter les données du LHC avec une grande performance et un taux raisonnable.

Les différents types de particules laissent différentes signatures lorsqu'elles interagissent avec le détecteur. Les différents objets reconstruits sont : les vertex primaires et secondaires, les électrons, photons, muons, jets de hadrons et jets étiquetés provenant de quarks b (b-jets). Les particules portant une charge électrique laissent une trace dans le trajectographe. Les électrons et les photons déposent leur énergie dans le calorimètre électromagnétique, les jets hadroniques dans le calorimètre hadronique. Les muons peuvent atteindre le spectromètre à muons et y laisser une trace. Les neutrinos n'interagissent pas avec le matériel du détecteur et ainsi ne laisse pas de signature. Ils sont reconstruits en faisant un bilan d'énergie.

L'auteur de cette thèse a travaillé particulièrement sur l'isolation des muons. Les muons provenant de la désintégration de particules lourdes comme les bosons W, Z et de Higgs, sont souvent produits de façon isolés des autres particules. Contrairement aux muons provenant de désintégrations semi-leptoniques des hadrons b par exemple qui se retrouvent généralement à l'intérieur d'un jet, ces muons 'prompts' sont séparés des autres particules de l'événement. La mesure de l'activité autour du muon est appelée isolation et est un outil puissant de rejection du bruit de fond dans de nombreuses analyses.

La variable d'isolation basée sur les traces, $p_T^{\text{varcon}30}$, est définie comme la somme scalaire de l'impulsion transverse des traces de plus de $p_T > 1$ GeV dans un cône de taille : $\Delta R = \min(10\text{GeV}/p_T^\mu, 0.3)$ autour du muon d'impulsion transverse p_T^μ , en excluant la trace du muon. La taille de ce cône est choisie pour être indépendante de p_T pour améliorer les performances de l'isolation pour des muons provenant de désintégration de particules de haut p_T .

La variable d'isolation basée sur le calorimètre, $E_T^{\text{topocone}20}$, est définie comme la somme de l'énergie transverse des clusters topologiques dans un cône de taille $\Delta R = 0.2$ autour du muon, après soustraction de l'énergie déposée par le muon lui-même et après corrections des effets d'empilement. Les contributions d'empilements et d'événements sous-jacents sont estimées en utilisant une technique d'énergie-densité ambiante et sont reconstruites événement par événement. Les critères de sélection sur l'isolation sont déterminés en utilisant la valeur relative des variables d'isolation, définie par le rapport des variables ci-dessus divisées par l'impulsion transverse du muon. La distribution de ces variables relatives est montrée figure B.2 avec le rapport données sur simulation dans le bandeau inférieur.

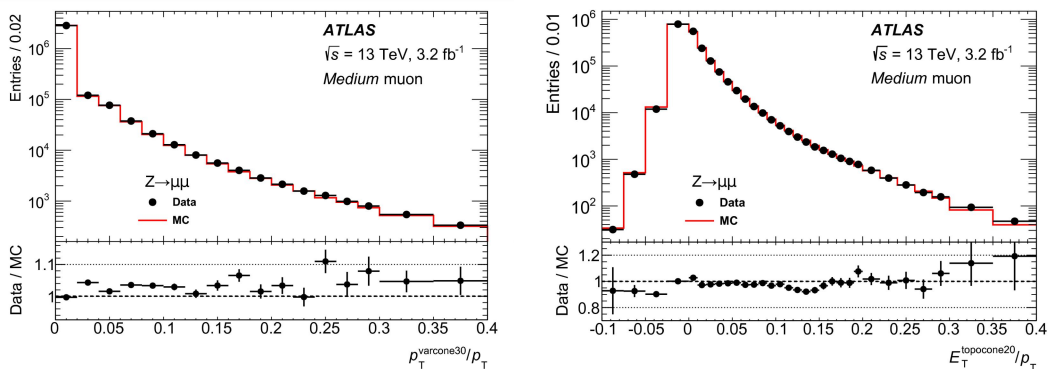


Figure B.2 Distribution de l'isolation relative basée sur les traces $p_T^{\text{varcon}30} / p_T$ (gauche) et sur le calorimètre $E_T^{\text{topocone}20} / p_T$ (droit)

Les données utilisées dans cette thèse correspondent à l'ensemble du Run 2 du LHC et ont été collectées entre 2015 et 2018 par le détecteur ATLAS à $\sqrt{s} = 13$ TeV. La luminosité intégrée correspondante est : $139.0 \pm 2.4 \text{ fb}^{-1}$. Cette thèse se focalise sur la recherche de la production $t\bar{t}t\bar{t}$ du MS dans le canal dilepton de même signe ou multilepton (SSML). Le rapport d'embranchement de ce canal est d'environ 12.5% ce qui est faible par rapport à d'autres canaux. Cependant ce canal bénéficie d'une plus faible contamination du bruit de fond. Les événements considérés dans cette analyse doivent satisfaire des critères liés au déclenchement ainsi que des critères cinématiques spécifiques.

L'estimation du bruit de fond est extrêmement importante dans la recherche de signaux rares comme $t\bar{t}t\bar{t}$. L'analyse a catégorisé les bruits de fonds en trois: les bruits de fond physique, estimés à partir du Monte Carlo, le bruit de fond provenant de charge mal identifiée et le bruit de fond avec de faux leptons ou des leptons non prompts. Ces deux derniers bruits de fond sont estimés directement dans les données. L'auteur de cette thèse a été en charge en particulier de l'estimation du bruit de fond provenant de charge mal identifiée. Cette estimation consiste d'abord à calculer le taux de mauvaise identification pour un électron, puis d'établir un poids correspondant à ce taux par événement et d'appliquer ce poids pour calculer le nombre d'événements de bruit de fond attendu. Ce travail inclue également l'évaluation des erreurs systématiques sur ces estimations et la validation de ces résultats.

Il y a deux manières pour que la charge d'un électron prompt soit mal identifiée. D'abord il peut s'agir d'un électron de très grande impulsion avec une trajectoire presque droite dans le trajectographe. Le deuxième cas provient de processus appelé trident, où l'électron initial radie un photon par bremsstrahlung puis le photon radié se convertit en une paire électron-positron. La mauvaise identification de la charge intervient alors si l'électron de conversion avec la mauvaise charge est reconstruit et identifié comme électron primaire. Cette mauvaise identification de la charge est négligeable pour les muons car la probabilité pour un muon de radier un photon par bremsstrahlung est beaucoup plus faible que pour un électron en raison de sa plus grande masse. De plus le plus grand bras de levier du spectromètre à muon permet de reconstruire la courbure des muons de façon plus précise.

Le bruit de fond provenant de charge mal identifiée est un bruit de fond important dans le canal dilepton de même signe. Les paires de leptons provenant des désintégrations de paires $t\bar{t}$ ou du boson Z sont à l'origine de signe opposé mais peuvent être prises pour du signal lorsque la charge de l'un des leptons est mal identifiée. La mesure de taux de mauvaise identification de la charge d'un électron est présentée sur la figure B.3 en fonction du p_T de l'électron et de sa pseudorapidité $|\eta|$ dans des événements Z+jets de données ou de simulation.

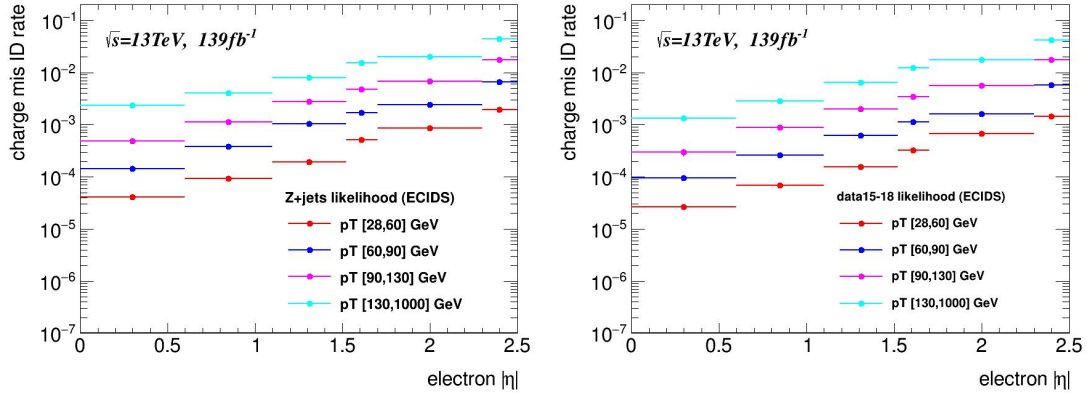


Figure B.3 Taux de mauvaise identification de la charge des électrons en utilisant une méthode de vraisemblance dans les données (gauche) et pour la simulation Z +jets (droite) en fonction du p_T et $|\eta|$ de l'électron

Le bruit de fond avec de faux leptons ou des leptons non prompts est estimé en utilisant une méthode d'ajustement de template. L'idée générale de cette méthode est de définir des gabarits (template) dans le Monte Carlo pour chaque composante de faux leptons afin de déterminer la forme des distributions cinématiques pour chaque composante. Puis plusieurs régions de contrôle dédiées sont définies afin d'extraire la normalisation des différentes composantes de faux leptons en ajustant les distributions Monte Carlo sur les données dans ces régions de contrôle. Un résumé des facteurs de normalisation obtenus pour les différentes composantes de faux leptons est présenté dans la table B1, ainsi que la normalisation obtenue pour le bruit de fond $t\bar{t}W$ qui s'est avéré mal simulé dans le Monte Carlo.

Parameter	NF $t\bar{t}W$	NF Mat. Conv.	NF Low mass γ^*	NF HF e	NF HF μ
Value	1.6 ± 0.3	1.6 ± 0.5	0.9 ± 0.4	0.8 ± 0.4	1.0 ± 0.4

Table B.1 Valeurs ajustées pour la normalisation des composantes de faux leptons et pour le bruit de fond $t\bar{t}W$

Afin d'améliorer la sensibilité de la recherche du signal $t\bar{t}t\bar{t}$, un discriminant multivarié est utilisé. La méthode choisie correspond à des arbres de décisions boostés (BDT). L'auteur de cette thèse a travaillé plus particulièrement sur l'optimisation des paramètres de ce BDT en utilisant la signification statistique du signal comme estimateur. Le BDT est construit pour discriminer le signal $t\bar{t}t\bar{t}$ de tous les bruits de fond dans la région définie comme étant la région du signal. Il est entraîné sur des échantillons Monte Carlo par une procédure entraînement-test-validation. La distribution pre-fit et post-fit de la sortie du BDT est présentée figure B.4.

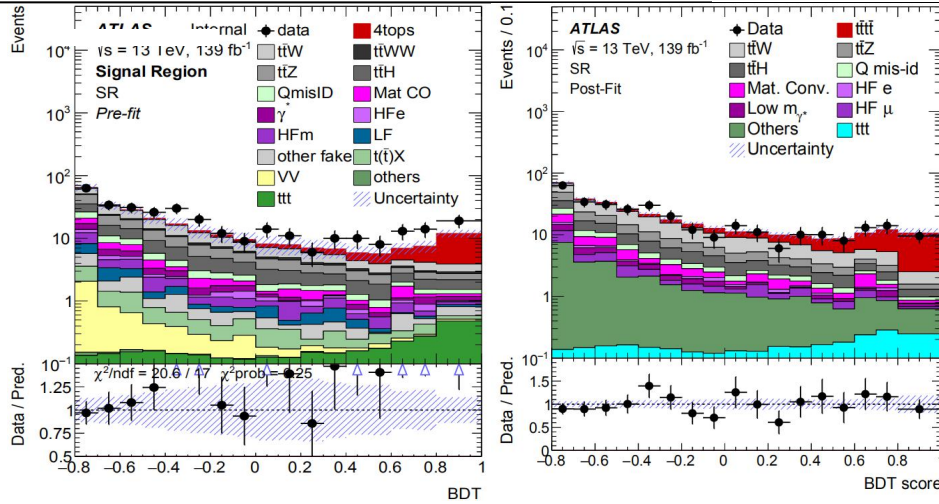


Figure B.4 Distribution pre-fit (gauche) et post-fit (droite) de la sortie du BDT dans la région de signal

L'accord entre données et Monte Carlo après l'ajustement est très bon. L'excès de signal observé par rapport au bruit de fond correspond à la cinématique attendue pour la production de 4 tops dans le MS.

Une analyse statistique est effectuée pour extraire le paramètre d'intérêt (POI). Dans cette analyse, le POI est la force du signal $t\bar{t}t\bar{t}$ notée μ , i.e. le rapport de la section efficace $t\bar{t}t\bar{t}$ mesurée sur la section efficace $t\bar{t}t\bar{t}$ attendue dans le MS. Un rapport de vraisemblance profilé est utilisé comme test statistique pour extraire la valeur de μ compte tenu du nombre d'événements observés dans les données et du nombre d'événements prédit. L'ajustement final est effectué simultanément sur la région de signal et sur les régions de contrôle. Quelques distributions post-fit pour la région $BDT > 0$ sont présentées sur la figure B.5.

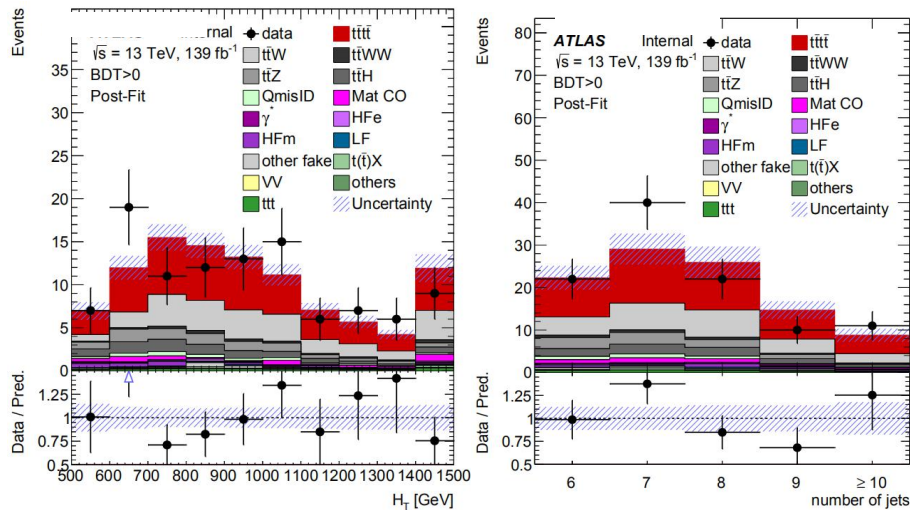


Figure B.5 Distributions post-fit pour la région $BDT > 0$

La force du signal extraite de l'ajustement est :

$$\mu = 2.0^{+0.4}_{-0.4} (stat)^{+0.7}_{-0.4} (syst) = 2.0^{+0.8}_{-0.6}$$

B.1

L'excès de signal sur le bruit de fond correspond à une signification statistique de 4.3 déviations standard pour une signification attendue de 2.4 déviation standard.

La modélisation du bruit de fond $t\bar{t}W + \text{jets}$ correspond à l'erreur systématique principale de l'analyse. La deuxième source la plus importante d'erreur systématique est la modélisation du signal puis les incertitudes systématiques sur la reconstruction des jets. L'erreur statistique est comparable au total des erreurs systématiques.

Après conversion de la force du signal μ en section efficace par multiplication de la section efficace $t\bar{t}t\bar{t}$ du MS, on trouve :

$$\sigma_{t\bar{t}} = 24_{-5}^{+5}(\text{stat})_{-4}^{+5}(\text{syst})fb = 24_{-6}^{+7}fb \quad \text{B.2}$$

Cette mesure de section efficace de production de $t\bar{t}t\bar{t}$ est compatible avec la prédiction du modèle standard au niveau de 1.7 déviation standard. Ce résultat constitue la première mise en évidence du processus de production de 4 quark tops.

Acknowledgement

Seven years has gone so fast. Wake me up when September ends.

I would like to start this part with two sentences from a famous English song *Wake Me Up When September Ends*.

The experience in the past seven years is quite unique. It is not smooth, but very impressive and precious. I won't be able to finish this thesis without the help of many people.

Firstly, I would like to say thanks to my supervisor Liang. He is a very knowledgeable and passionate guy who is always willing to help whenever I have trouble. I still remember his famous words, *whatever you do, try to be the best*. I will keep this in my mind for the rest of my life. Thanks to my co-supervisor Frederic. He is a very kind and warm-hearted person with great sense of responsibility. He helped me a lot during the period of my PHD, and especially during my stay in France. Thanks to Lang, who raised me up during my hardest time. Thanks to the SJTU group, for the precious memories in the past years.

Finally, I would like to say thanks to my family, and especially to my mom, for the selfless love and silent support behind my back. Without you, I won't be able to make this achievement.

The end of this thesis is the start of a new journey. Life is continuing and we have to keep moving on.

List of publication

1. Evidence for $tttt$ Standard Model Production in the Multilepton Final State in proton-proton Collisions with the ATLAS Detector, accepted by EPJC, arXiv: 2007.14858 [hep-ex].
2. Search for Higgs boson pair production in the $WWWW$ decay channel using ATLAS data recorded at $\sqrt{s} = 13$ TeV, JHEP 05 (2019) 124, arXiv: 1811.11028 [hep-ex].
3. Search for the Standard Model Higgs boson produced in association with top quarks and decaying into a bb pair in pp collisions at $\sqrt{s} = 13$ TeV with the ATLAS detector, Phys. Rev. D 97 (2018) 072016, arXiv: 1712.08895 [hep-ex].
4. Evidence for the associated production of the Higgs boson and a top quark pair with the ATLAS detector, Phys. Rev. D 97 (2018) 072003, arXiv: 1712.08891 [hep-ex].
5. Observation of Higgs boson production in association with a top quark pair at the LHC with the ATLAS detector, Phys. Lett. B 784 (2018) 173, arXiv: 1806.00425 [hep-ex].

Titre : Recherche de la production de 4 quark tops dans le modèle standard avec des états finaux de même signe di-lepton et multi-lepton à 13 TeV avec le détecteur ATLAS au LHC

Mots clés : quark top, modèle standard, processus rare, ATLAS

Résumé : Cette thèse présente les résultats sur la recherche de la production de quatre quarks top dans le canal deux leptons de même signe ou multilepton. L'analyse utilise l'ensemble des collisions proton-proton du Run 2 du LHC à $\sqrt{s}=13$ TeV collecté avec le détecteur ATLAS, ce qui correspond à une luminosité de 139 fb^{-1} . Les événements avec deux leptons de même signe ou au moins trois leptons avec de nombreux jets en particulier provenant de quarks b sont considérés. Les événements sont sélectionnés en région de signal et régions de contrôle avec une modélisation du bruit de fond appropriée. Un arbre de décision boosté (BDT), qui est une méthode multivariée, est alors utilisé pour augmenter la séparation entre le signal et le bruit de fond.

Enfin un ajustement par maximum de vraisemblance est effectué sur la sortie du BDT simultanément sur les régions de signal et de contrôle pour mesurer la section efficace de production de quatre quarks top et la force du signal (définie comme le rapport entre la section efficace mesurée et la prédiction du modèle standard). La section efficace mesurée est :

$\delta_{\text{tttt}}=24+5-5(\text{stat})+5-4(\text{syst})\text{fb}=24+7-6 \text{ fb}$, ce qui est compatible avec la prédiction du modèle standard à 1.7 déviations standard.

La force du signal correspondante est : $\mu=2.0+0.4-0.4(\text{stat})+0.7-0.4(\text{syst})=2.0+0.8-0.6$. La signification statistique observée (attendue) du signal quatre quarks top est 4.3 (2.4) σ , ce qui représente la première mise en évidence de ce processus.

Title : Search for standard model production of four top quarks with same-sign di-lepton and multi-lepton final states in proton-proton collisions at $\sqrt{s} = 13$ TeV recorded with the ATLAS detector

Keywords : quark top, modèle standard, processus rare, ATLAS

Abstract : This thesis presents the latest results of the Standard Model four-top-quark search in the same sign di-lepton and multi-lepton channel. The analysis uses the full Run2 proton-proton collision dataset at $\sqrt{s}=13$ TeV collected with the ATLAS detector, which corresponds to an integrated luminosity of 139 fb^{-1} . Events with two same sign leptons or three or more leptons, plus multiple jets and b-tagged jets in the final states are considered in the analysis. Further event and kinematic selections are performed in separate signal and background control regions with proper background modelling. Boosting Decision Tree (BDT) based Multi-Variate Analysis (MVA) method is then used to enhance signal and background separation.

Finally, a simultaneous likelihood fit is performed on the BDT discriminant across all the signal and background control regions to measure the four-top-quark production cross section and the signal strength (defined as the ratio of the measured cross section over the SM prediction). The measured four-top-quark production cross section is $\sigma_{\text{tttt}} = 24^{+5}_{-5}(\text{stat}) + 5^{+4}_{-4}(\text{syst}) \text{ fb} = 24^{+7}_{-6} \text{ fb}$, which is in consistent with the standard model prediction within 2 standard deviations. The corresponding signal strength is $\mu = 2.0^{+0.4}_{-0.4}(\text{stat}) + 0.7^{+0.4}_{-0.4}(\text{syst}) = 2.0^{+0.8}_{-0.6}$. The observed (expected) significance of the four-top-quark signal is 4.3 (2.4) σ , which provides the first evidence for the SM four-top-quark production.